České vysoké učení technické v Praze
Fakulta jaderná a fyzikálně inženýrská

**Katedra fyziky**
**Obor: Fyzika a technika termojaderné fúze**

# Studium okrajového plazmatu tokamaku COMPASS a jeho poloidálních variací

# Study of edge plasma of tokamak COMPASS and its poloidal variations

DIPLOMOVÁ PRÁCE

Vypracoval: Bc. Kateřina Jiráková
Vedoucí práce: Mgr. Jakub Seidl, Ph.D.
Rok: 2018

ČESKÉ VYSOKÉ UČENÍ TECHNICKÉ V PRAZE
**FAKULTA JADERNÁ A FYZIKÁLNĚ INŽENÝRSKÁ**
PRAHA 1 - STARÉ MĚSTO, BŘEHOVÁ 7 - PSČ 115 19

*Katedra:* fyziky *Akademický rok:* 2017/18

# ZADÁNÍ DIPLOMOVÉ PRÁCE

| | |
|---|---|
| *Student:* | Bc. Kateřina Jiráková |
| *Studijní program:* | Aplikace přírodních věd |
| *Obor:* | Fyzika a technika termojaderné fúze |
| *Název práce: (česky)* | Studium okrajového plazmatu tokamaku COMPASS a jeho poloidálních variací |
| *Název práce: (anglicky)* | Study of edge plasma of tokamak COMPASS and its poloidal variations |

*Pokyny pro vypracování:*

Charakterizujte parametry okrajového plazmatu tokamaku COMPASS a srovnejte a uveďte do souvislostí měření na různých poloidálních pozicích.

1. Porovnejte elektronovu teplotu měřenou na divertoru, reciprokými sondami a diagnostikou Thomsonova rozptylu a interpretujte výsledky pomocí analytického modelu paralelního transportu v SOL [1]. V případě dostupnosti vhodných simulací použijte i komplexnejší 1D či 2D numerické modely [2,3].

2. Měřením okrajové elektronové teploty určete na základě energetické rovnováhy [1] pozici separatrix a systematicky ji srovnejte s pozicí vrstvy střižných toků a výstupem magnetické rekonstrukce EFIT.

3. Charakterizujte a srovnejte radiální profily relevantních parametrů plazmatu, např. tlaku či tepelného toku, měřené polem divertorových sond a reciprokými sondami. Na jejich základě proveďte diskuzi charakteru transportu v okrajovém plazmatu.

*Doporučená literatura:*

[1] Stangeby, P. C.: The Plasma Boundary of Magnetic Fusion Devices, Taylor & Francis Group, 2000

[2] Havlíčková E., et al: Steady-state and time-dependent modelling of parallel transport in the scrape-off layer, Plasma Physics and Controlled Fusion 53(6), 2011

[3] Bufferand, H., et al: Near wall plasma simulation using penalization technique with the transport code SOLEDGE2D-EIRENE, Journal of Nuclear Materials 438, 2013

[4] Wesson, J.: Tokamaks, Oxford Press, 2011

*Jméno a pracoviště vedoucího diplomové práce:*

Mgr. Jakub Seidl, Ph.D., Ústav fyziky plazmatu AV ČR

*Datum zadání diplomové práce:* 20.10.2017

*Termín odevzdání diplomové práce:* 07.05.2018

*Doba platnosti zadání je dva roky od data zadání.*

*vedoucí katedry* ..... *děkan*

ČESKÉ VYSOKÉ UČENÍ TECHNICKÉ V PRAZE Fakulta jaderná a fyzikálně inženýrská -1-

*V Praze dne* 20.10.2017

**Prohlášení**

Prohlašuji, že jsem svou diplomovou práci vypracovala samostatně a použila jsem pouze podklady (literaturu, projekty, SW atd.) uvedené v přiloženém seznamu.

Nemám závažný důvod proti použití tohoto školního díla ve smyslu § 60 Zákona č. 121/2000 Sb., o právu autorském, o právech souvisejících s právem autorským a o změně některých zákonů (autorský zákon).

V Praze dne .....  .....

Bc. Kateřina Jiráková

**Poděkování**

Děkuji svému školitelovi Jakubovi Seidlovi za trpělivost a vysoké nasazení při vedení této práce. Mé poděkování patří také Jiřímu Adámkovi za konzultace ohledně sondových měření a Migleně Dimitrové za poskytnutí dat ze starého divertorového pole.

Bc. Kateřina Jiráková

*Název práce:*

**Studium okrajového plazmatu tokamaku COMPASS a jeho poloidálních variací**

*Autor:* Bc. Kateřina Jiráková

*Studijní program:* Aplikace přírodních věd
*Obor:* Fyzika a technika termojaderné fúze
*Druh práce:* Diplomová práce

*Vedoucí práce:* Mgr. Jakub Seidl, Ph.D.
Katedra fyziky, Fakulta jaderná a fyzikálně inženýrská, České vysoké učení technické v Praze
*Konzultant:* –

*Abstrakt:* V budoucích fúzních reaktorech bude nezbytně nutné udržovat velký teplotní spád mezi okrajem udrženého plazmatu a první stěnou včetně divertoru. Tato práce zkoumá, jestli v podobném režimu (anglicky zvaném conduction-limited regime) může pracovat i Scrape-Off Layer (SOL) tokamaku COMPASS v Praze. Diskuze je založena na vzájemném srovnání pěti diagnostik elektronové teploty: horizontální a vertikální reciproké sondy, starého a nového divertorového pole a Thomsonova rozptylu. Jejich profily jsou srovnány za pomoci korekce pozice separatrix a je dosaženo závěru, že pro SOL tokamaku COMPASS je typický jen velmi malý spád teploty i pro parametry, kdy by již měl nastat režim s velkými teplotními gradienty. Jako vysvětlení je zde navrženo, že paralelní profil teploty by mohlo zplošťovat proudění tepla.

*Klíčová slova:* Tokamak, transportní režim, Scrape-Off Layer, elektronová teplota, dvoubodový model

*Title:*

**Study of edge plasma of tokamak COMPASS and its poloidal variations**

*Author:* Bc. Kateřina Jiráková

*Abstract:* In future fusion reactors, maintaining a large temperature drop between the confined plasma and the first wall including the divertor will be vitally necessary. This thesis addresses the question whether the Scrape-Off Layer (SOL) of tokamak COMPASS in Prague can also operate in this conduction-limited regime. The discussion is based on comparing the electron temperature profiles measured by five diagnostics: the horizontal and vertical reciprocating probes, the old and new divertor array, and the Thomson scattering. Only small parallel temperature gradients are found even in those discharges with collisionality sufficiently high to induce the conduction-limited regime. The possibility of quite strong parallel heat convection is suggested as an explanation of the temperature profile flattening.

*Key words:* Tokamak, transport regime, Scrape-Off Layer, electron temperature, two-point model

# Contents

# Introduction

With the worldwide energy consumption rising exponentially, it is paramount for mankind to find new energy sources which are both scalable and sustainable. Nuclear fusion offers such an energy source, as it produces little to no radioactive waste, utilises the abundant sea water and lithium ores as fuel sources, and entails no risk of an uncontrollable chain reaction [1]. However, the great disadvantage of nuclear fusion are its high technological demands. Consider that in the fifties it was thought that fusion would become a reliable power source within twenty years [2]. Since then, the history of fusion has comprised of overcoming one obstacle (such as collective plasma instabilities, which were suppressed in the magnetic well configuration of Ioffe's bars) only to discover a new obstacle (loss cone micro-instabilities which rendered Ioffe's bars infeasible as a fusion reactor design).

One of the greatest challenges facing the operation of a fusion power plant is the issue of power exhaust. The fusion reaction intended for the current version of the demonstration power plant DEMO is D-T fusion,

$$^{2}\mathrm{D} +^{3}\mathrm{T} \rightarrow {}^{4}\mathrm{He} + \mathrm{n}^{0} + 17.6\ \mathrm{MeV}.$$

The energy output of this reaction is split unevenly between the helium nucleus (3.5 MeV) and the neutron (14.1 MeV). Neutrons, unaffected by the confining magnetic fields, fly out of the plasma vessel and are slowed down and absorbed in the cooling blanket. In contrast, the alpha particle deposits its energy in the surrounding plasma, heating it so that the fusion reaction continues. Thus the issue of power exhaust consists of two parts: designing and operating the cooling blanket, and exhausting power from the plasma itself. In this thesis, I will be interested in the latter.

There are two main channels which cool the plasma: radiation, and heat flow to plasma-wetted surfaces. While radiation is, like neutrons, absorbed volumetrically in the first wall and the cooling blanket, high energy plasma particles impinging on solid surfaces deposit their power locally. Thus, plasma facing components (PFCs) are at risk of structural changes and melting due to the strong concentration of heating power. In recent experiments, tungsten monoblock PFCs have been exposed to heat fluxes of the magnitude expected in DEMO, 20 $\mathrm{MW.m^{-2}}$, with the resulting effects including local melting, roughening, and formation of cracks that spanned the entire monoblock surface [3].

Managing power loads onto the PFCs breaks down further into several issues, including PFCs shaping to optimise power load spatial distribution, developing tungsten

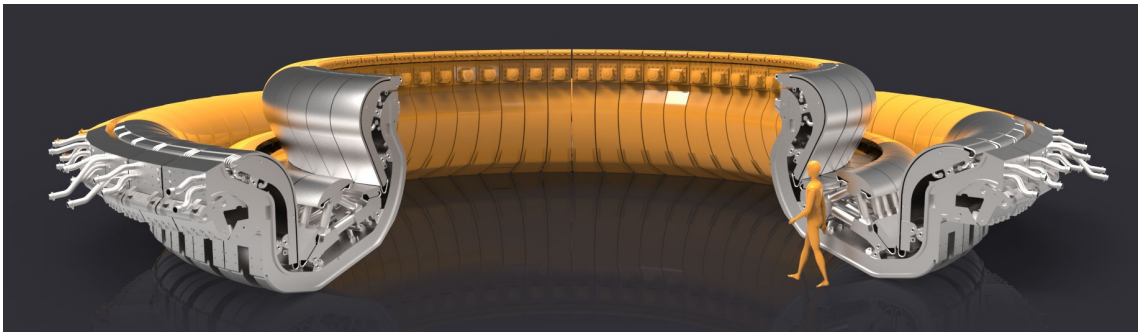

Figure 1: Model of the divertor for the ITER tokamak, which is currently under construction in France. [4]

composites for increased durability and resistance to sputtering, and others. In this thesis, the optimisation and control of plasma conditions at the plasma-surface contact location is investigated. In general, it is desirable to shroud the solid surfaces by plasma cool enough to feature a greatly increased neutral particle density (temperature in the order of a few eV). Within this "neutral cushion", high energy particles arriving from the confined plasma are slowed and cooled, depositing and radiating their energy in its volume rather than at the solid surface. Such a cushion can be created by controlling the heat and particle transport from the confined plasma to the wall. In particular, increasing the density and/or prolonging the distance between the hot plasma and the wall leads to the necessary cooling of wall plasma. In order to achieve both of these goals, it is advantageous to operate a tokamak in the divertor configuration.

The divertor, Fig. 1, is a PFC designed to withstand large heat fluxes on a long-term scale (on DEMO, up to hours [5]). Employing a divertor in a tokamak has numerous advantages. The parallel distance (i.e. distance along magnetic field line) of the divertor from the main plasma means that divertor plasma can be much cooler, protecting the plasma-wetted surfaces. Low temperature, in turn, implies higher density, and so the divertor volume is quite efficient at particle removal via pumping. Finally, operating in the divertor configuration offers an indisputable advantage over any other plasma equilibrium design. The high-confinement mode, imperative for self-sustained fusion reaction, has only been achieved in the divertor configuration.

The main goal of this thesis is to compare the conditions “upstream” (at the edge of the confined plasma) and “downstream” (at the divertor plates), using the experimental measurements carried out at tokamak COMPASS in Prague [6]. From this comparison, conclusions are drawn about the heat and particle transport regime between the two locations. Since COMPASS is a small tokamak ($R_0 = 0.56$ m, $I_p \leq 400$ kA, $B_T = 0.9$-$2.1$ T), its distance between upstream and downstream is relatively short. This implies that the heat from upstream reaches the target quite easily, resulting in only a small temperature drop and high target temperatures. Thus tokamak COMPASS can be expected to have difficulties entering the regime desirable for a fusion power plant, where the target temperature needs to be low while the upstream temperature remains high.

In Chapter 1 of this thesis, the theory of the two-point model (2PM) is presented. The 2PM is a very simple model of the divertor Scrape-Off Layer (SOL) which can be used to predict downstream conditions from control variables of tokamak operation. In this chapter it is derived from basic principles, with close attention paid to the mutual interconnection of its assumptions. It is shown how, using the 2PM, downstream conditions may be calculated from the control variables: the upstream density, the heat flux carried from upstream to target, and the distance between these two locations. By limiting the downstream temperatures to small values in the model, the limit of the conduction-limited regime is obtained. Its counterpart, whose defining feature is the lack of a temperature drop between upstream to downstream, is called the sheath-limited regime. The two regimes are defined quantitatively in this chapter using the collisionality parameter, and the collisionality of tokamak COMPASS is predicted based on its operational space. The result of this prediction is that the tokamak COMPASS mostly operates in the sheath-limited regime, with a possibility of the conduction-limited regime at the inner divertor target for high densities, $n_u > 1 \times 10^{19}$ m$^{-3}$, and low parallel heat fluxes, $q_\parallel < 15$ MW.m$^{-2}$. For the outer target the criteria for a high temperature drop are more constricting: $n_u > 2 \times 10^{19}$ m$^{-3}$ and $q_\parallel < 10$ MW.m$^{-2}$.

In Chapter 2, the diagnostics of tokamak COMPASS are introduced. The core of this thesis is the comparison of electron temperature profiles, and to that end five different diagnostics are employed: two reciprocating probes, two divertor probe arrays, and the Thomson scattering diagnostic. The probe measurements are further discussed in this chapter, providing details on the design and properties of ball-pen probes and Langmuir probes. The two divertor probe arrays are addressed in particular. It has been known that their measurements are at odds with each other, with the new divertor array measuring temperatures systematically higher than the old one and its profile being distorted by "teeth", for lack of a better word. Non-ambipolar, toroidally asymmetric currents are suggested as a possible explanation. The diagnostics chapter is concluded by listing the quantities inferred from the probe measurements and giving their formulas, as well as possible sources of uncertainties.

Chapter 3 contains the heart of this thesis: the experimental results, their interpretation, and discussion. It is divided into two sections, the first a necessary condition before proceeding on to the latter.

In the first half of Chapter 3, systematic errors in mapping performed by the magnetic equilibrium reconstruction programme EFIT++ are investigated and their correction is sought. Due to the large gradients in the vicinity of the separatrix, any displacement of this magnetic surface can lead to faulty conclusions about the likeness or difference of profiles measured at different places in the tokamak. Since the experimental part of this thesis stands on the comparison of $T_e$ profiles measured by five different diagnostics, proper mapping is the key to this analysis.

In the second half of Chapter 3, electron temperature profiles measured at upstream and downstream are compared within the frame of the 2PM. A very good agreement is found between the data and the model prediction, especially for the sheath-limited regime, as the 2PM is able to perfectly reproduce the measured upstream and target temperature profiles. However, in discharges where the model predicts significant

temperature drops, the COMPASS SOL is still isothermal, with the entire SOL temperature falling instead of supporting a temperature gradient. Since pressure and power are found to be preserved between the upstream and target, it is possible that the discrepancy is caused by parallel convective transport in the COMPASS SOL, which is not included in the 2PM. It is further shown that the outcomes of this analysis are strongly dependent on variables which are quite uncertain, such as the probe collection area or the mapping correction precision.

Chapter 4 summarises the findings of this thesis and it provides suggestions for further study, aiming to achieve significant parallel temperature gradients in the SOL despite the short connection length. It is followed by the references and the appendix.

# Chapter 1

# The two-point model and its applications

High-temperature plasma physics is a field of supreme complexity. Individual electrons, ions of various species and degree of ionization, molecules, photons, and many more components make up a plasma by interacting with one another. The number of particles is large, the number of interactions is larger yet. As a result, it is impossible to describe plasma with complete accuracy within a reasonable time frame. To allow at least some physical insight into the problem of plasma physics, simplified models have been developed, each focusing on a particular aspect of plasma physics and neglecting others. For instance, in magnetohydrodynamic studies (MHD) plasma is treated as a fluid, which involves losing all information contained in the velocity distribution function of particles. Thanks to this simplification, MHD is able to predict macroscopic plasma instabilities with good accuracy but it fails to predict microinstabilities, which can arise from a particular shape of the velocity distribution function. Respective models may be combined to provide a sophisticated simulation of plasma behaviour, however, the computation time can often be daunting. Thus there have been efforts in the opposite direction: to develop analytic models that give quick results at the cost of complexity and accuracy. The pioneer of this effort for tokamak SOL (scrape-off layer) modelling is P. Stangeby's two-point model (2PM) [7].

"Quick, if not very accurate results" is a fitting characterisation for this model. Eight pages of this chapter are enough to derive the 2PM, several more to discuss it, but the accuracy of its predictions is a matter beyond the scope of this thesis. The assumptions of the 2PM are quite strict and not necessarily close to reality, and consequently its predictions deviate from actual tokamak data sometimes in unpredictable ways.

For all its flaws, however, the 2PM has major advantages which advocate its use today and in foreseeable future. In Stangeby's basic form, which I present here, the 2PM is able to define and roughly predict two transport regimes of the scrape-off layer (SOL): the sheath-limited regime, and the conduction-limited regime. It also succeeds in identifying the mean of transition between the two, plasma collisionality $\nu^*$. The disagreement of the model to experimental data is not a show-stopper either;

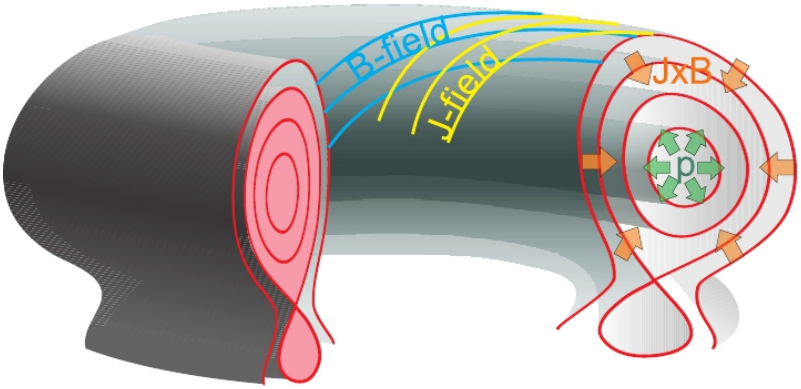


Figure 1.1: Schema of magnetic equilibrium of tokamak plasma in the divertor configuration. [10]

it is possible (and strongly advocated by Stangeby [8]) to incorporate correction factors into the model, which enable breaking the original strict assumptions but do not account for any actual physical processes leading to this deviation. The next step, taken for example by [9], broadens the meaning of "the two-point model" to "a two-point model" and proposes a model which relates the two points (upstream and downstream) using more complex equations. Such a model no longer yields analytic results like Stangeby's basic two-point model can, but on the other hand its predictions are in good accord with, in the cited article specifically, turbulent plasma simulation codes. From this point on, however, I will abandon such advanced models and I will focus solely on the basic two-point model developed by Stangeby.

In this chapter, the 2PM will be derived from basic physical assumptions. After a brief discussion of its three equations, the temperature drop from upstream to downstream will be quantified using the parameter $f_T = T_{upstream}/T_{downstream}$ and the formula for $f_T$ will be found from the 2PM. By taking two limits, one where $T_{upstream} \approx T_{downstream}$ and one where $T_{upstream} \gg T_{downstream}$, the sheath-limited and the conduction-limited regime will be defined, respectively. The operational space of tokamak COMPASS will be explored and the possibility of entering the conduction-limited regime, desirable for future fusion reactors due to its low target temperature, will be investigated. This will provide a frame for interpreting experimental data in chapter 4, Experimental results, where low collisionalities and low temperature drops will be found in accordance with the 2PM prediction.

## 1.1 Derivation of the two-point model

In this section, the 2PM will be derived from basic physical assumptions. The final form of the model will consist of three equations: the pressure balance equation, the heat conduction equation, and the power balance equation.

### 1.1.1 The two-point model geometry

To begin, it is necessary to define the geometry of the 2PM. This geometry is based on the magnetic equilibrium of a tokamak plasma in divertor configuration, figure 1.1, however, it is significantly simplified and reduced. A real tokamak plasma in equilibrium is a three-dimensional object, while the two-point model, as the name suggests, is only concerned with two points: upstream and downstream, or target.[1]

As to the actual position of upstream and target, there is a certain freedom left to the model user. The 2PM specifies that upstream and target are two locations directly connected via a magnetic field line, where upstream is the sole energy source and target the sole energy sink. Any pair of locations which fulfil this criterion are acceptable. But some choices are, naturally, more frequent than others.

The location of upstream is usually chosen at the outer midplane (OMP) or at the X-point, assuming toroidal symmetry to reduce the tokamak geometry to its poloidal cross-section cut. These two locations represent a compromise between the assumptions of the 2PM and the availability of probe measurements with sufficient spatial resolution. Speaking for the X-point is the fact that there are no significant energy sources along the magnetic field line leading from its vicinity to the divertor target. Speaking for the OMP, on the other hand, is the fact that many tokamaks feature a reciprocating probe installed at this location. Such a probe enables SOL parameters measurements with a good temporal and spatial resolution and thus provides precise input data into the 2PM. It is true that in this case, upstream is not a sole source of energy along the magnetic field line, as more power crosses the separatrix while the line is winding toward the X-point. However, it has been shown that radial transport in greatly enhanced in the 30° sector centred near the OMP, making this location the most prominent energy source along the flux tube [11]. And, after all, the 2PM can be adjusted slightly to account for power crossing the separatrix uniformly until the X-point. The only change this entails is modifying a factor 7/2 into 7/4 in the heat conduction equation of the 2PM, Eq. (1.1) [7]. Having considered all the previously listed factors, for this thesis the OMP was chosen as upstream, the main reason being the availability of the COMPASS tokamak database of OMP reciprocating probe measurements.

The location of target, or downstream, is quite straightforward in comparison to upstream. It is simply at the divertor target where the magnetic field line starting at upstream hits solid surface. Here three more issues need to be discussed.

Firstly, in experiment the toroidal locations of upstream and target measurements are given and can not be changed. In COMPASS, for example, the toroidal angle of the horizontal reciprocating probe (HRCP) is 202.5°, while the toroidal angle of the new divertor probe array is 100°. There is no a priori reason why a magnetic field line starting at the HRCP should end up directly atop the divertor array. It is much more likely that it will hit the divertor at some entirely other location, meaning that HRCP and the divertor probe array are not directly magnetically

[1] In the previous text the latter location was referred to as downstream for greater clarity. However, it is usual to use the subscripts "u" for upstream and "t" for target. Therefore, from this chapter on, the term "target" will be used instead of "downstream".

connected and therefore do not conform to the upstream-target geometry of the 2PM. The magnetic equilibrium of a tokamak experiment can be, to some level, adjusted. Unfortunately, the data from this thesis come solely from experiments done in the past, and there is no longer a way to influence the magnetic equilibrium. Thus, the argument of toroidal symmetry must be invoked, implying that the exact toroidal location of the measurements does not matter. As chapter 3, Experimental results, will show, toroidal symmetry of the divertor cannot be assumed lightly in the COMPASS tokamak. Measurements from the old and new divertor array, located 135° apart toroidally, show differences up to a factor of two in a quantity as basic as the Langmuir probe floating potential. The reason of this asymmetry is still being investigated, but it seems like toroidally asymmetric non-ambipolar currents to the divertor may be one of the factors. For the user of the 2PM, this means that he or she must consider carefully whether the experiment geometry and diagnostics quality allows to make the assumption of toroidal symmetry.

The second issue in the choice of upstream and target is that measuring the entire upstream and target profile gives us freedom to choose where in this profile upstream and target should be. Obviously, they must lie on the same magnetic surface, but should they lie in the near SOL, the far SOL, or some other specific location? The 2PM gives no directions here, other than what we already know: that energy should enter only at upstream, or uniformly until some point near the X-point, and it should not be lost until it reaches target. Since in experiment this condition is likely to be violated at any magnetic surface due to radial transport, radiation, charge exchange, and many other processes, the choice of the exact radial position does not matter very much. While Stangeby advocates that the ideal location for upstream is just outside the separatrix, it can be also argued that in high density regimes, power at the strike point has been observed to be largely dispersed and radiated before reaching the target [12]. This is due to the formation of the neutral cushion described in the introduction. This effect was, however, local to magnetic field lines ending near the strike point; further out in the SOL power losses were relatively much smaller due to smaller target density. It can thus be concluded that the choice of exact upstream/target location is mostly up to the user's discretion. In fact, the analysis can be carried out for each magnetic field line individually.

In this thesis, upstream was chosen to be just outside the separatrix, so target coincides with the strike point. There was one main reason for this decision. The magnetic equilibrium reconstruction code EFIT++ used on COMPASS shows a systematic error in the calculation of the OMP separatrix position. This grows to be a serious issue when, for instance, measuring plasma parameters at the separatrix. Due to strong gradients in the vicinity of the separatrix, an error in separatrix position of several centimetres can result in 50 % error in the magnitude of quantities measured at this location [13]. The issue of exact separatrix location at the OMP is not native only to tokamak COMPASS, but has been dealt with on other machines as well [14]. One of the ways to help solve this issue is to rely on the 2PM, as it allows its user to calculate the upstream temperature from the target temperature and several other quantities, such as power entering the SOL or the magnetic field line length. If a temperature profile measurement is available then, finding this upstream temperature on it yields the separatrix position. It follow from this that

carrying out the analysis in this thesis with upstream just outside the separatrix allows not only discussion of the SOL transport regime, but also an estimate of the separatrix position.

Finally, there is one more ambiguity regarding the location of target – the choice between the inner and the outer divertor target. In experiments conducted on other machines, both choices have been viable [14]. When choosing the OMP as upstream (which is the traditional decision when applying the 2PM), the inner target is magnetically more distant from upstream than the outer target. This implies a greater temperature drop toward the inner target and an earlier onset of the conduction-limited regime, where the magnetic field line length is sufficient to carry large temperature gradients and the target plasma is cold and dense. It has been, indeed, observed in experiment that the inner target can reach detachment (an extreme case of the conduction-limited regime where pressure and power losses near the target reduce the temperature to a few eVs) before the outer target. This provides an implicit validation of choosing the OMP as upstream and illustrates the possibility to analyse both the inner and the outer target using the 2PM. In the conditions of tokamak COMPASS, however, analysis of the inner target is not feasible. The reason is the inferior quality of temperature measurements in this part of the divertor, as the new divertor probe array routinely measures negative temperatures here. It is still under discussion whether this is an effect of magnetic shadowing due to tile misalignment or something else. The lack of a good explanation means that the inner divertor target is unusable for 2PM analysis. As a result, this thesis only uses one target location - the outer strike point.

This concludes the discussion concerning where upstream and target in the 2PM applied to COMPASS experimental data should be located. Upstream is at the outer midplane, just outside the separatrix, while target is at the outer strike point. The only issue left is to establish the 2PM geometry between these two points.

Upstream and target, lying on a single magnetic field line, are said to be connected via a flux tube. The actual perpendicular dimensions of this tube do not matter in the 2PM, but when applying the model to experimental data, they are estimated using the typical radial and poloidal spatial scales. These are the heat flux SOL width $\lambda_q$ and the quantity $4\pi R_{sep}\frac{B_{pol,sep,OMP}}{B_{total,sep,OMP}}$, respectively. For more details about these quantities, refer to section 3.1.4. While in experiment flux expansion causes the flux tube cross-section area to change along its parallel coordinate $s$, the 2PM neglects this variation and asserts the flux tube as having a constant, arbitrary cross-section area. This transformation is called straightening out the SOL and it is often used when modelling SOL transport [7].

The geometry of the 2PM is now set. The model space consists of two places, upstream and target, which are connected via a flux tube following a magnetic field line. Next, the principal assumption of the 2PM will be defined.

### 1.1.2 The principal assumption of the two-point model

Stangeby names pressure and power conservation as the two main assumptions of his 2PM [8], yet these can be further distilled to obtain the principal assumption of the 2PM: **The flux tube is a closed system in steady state, with power entering solely at upstream and leaving solely at target**. I will discuss this assumption in parts.

The term "closed system" is used in contrast to an isolated system (which does not exchange energy nor particles with its surroundings) and to an open system (which can exchange both), meaning that a closed system can exchange energy with its surroundings, but not particles. This lack of particle transport is not completely physically unreasonable – plasma at the upstream location can be in immediate pressure balance with the surrounding plasma. The lack of pressure gradients in all directions would then imply little to no particle transport. Meanwhile, plasma particles neutralised at the target may be assumed to be quickly released again and re-ionised at the same spot, keeping the sum of charged particles in the flux tube constant. Thus, particle balance in the entire flux tube can be achieved.

The assumption of steady state is self-explanatory, as the 2PM was developed to describe tokamak plasma equilibrium.

The last part of the principal assumption demands that no power is injected into the flux tube except at upstream and that the entirety of this power travels down the flux tube without any losses to be exhausted completely at target. The mean of upstream power injection is unspecified and arbitrary in the model, but target power exhaust is specified later in the derivation to be via the electric sheath, which forms around any solid conductor in contact with plasma [15]. The requirement of no power losses or gains, as well as no particle losses or gains along the flux tube translates into the lack of any perpendicular transport. This corresponds to ideal magnetic confinement, where drifts, turbulence, and particle collisions do not cause particles to leave their magnetic field line.

Next, the three main consequences of the principal 2PM assumption will be derived: pressure balance, conductive heat transport, and power balance.

### 1.1.3 Consequences of the principal assumption

To repeat, the flux tube is a closed system in steady state, where energy enters only at upstream and is exhausted only at target. This assumption can be unfolded again to obtain the core properties of the 2PM as listed by Stangeby: pressure balance and power balance. These relations together with conductive transport, which is a consequence of pressure balance, form a basis for the three equations of the 2PM.

To obtain pressure balance, consider the following. If the flux tube does not accept nor release particles, then all the particle motion must occur within it. However, as the connection between upstream and target cannot support circular flows, the flow of particles must be either one way or the other. If this were the case, however, and there existed a steady particle flow from one end to the other, then particles would

accumulate at the latter end, breaking the assumption of steady state. Therefore, there can exist no particle flow within the flux tube and the plasma must be stagnant. It follows that there can be no total pressure gradient along the flux tube, as this would inevitably act as a drive for particle flow. The magnetic component of hydrodynamic pressure force, $\mathbf{j} \times \mathbf{B}$, is zero as the flux tube copies a magnetic field line. Thus only plasma pressure $p$ remains (as the sum of the static and the dynamic part), and this is of the same value at upstream and at target.

$$p_u = p_t$$

Next, the necessity of conductive heat transport will be shown. Heat transport generally has two parts: convective, which is proportional to the plasma velocity, and conductive, which is proportional to the temperature gradient. The plasma velocity is zero as shown in the previous paragraph, and thus there can be no convective transport and the transport is purely conductive, obeying the law of diffusion,

$$q_\parallel = -k\nabla T,$$

where $q_\parallel$ is the parallel heat flux [$\mathrm{Wm}^{-2}$], $k$ is the thermal conductivity and $T$ is expressed in eV. Generally, both ions and electrons contribute to this heat flux, transporting heat according to their respective gradients and conductivities. However, as conductivity is inversely proportional to particle mass, electron conductivity is much higher than ion conductivity, and the ion contribution to the total heat flux may be neglected. Using Spitzer's formula for electron heat conductivity, $k = \kappa_{0e} T_e^{5/2}$ where $\kappa_{0e} = 2000$ for electrons ($\kappa_{0i} = 60$ for ions) [7], we obtain the heat conduction equation in its differential form,

$$q_\parallel = -\kappa_{0e} T_e^{5/2} \frac{\mathrm{d}T_e}{\mathrm{d}s}$$

where $s$ is the distance along the flux tube. Due to the assumption that no power leaves the flux tube and the flux tube cross-section area is constant along the flux tube, the heat flux $q_\parallel$ is also constant, allowing for integration from upstream ($s = 0$) to target ($s = L$). The symbol $L$ is then called the flux tube length or the connection length.

$$-\frac{q_\parallel}{\kappa_{0e}} \mathrm{d}s = T_e^{5/2} \mathrm{d}T_e$$

$$-\frac{q_\parallel L}{\kappa_{0e}} = \frac{2}{7} \left( T_{e,u}^{7/2} - T_{e,t}^{7/2} \right)$$

After rearranging the terms, the heat conduction equation in the integral form is obtained.

$$T_{e,u}^{7/2} = T_{e,t}^{7/2} + \frac{7}{2} \frac{q_\parallel L}{\kappa_{0e}} \tag{1.1}$$

The final consequence of the 2PM is power conservation – all power that enters at upstream leaves at target. Writing power as $P = q_\parallel A_\parallel$ where $A_\parallel$ is the cross-section area of the flux tube and recalling that this was defined to be constant in the geometry section, one can write:

$$q_{\parallel u} = q_{\parallel t}$$

### 1.1.4 The final form of the two-point model

The three current equations,

$$p_u = p_t$$
$$T_{e,u}^{7/2} = T_{e,t}^{7/2} + \frac{7}{2}\frac{q_\parallel L}{\kappa_{0e}}$$
$$q_{\parallel u} = q_{\parallel t}$$

are in the form most fitting to verify if the principal assumption of the 2PM is valid in experimental data. However, they are not suitable for making any predictions. In order to do this, the pressure $p$ and the heat flux $q_\parallel$ must first be written using plasma parameters such as density $n$, temperature $T$, and so on. With this goal in mind, several additional assumptions are made in the basic 2PM.

Firstly, impurity content is considered to be zero and the plasma is assumed to consist of pure deuterium. This means that ion mass is equal to the mass of a deuteron, given in the appendix A.

Secondly, Bohm criterion is assumed to hold. This criterion describes the plasma potential drop in front of an electrically floating conductor in contact with plasma, attributed to the absorption of the more mobile electrons. The resulting potential relative to the electric ground is called the floating potential $V_{fl}$, and it consists of a contribution from the plasma potential and from the electron temperature. This potential drop creates an electric field in a region called the sheath, where ions are accelerated toward the conductor and electrons are repelled. The resulting current is ambipolar, with an equal contribution from ions and electrons, making the net current zero.[2] A small portion of the electric field extends even beyond the sheath, whose characteristic length is the Debye length, into the so-called electric pre-sheath. This potential drop accelerates ions to the sound speed,

$$c_s = \sqrt{\frac{e(T_{i,t} + T_{e,t})}{m_i + m_e}},$$

at the sheath entrance (the temperature is, as everywhere in this thesis, given in eV). The sheath then exhausts power from the incident plasma at the rate

$$q_{\parallel t} = \sum_{\sigma \in [e,i]} \gamma_\sigma e n_{t,\sigma} T_{t,\sigma} c_{s,t}$$

where $\gamma_\sigma$ is the sheath heat transmission coefficient of species $\sigma$.

The third and final additional assumption of the 2PM is thermal equilibrium between ions and electrons, $T_e = T_i$.

Together these additional assumptions provide the relationships

$$n_e = n_i = n \tag{1.2}$$

[2]The actual divertor tiles of tokamak COMPASS are not floating, but grounded. It is possible that this affects the measurements of probes (which are, themselves, floating), by influencing the plasma potential near the divertor target and causing $\mathbf{E} \times \mathbf{B}$ drifts which distort probe measurements. More information is given in section 2.1.1.

$$T_e = T_i = T \tag{1.3}$$

$$m_i = m_d = 3.343 \times 10^{-27}\,\mathrm{kg} \tag{1.4}$$

$$v_{\parallel t} = c_{s,t} = \sqrt{\frac{2eT_t}{m_i}} \tag{1.5}$$

$$q_{\parallel t} = \gamma e n_t T_t c_{s,t} \tag{1.6}$$

where $\gamma = 7$ [7] is the total sheath heat transmission coefficient. Notice that the consequence of the Bohm criterion is that the target plasma velocity is non-zero. The sheath is considered to take up a negligible part of the flux tube length, so this does not influence the transport character further upstream. In fact, as shown by Stangeby [7], plasma velocity may be non-zero in a considerable part of the flux tube without affecting the 2PM significantly.

Using relations (1.2)-(1.6), the 2PM equations may be rewritten. Pressure, consisting of the static and the dynamic part for ions and electrons,

$$p = \sum_{\sigma\in[e,i]} \left(p_{stat,\sigma} + p_{dyn,\sigma}\right) = \sum_{\sigma\in[e,i]} \left(enT + m_\sigma n v_\parallel^2\right)$$

is purely static at upstream due to zero plasma velocity. Thermal equilibrium then causes the two terms in static pressure to add up,

$$p_u = 2en_uT_u.$$

The target pressure consists of both the static and the dynamic part. The electron dynamic part is small compared to the ion part because of the electron mass factor, and it may be neglected. Then, using $c_{s,t} = \sqrt{2eT_t/m_i}$,

$$p_t = \sum_{\sigma\in[e,i]} \left(en_tT_t\right) + m_i n_t c_{s,t}^2 = 4en_tT_t.$$

Since $q_{\parallel u} = q_{\parallel t}$ and the subscript does not matter, it is left out and the heat flux is denoted simply $q_\parallel$, giving

$$q_\parallel = \gamma e n_t T_t c_{s,t}$$

Collecting all three equations (and reducing the pressure equation of the factor $2e$), the basic 2PM is obtained:

$$\boxed{\begin{aligned} n_uT_u &= 2n_tT_t \\ T_u^{7/2} &= T_t^{7/2} + \frac{7}{2}\frac{q_\parallel L}{\kappa_{0e}} \\ q_\parallel &= \gamma e n_t T_t c_{s,t} \end{aligned}}$$

## 1.2 Application of the two-point model

In this section, the 2PM derived above will be discussed. In particular, I will be interested in its application to the COMPASS tokamak as a predictor of plasma parameters which are difficult to control in experiment.

The basic 2PM as framed above *relates* the upstream and target plasma parameters ($n_u$, $T_u$, $n_t$, $T_t$) using the parallel heat flux $q_\parallel$, the flux tube length $L$, and several constants. For predicting the parameter values, however, formulas for individual *dependent* variables as determined by *independent* variables is much more convenient. This is why the usual conception of the 2PM involves considering the upstream density $n_u$, the heat flux $q_\parallel$, and the flux tube length $L$ as control variables, while the other three ($n_t$, $T_t$, and $T_u$) are dependent. The reason for this particular choice is that $n_u$, $q_\parallel$, and $L$ may be (to some extent) controlled in a tokamak experiment. Upstream density $n_u$ is proportional to the line-averaged electron density $\overline{n}_e$, which is controlled by fuelling. The heat flux $q_\parallel = P_{SOL}/A_\parallel$ is proportional to the power crossing the separatrix, which in turn is determined by the total heating power. Finally, the flux tube length $L$ depends on the magnetic equilibrium geometry, which is controlled by the toroidal magnetic field $B_T$, the plasma current $I_p$, and the currents in the shaping coils. The control mechanisms are not linear and achieving different parameters usually demands an experienced tokamak operator, but controlling $n_u$, $q_\parallel$, and $L$ is still more straightforward than controlling, for instance, the target temperature.

To obtain formulas for the individual dependent variables, the quantities must first be extracted from the 2PM equations. This is a somewhat complicated task, as the heat conduction equation includes three non-linear terms. The step usually taken here is to assume a substantial temperature drop along the flux tube (the conduction-limited regime), implying $T_u^{7/2} \gg T_t^{7/2}$, and neglect the target temperature term. In many larger tokamaks this assumption is legitimate, since $T_t = T_u/2$ is sufficient to reduce $T_t^{7/2}$ to 9 % of $T_u^{7/2}$ thanks to the large exponent 7/2. In the conditions of tokamak COMPASS, however, temperature drops are usually much smaller than one half. In other words, when COMPASS values are used (section 3.2.2), the term $\frac{7}{2}\frac{q_\parallel L}{\kappa_{0e}}$ in the heat conduction equation is small compared to the other two. Since the formulas derived here ultimately serve to explore these very conditions, $T_u \approx T_t$ must be assumed and the common neglection of $T_t$ is impossible to carry out.

Let us now derive the exact solution of the 2PM for $T_t$, $n_t$, and $T_u$. The easiest variable to extract from the three 2PM equations is $T_t$. (For the complete derivation, refer to appendix B.) One may combine the equations to obtain a quasi-cubic equation of the form

$$x^3 + Bx - A = 0$$

where

$$A = \left( \frac{q_\parallel (2m_i)^{1/2}}{\gamma n_u e^{3/2}} \right)^{7/2},$$

$$B = \frac{7 q_\parallel L}{2\kappa_{0e}}, \text{ and}$$

$$x = T_t^{7/4}.$$

This equation has two complex roots and one real root, which can be calculated analytically. The resulting expression for $T_t$ is somewhat complicated when written down, (B.8), but its numerical calculation is straightforward. With $T_t$ known, the rest of the dependent variables are easy to work out. The upstream temperature $T_u$ follows directly from the heat conduction equation,

$$T_u = \left( T_t^{7/2} + \frac{7}{2} \frac{q_\parallel L}{\kappa_{0e}} \right)^{2/7}. \tag{1.7}$$

Notice the exponent $2/7$. This causes the upstream temperature to be remarkably insensitive to the control variables variation. Or at least - it is insensitive as long as the heat flux term is significant compared to $T_t^{7/2}$. The target temperature is, in contrast to the upstream one, quite sensitive to the control parameters [7], so if $T_u \approx T_t$, the upstream temperature varies just as quickly as $T_t$. Indeed, it is shown for tokamak COMPASS, where temperature differences between upstream to target are typically small, that for the outer strike point $T_u$ = 20-80 eV across the entire operational space (figure 1.2). Thus one has to be careful before applying the common practice [16] and assuming a static value of $T_u$ across all discharges in a small tokamak device such as COMPASS.

Knowing now the upstream and target temperatures, the target density $n_t$ follows from the pressure balance equation,

$$n_t = \frac{n_u T_u}{2T_t}.$$

Thus all three dependent quantities can be precisely computed from $n_u$, $q_\parallel$, and $L$ using the 2PM.

### 1.2.1 SOL transport regimes

For the operation of a fusion reactor, which requires very high temperatures in its core, it is desirable to induce a large temperature drop from upstream to target. A low target temperature reduces physical sputtering, which can otherwise erode the target material and contaminate the plasma with impurity atoms, it lowers the risk of melting and other phase changes, and prolongs the divertor lifetime. It is one of the great achievements of the 2PM that it can be used to predict this temperature drop from the values of $n_u$, $T_u$, and $L$. In this section, the process of deriving the key parameter of SOL transport, collisionality, will be shown and two SOL transport regimes will be defined: the sheath-limited regime and the conduction-limited regime.

To begin, we define the temperature gradient factor:

$$f_T \equiv \frac{T_u}{T_t}.$$

This factor serves simply to put the term "temperature drop" into numbers. In the classical derivation which I follow here, $f_T > 3$ and $f_T < 1.5$ are used as the criteria

for a high and low gradient, respectively [7]. This corresponds to $T_t^{7/2}$ being 2% (negligible) and 24 % of $T_u^{7/2}$ (not negligible), respectively. Stangeby then calculates the value of $f_T$ using the 2PM equations and arrives at the following expression:

$$\frac{n_u L}{T_u^2} = \frac{4\kappa_{0e}}{7\gamma e c_{s0}} f_T^{1/2} \left(1 - f_T^{-7/2}\right) \tag{1.8}$$

On the left-hand side (LHS) appear only upstream quantities and the flux tube length, while on the right-hand side (RHS) appear only constants and $f_T$ itself, with $c_{s0}$ denoting the sound speed for $T = 1$ eV. There are three reasons for employing $T_u$ here rather than the control variable $q_\parallel$. One is that, as stated previously, in devices with a large temperature gradient the value of $T_u$ is not very sensitive to any of the control variables. The second reason is that the expression $\frac{n_u L}{T_u^2}$ has an immediate physical meaning - it is the mean number of collisions that a particle undergoes along the way from upstream to target, times $10^{16}$. This follows from the fact that particle mean free path can be expressed as $\lambda = 10^{16} T_e^2/n$ [7]. Finally, a similarly defined collisionality is one of the dimensionless parameters which naturally emerges in the core plasma modelling [17]. This shows that collisionality is physically important for plasma physics as a whole. For these three reasons, it is convenient to leave $T_u$ in the expression rather than to substitute it with $q_\parallel$.

The LHS of equation (1.8) can now used as a basis for defining a more compact parameter corresponding to the temperature gradient size: the plasma collisionality

$$\nu^* \equiv 10^{-16} \frac{n_u L}{T_u^2}.$$

The factor $10^{-16}$ reduces the collisionality value to a sensible number: $f_T = 3$ corresponds to $\nu^* = 15$, $f_T = 1.5$ to $\nu^* = 10$. More importantly, thus defined collisionality is directly equal to the mean number of collisions between upstream and target,

$$\nu^* = \frac{L}{\lambda}.$$

The following table sums up the transformation from $f_T = T_u/T_t$ to the plasma collisionality.

| | | | |
|---|---|---|---|
| small gradient | $f_T < 1.5$ | $\frac{n_u L}{T_u^2} < 1 \times 10^{17}$ | $\nu^* < 10$ |
| significant gradient | $f_T > 3$ | $\frac{n_u L}{T_u^2} > 1.5 \times 10^{17}$ | $\nu^* > 15$ |

When temperature gradients are small and collisionality $\nu^* < 10$, we say that the SOL in *the sheath-limited regime*. Conversely, when great temperature drops arise and $\nu^* > 15$, we speak of *the conduction-limited regime*. The names of these two SOL transport regimes come from the dominant physical processes involved. For low collisionalities, particles do not collide many times before reaching the target, and so they are predominantly affected by the electric field of the pre-sheath and

the sheath, thus the sheath-limited regime. On the other hand, at high $\nu^*$ collisions affect the particles more than the electric field and the transport is dominated by heat conduction, thus the conduction-limited regime. It is good to remind here that the low target temperatures of the conduction-limited regime do not imply any momentum or power losses. The low $T_t$ is compensated for with high $n_t$ so that the total pressure remains constant. Naturally, in experiment sufficiently low $T_t$ will cause ion-neutral and other interactions to disperse plasma energy and momentum, however, the original definition of the conduction-limited regime entails no losses in accord to the original 2PM assumptions.

In reactor conditions the target temperature should be as low as possible, which is why there have been efforts to control the value of SOL plasma collisionality. From its definition one sees three ways to increase $\nu^*$: increasing the upstream density $n_u$ (for example by increased fuelling), increasing the flux tube length $L$ (for example by moving the X-point further from the divertor), and decreasing the upstream temperature $T_u$ (for example by reducing the heating power). Each of the parameters has a certain range in a tokamak device, depending on its operational space. For instance, the density is limited by the Greenwald density limit; if overstepped the plasma becomes unstable and prone to disruptions. The COMPASS tokamak, with $R = 0.56$ m and $L \approx 10$ m, is a relatively small-sized machine. The question of this thesis is if it can achieve sufficient collisionalities to enter the steady-state conduction-limited regime despite its size.

### 1.2.2 Two-point model predictions for tokamak COMPASS

In this section, values of plasma collisionality will be predicted for COMPASS using the 2PM. It is, however, important to keep in mind that these predictions are based on assumptions that may not hold in an actual tokamak, such as the lack of radial transport and convective parallel transport in the SOL. Therefore, they must be taken with a grain of salt.

Figure 1.2 shows the 2PM predictions for $f_T$, $T_u$, $T_t$, and $\nu^*$ within the COMPASS operational space. (To see the actual operational space, refer to section 3.2.1.) $L = 5.3$ m was used as the flux tube length, the value obtained by magnetic field line tracing from the outer midplane to the outer strike point. The figure shows that in a large part of the parameter space, the outer target collisionality does not exceed 15. There is, however, a window at high densities $n_u > 2 \times 10^{19}$ m$^{-3}$ and low heat fluxes $q_\parallel < 10$ MW.m$^{-2}$ where the outer target is predicted to enter the conduction-limited regime. The characteristic temperature drops will be sought in the experimental part of this thesis using the electron temperature measurements of several diagnostics.

Figure 1.3 shows the same situation for the inner strike point, where $L = 14.6$ m. Thanks to the larger connection length the conduction-limited conditions encompass a broader range of parameters, $n_u > 1 \times 10^{19}$ m$^{-3}$ and $q_\parallel < 15$ MW.m$^{-2}$. In the $T_u$ plot, the characteristic 2/7 insensitivity can be seen - from a certain density on, $n_u$ has little effect on $T_u$ while the $q_\parallel$ dependency grows weaker and weaker. It

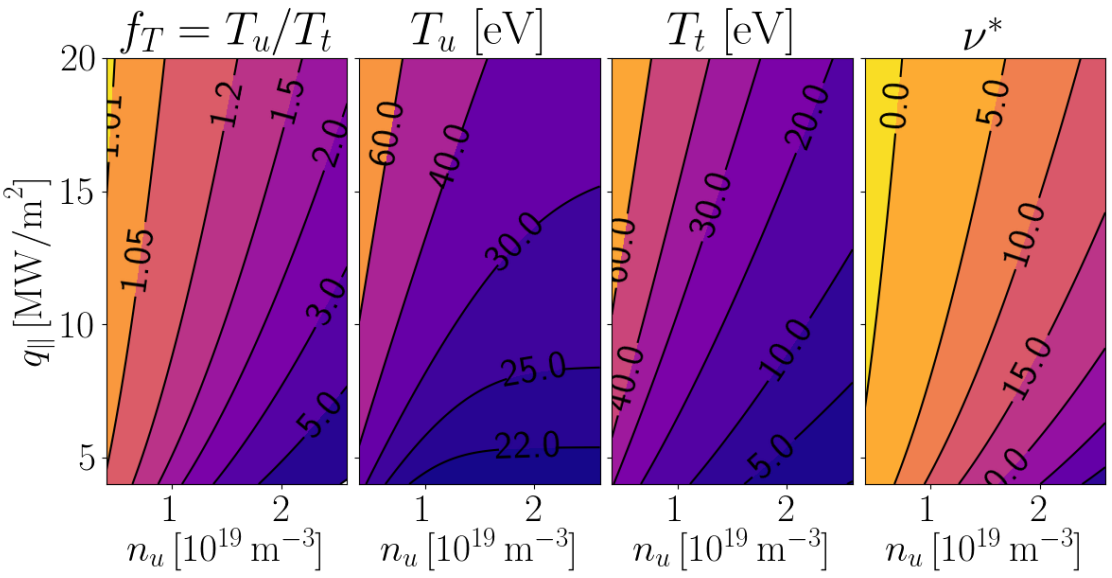


Figure 1.2: 2PM predictions for the COMPASS outer strike point ($L = 5.3$ m): the temperature gradient factor $f_T$, the upstream and target temperatures, and the plasma collisionality $\nu^*$.

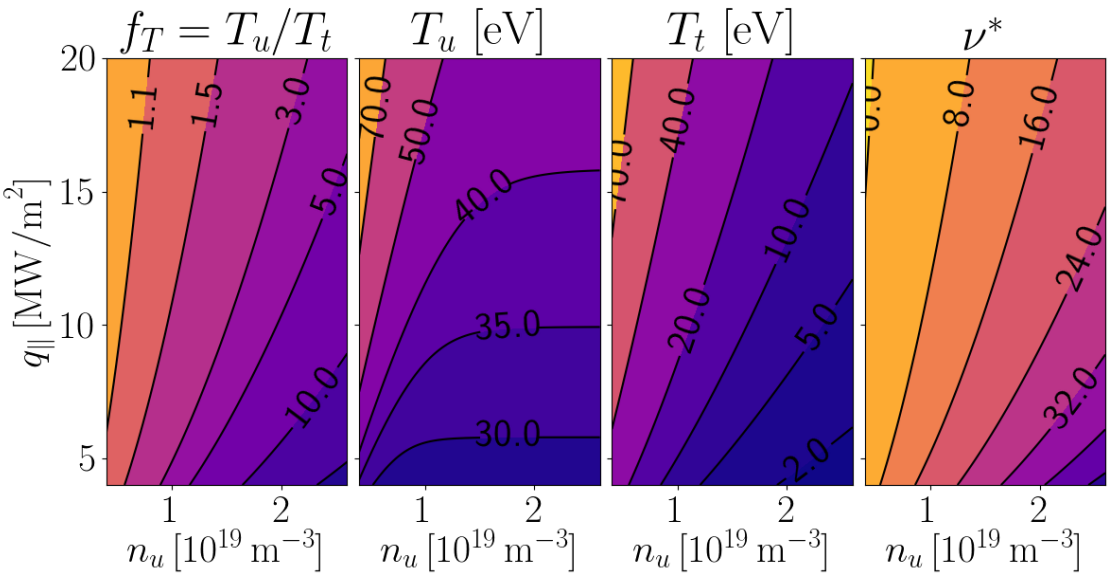


Figure 1.3: 2PM predictions for the COMPASS inner strike point ($L = 14.6$ m): the temperature gradient factor $f_T$, the upstream and target temperatures, and the plasma collisionality $\nu^*$.

is apparent that the conduction-limited regime is reached more easily on the inner target, unfortunately, this location lacks sufficient probe coverage as the new divertor array usually measures negative temperatures there. This is why the analysis in this thesis will be carried out only for the outer target, which offers a smaller window of opportunity to enter the high temperature drop SOL regime.

From the basic 2PM, the SOL transport regime for COMPASS follows as mostly sheath-limited, with a window at high densities and low heat fluxes where both targets enter the conduction-limited regime. Yet the reality may not be this simple. Many of the effects which the basic 2PM specifically rules out, such as power losses from the flux tube, may lower the experimental value of $T_t$, resulting in a greater temperature gradient than the model predicts. On the other hand, however, there are also processes forbidden in the 2PM, such as convective heat transport, which affect the edge plasma by flattening the temperature gradient. All in all, comparing the computed temperature drops to experimental temperature drops is needed to assess the SOL transport regimes of tokamak COMPASS.

# Chapter 2

# Diagnostics of tokamak COMPASS

This chapter introduces the diagnostics providing data for this thesis. Among them the most prominent are the electron temperature diagnostics, which come to a total of five: the horizontal reciprocating probe (HRCP) [18], the vertical reciprocating probe (VRCP) [19], the Thomson scattering diagnostic (TS) [20], the old divertor probe array [19], and the new divertor probe array [21]. Each of these diagnostics is located at a different place in tokamak COMPASS, both toroidally and poloidally (Fig. 2.1 and 2.2). In the theory chapter the 2PM and the SOL transport regimes were introduced; in the experimental chapter they shall be researched mainly by comparing $T_e$ profiles measured at various positions in the tokamak.

It is not only the position of the measurement that differs between these five diagnostics, but typical temporal and spatial resolution of each diagnostics is also different, as summarized in Tab. 2.1. Since this work deals mainly with steady-state quantities, the sub-microsecond resolution of the probe diagnostics is not utilised and, unless otherwise noted, the measured temperature is averaged over time scale of several milliseconds that is significantly longer than the autocorrelation time of temperature fluctuations. Further details on arrangement and parameters of the COMPASS diagnostics can be found in overview papers [22] [19] and references therein.

| $T_e$ diagnostic | $\Delta_{space}$ | $\Delta_{space,mapped}$ | $\Delta_{time}$ |
|---|---|---|---|
| HRCP | 1 mm[1] | – | 0.2 $\mu$s |
| VRCP | 1 mm[1] | 1 mm[1] | 0.2 $\mu$s |
| old divertor array | 4-5 mm | 0.3-1 mm | 0.5 ms |
| new divertor array | 3-4 mm | 0.1-0.7 mm | 0.25 $\mu$s |
| TS | 3.6 mm | 1.2-1.9 mm | 8 ms, 16 ms[2] |

Table 2.1: The spatial resolution and time resolution of the $T_e$ diagnostics used in this thesis. $\Delta_{space,mapped}$ refers to the spatial resolution after mapping onto the OMP.

[1] Refer to section 3.1.2.
[2] The TS diagnostic was upgraded in 2017, increasing the laser pulse rate two-fold. [20]

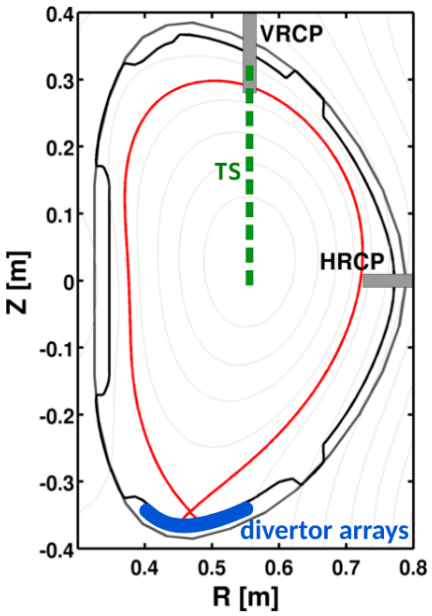


Figure 2.1: COMPASS $T_e$ diagnostics, poloidal view.

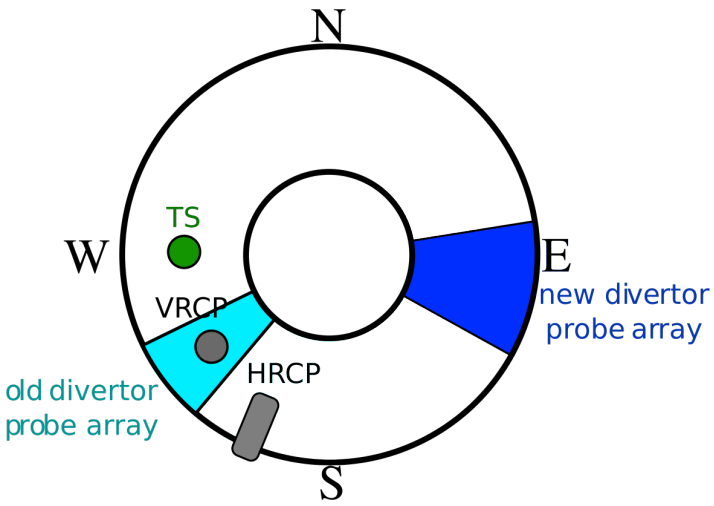


Figure 2.2: COMPASS electron temperature diagnostics, toroidal view.

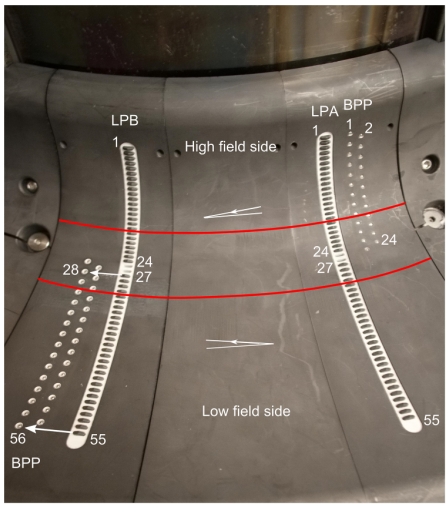


Figure 2.3: The new divertor array. 2×53 LPs and 56 BPPs in total, one BPP and two LPs at each radius - the LP in the vicinity of the BPP is in the floating mode, the other one is biased to −270 V and measures $I_{sat}$. [21]

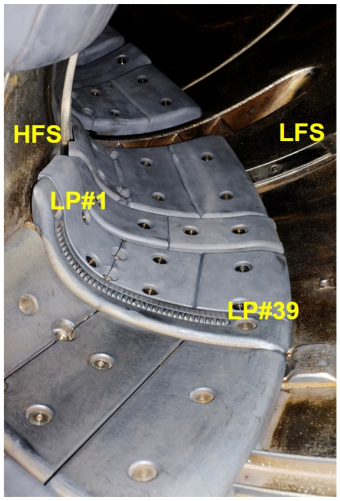


Figure 2.4: The old divertor array. 39 LPs in total, usually swept. Courtesy of M. Dimitrova.

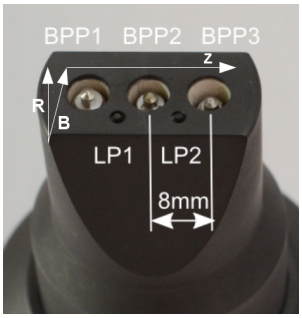


Figure 2.5: Example of a RCP head: the "classical" HRCP head [23]. Courtesy of J. Seidl.

## 2.1 Electron temperature measurements

There are three physical methods of measuring electron temperature employed in this thesis. Firstly, the HRCP, the VRCP, and the new divertor probe array all carry floating ball-pen probes (BPPs) and Langmuir probes (LPs), whose potential difference is directly proportional to $T_e$ [24]. Secondly, the old divertor probe array uses swept Langmuir probes to measure their $I$-$V$ characteristic which is then processed using the first-derivative probe technique [25]. Finally, the Thomson scattering diagnostic measures the Thomson scattering of laser photons in the plasma and infers the temperatures from the detected scattered spectra [26]. I will go further only into the probe measurements because a substantial inconsistency between the old and new divertor probe arrays is found in the experimental part and a theoretical background is needed in order to perform a discussion. For further details on the use of Langmuir probe sweeping and Thomson scattering on tokamak COMPASS, refer to [27] and [28].

### 2.1.1 Probe measurements of the electron temperature

This section will provide a simple theoretical background for $T_e$ measurements using the BPP-LP method. After introducing the probes design and operation, data interpretation will be discussed.

In plasma physics, Langmuir probes are one of the most commonly used diagnostics. Their distinctive feature as a diagnostic is that designing, manufacturing, and using a LP is very easy, but interpreting the data can be extremely difficult [29]. From the LP schema in figure 2.6, one can see that the probe consists only of a conductive (here graphite) pin, which is insulated from the probe holder and connected to a data acquisition system which reads its potential and current. The $I$-$V$ characteristic of the Langmuir probe (Fig. 2.7), on the other hand, can change shape substantially depending on plasma conditions [30]. It is sensitive to, for instance, the electron velocity distribution function, which can be resolved using the first-derivate probe technique, the plasma composition, or the presence and frequency of RF waves. This illustrates that LP data must always be used with careful consideration of what they might mean. With all that said, the ion branch of the characteristic is still typically represented by the ideal $I$-$V$ characteristic [7]:

$$I = I_{sat,i}\left(1 - \exp\frac{V_{bias} - V_{fl}}{T_e}\right), \tag{2.1}$$

where $I$ is the current measured when the bias voltage $V_{bias}$ is applied on the probe and $I_{sat,i}$ is the ion saturated current.

The simplest measurement which can be performed by a LP is the measurement of its floating potential, $V_{fl}$. In this regime, the probe is electrically insulated from the vacuum vessel and plasma particles are allowed to charge it until a current balance between electrons and ions is achieved. The floating potential follows the formula

$$V_{fl} = \Phi - \alpha_{LP} T_e, \tag{2.2}$$

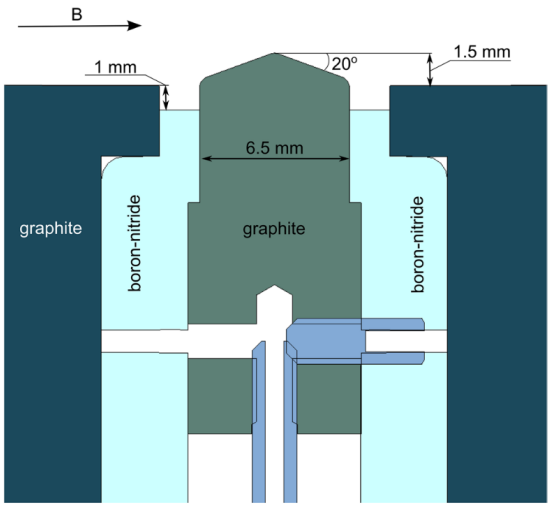


Figure 2.6: Schematic of the Langmuir probes used in the new divertor array of tokamak COMPASS. [21]

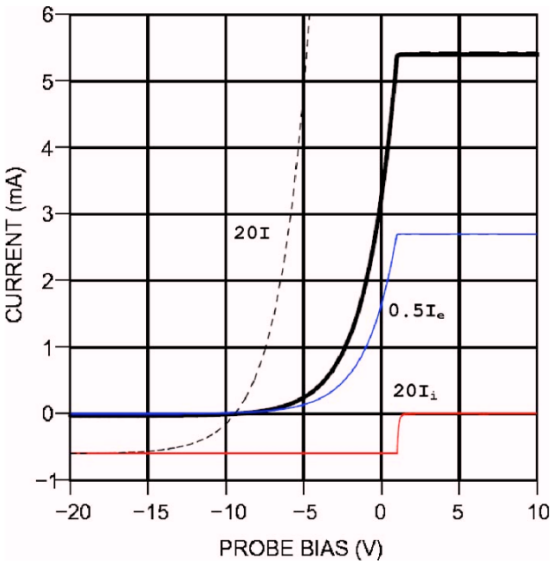


Figure 2.7: Ideal $I$-$V$ characteristic of a Langmuir probe (black) and the contributions of the electron and ion currents $I_e$ and $I_i$, respectively. [29]

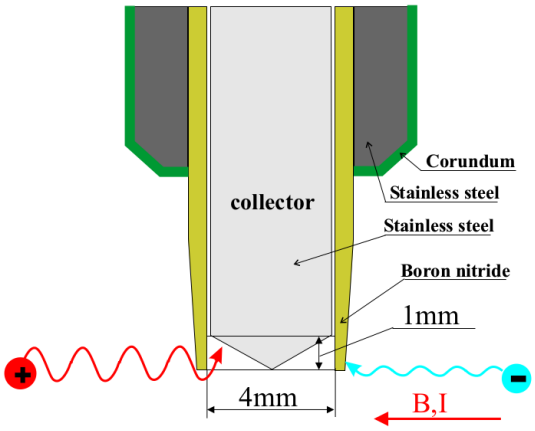


Figure 2.8: Schematic of the ball-pen probe. [31]

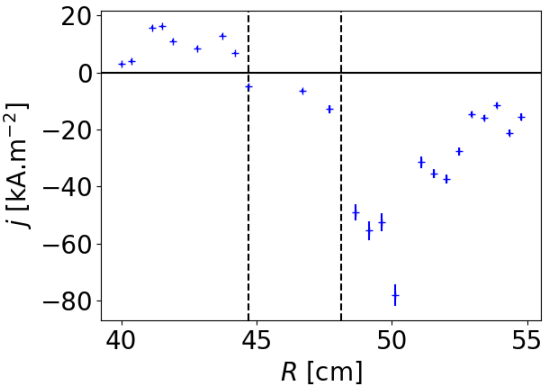


Figure 2.9: Currents flowing into the grounded divertor probes, courtesy of Jakub Seidl. Discharge #15976.

where $\Phi$ denotes the local plasma potential and $\alpha_{LP} = 2.8$ [7] is a coefficient depending mainly on the probe geometry, plasma composition, and the magnetic field [31]. Here it was evaluated for cylindrical Langmuir probe in deuterium plasma and $T_i = T_e$. LP floating potential measurement makes up one half of $T_e$ measurement using the BPP-LP technique.

The ball-pen probe, figure 2.8, is, in essence, very similar to the Langmuir probe. The key difference is that while a LP usually protrudes from the surrounding material to be in direct contact with plasma, the BPP pin is sunk below the surface, hidden in a ceramic shielding tube. This should, in theory, prevent a large part of electrons from reaching the pin due to their small Larmor radius. Ions, in contrast, can still impinge on the pin, raising the ratio of ion to electron current to, ideally, unity [32]. Even though this intuitive explanation is somewhat oversimplified and numerical particle-in-cell simulations show that plasma particles are transported towards the collector with significant contribution of $\mathbf{E}\times\mathbf{B}$ drifts created by self-consistent electric fields forming inside the shielded tube [33], the real transport mechanism still leads to the suppression of the electron current reaching the collector. This suppression affects the $\alpha$ coefficient in Eq. (2.2) of such a pin, as it obeys the relation

$$\alpha = \ln \frac{I_{sat,e}}{I_{sat,i}}$$

where $I_{sat,e}$ and $I_{sat,i}$ are the electron and ion saturated currents, respectively. If $I_{sat,e} = I_{sat,i}$, then $\alpha = 0$ and the floating potential of the pin is directly equal to the plasma potential $\Phi$. In experimental measurements performed on ASDEX [34], this coefficient was found to be $\alpha_{BPP} = 0.6 \pm 0.3$. Thus the ball-pen probe floating potential is very close to, though not equal to, the plasma potential $\Phi$.

Electron temperature measurement on both the reciprocating probes and the new divertor array is based on the fact that $\alpha_{LP} \neq \alpha_{BPP}$. All three of these diagnostics contain a number of floating ball-pen and Langmuir probes located close to each other, so that one may infer the electron temperature from their voltages as

$$T_e = \frac{V_{fl,BPP} - V_{fl,LP}}{\alpha_{LP} - \alpha_{BPP}} \tag{2.3}$$

For both of the reciprocating probes, $\alpha_{LP} - \alpha_{BPP} = 2.2$ [18], while on the divertor the $I$-$V$ characteristics give $\alpha_{LP,div} - \alpha_{BPP,div} = 1.4$ due to the different geometry of the LPs [21].

The BPP-LP method, in comparison to sweeping the LP to obtain the $I$-$V$ characteristic and determining the temperature either by fitting the ideal characteristics (2.1) or by the first-derivative probe technique, has both advantages and disadvantages. While the time resolution of the latter method is limited by the sweeping frequency, $T_e$ computed from $V_{fl,BPP}$ and $V_{fl,LP}$ has the same sampling frequency as the two voltages. In the conditions of COMPASS, for instance, one data point from the old divertor array corresponds to 2,000 data points from the new divertor array. This allows the BPP-LP method to investigate plasma turbulence, ELMs, or fast plasma shifts. Both of the methods, however, contain inherent errors. The BPP and LP measurements physically cannot be carried out at the same place, which

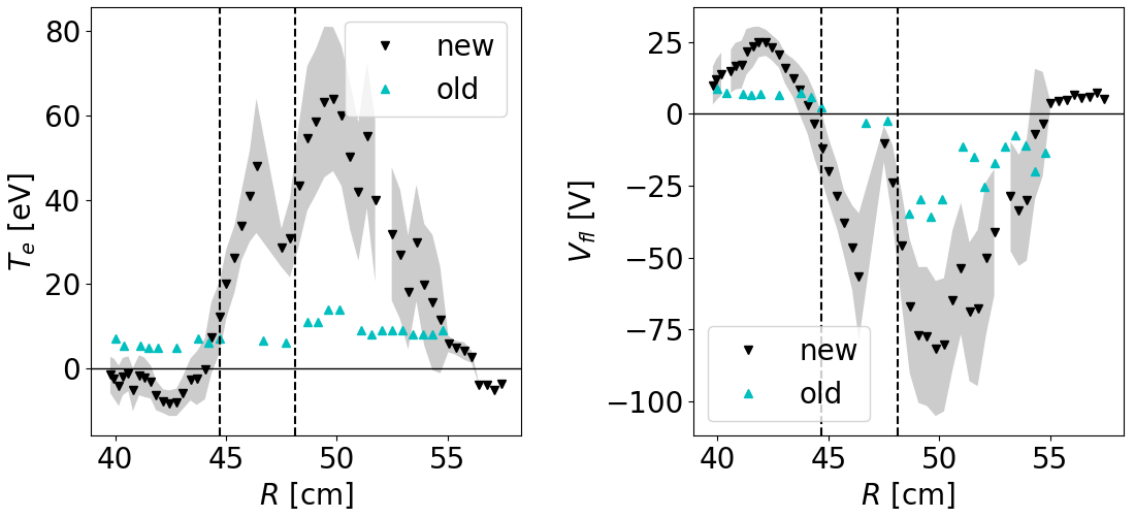


Figure 2.10: Comparison of $T_e$ and $V_{fl}$ measurement of the old and new COMPASS divertor probe array. The shaded area represents standard deviation of temperature fluctuations. Discharge #15976.

introduces errors due to presence of finite electric fields and spatial gradients of $T_e$.[1] On the other hand, the sweeping method needs some time to collect enough data for the $I$-$V$ characteristic, thus suffering from not sampling at one time instant, which brings problems due to large sensitivity of the fit on distortion of the $I$-$V$ characteristic by temporal fluctuations of plasma parameters. An interesting issue, explored in [35], is that the BPP-LP method is not able to differentiate between a single and a bi-maxwellian electron velocity distribution, instead measuring the higher temperature of the two. Conversely, interpreting the $I$-$V$ characteristic using the first-derivate probe technique employed in the old divertor array, bi-maxwellian distribution can be detected and measured. On the whole, however, when interested in temperatures averaged over a long time period, there should not be a substantial difference in the electron temperatures measured by the two methods.

Thus it was quite a surprise that after the new divertor array was installed in 2016, its $T_e$ was found to be systematically higher than that of the old divertor array, figure 2.10. Floating potentials of the two arrays are also not the same, with the new divertor array giving more negative $V_{fl}$ and thus measuring a higher temperature as Eq. (2.3) dictates. The reason for the discrepancy has not been fully resolved yet, but a significant role may be played by non-axisymmetric non-ambipolar electric currents flowing into the divertor.

The issue of anomalous divertor LP measurement was examined already at the previous COMPASS installation site, Culham, UK, where distortions of electron density profiles were observed which changed significantly upon reversing $B_T$ [36].

[1] This is not an issue in the measurements studied here. The divertor probes are spaced in the toroidal direction only (Fig. 2.3), measuring due to shallow incident angle of the magnetic field at two very close field lines. The pins on the reciprocating probes (Fig. 2.5) are spaced mainly poloidally and any perturbations of the measurement due to non-homogeneous temperature or potential field will be averaged out to zero during time averaging, assuming the mean temperature and potential are poloidally symmetric.

The article offered the explanation that the parallel thermoelectric and Pfirsch-Schlüter currents may be responsible for changing the plasma potential, and thus forming electric fields that drive particles in various directions via $\mathbf{E} \times \mathbf{B}$ drifts. The drift direction depends on the position relative to the strike points, and so the oscillating drift profile distorts the $T_e$, $V_{fl}$ and $n_e$ profiles in a manner not unlike the "teeth" measured by the new divertor array on the current COMPASS (Fig. 2.10). Indeed, currents of the same direction and magnitude as in [36] were found on tokamak COMPASS, figure 2.9. Change of plasma and floating potential due to the presence of parallel SOL currents is described in more detail in [37], where the authors show on the case of DIII-D that even for moderate L-mode conditions the perturbation of the floating potential can reach more than 100 V. This adds to the credibility of explaining the $V_{fl}$ and $T_e$ profile distortion, possibly including also the negative temperature on the HFS, with non-ambipolar currents flowing into the grounded divertor. However, since there is currently no theory that could be used to assess effect of the parallel currents on the ball-pen probe measurements, a definitive conclusion cannot be drawn.

Assuming that the parallel currents are responsible for distorting the temperature and floating potential measurements at the divertor, however, brings new questions. Why do the currents affect the two probe arrays in a different way? Is it because the COMPASS tokamak is toroidally asymmetric, with the slight misplacement of the central solenoid playing a role? Is it possible to remove the effects of the parallel currents and retain the original profiles of electron temperature? If such a correction is possible, will the resulting profile be consistent with the old, or the new array? Answering these questions is outside the scope of this thesis, but the issue will be addressed in another, unique way. Measuring electron temperature with five different diagnostics offers the opportunity to perform various comparisons. For instance, using the 2PM it is possible to calculate the temperature drop along the flux tube, meaning that $T_u$ can be inferred from a known $T_t$. Finding this $T_u$ on the upstream temperature profile will then, in turn, yield the separatrix position. This separatrix position can then be compared with the magnetic reconstruction results or with the location of the velocity shear layer, providing a validation for the initial $T_t$. In this manner, the discrepancy between the old and the new divertor probe array will be addressed in section 3.1.4.

### 2.1.2 Other quantities inferred from probe measurements

Using three spatially close probes, a ball-pen probe, a floating Langmuir probe, and a Langmuir probe in the $I_{sat}$ regime, it is possible to measure the following quantities:

- electron temperature $T_e = \dfrac{V_{BPP} - V_{fl}}{\alpha}$,
- electron parallel heat flux $q_{\parallel} = \gamma \dfrac{I_{sat} T_e}{A}$,

- electron density $n_e = \dfrac{I_{sat}}{feA\sqrt{2eT_e/m_i}}$, and
- electron pressure $p_e = en_eT_e$,

where $\gamma = 7$ is the sheath heat transmission coefficient for deuterium plasma, no secondary electron emission and $T_e = T_i$ [7], $A$ is the effective probe collecting area, $e$ is the elementary charge, and $m_i$ is the deuteron mass. The ions charge is taken as $Z = 1$ and $\alpha = 2.2$ and 1.4 for the reciprocating probes and the new divertor array, respectively.

The value of the effective probe collecting area deserves special attention. In the case of $T_i = 0$ eV, $A$ would be just the area of the geometrical projection of the pin onto the magnetic field. However, since $T_i$ in the SOL is comparable or even larger than $T_e$ [A. Dvornova, Master thesis 2016], ion Larmor radius has to be taken into account. Recently, a comparison of the density derived from the HRCP using the formula above, results of particle-in-cell simulations, and the density measured by the Lithium Beam Emission Spectroscopy diagnostics was performed for the geometry of the COMPASS probe head shown in Fig. 2.5 [A. Podolnik et al, submitted to PPCF]. The effective collection area was found to be by a factor of $q_A = A/A_\perp =$ 3-7 larger than a simple geometrical projection (one side) of a cylindrical pin $A_\perp = dh$, where $d = 0.9$ mm and $h = 1.5$ mm is the diameter and height, respectively, of the Langmuir pins used on the COMPASS probe heads. Since the ratio $S/A_\perp = 3.6$, where $S$ is the full surface of the pin $S = \pi d(h + d/4)$, is well within this range, for simplicity the pin collecting area will be assumed equal to the full surface of the pin, $A_{HRCP} = S = 4.9$ mm$^2$. For the new divertor probes $A_{div} = 2.8$ mm$^2$ are taken from [21]. Discussion of the impact of the rather large uncertainty in $A$, which influences absolute values of the measured density and parallel heat flux both on the midplane and divertor, on the results of comparison of divertor and midplane profiles will be presented in section 3.2.3.

Another possible source of error in calculating the listed physical quantities is the value of the sheath heat transmission coefficient $\gamma$, which depends on the unknown ratio $T_i/T_e$ and on the magnitude of the secondary electron emission [38]. Even though recently a very good match was found between the parallel heat flux from the new divertor array (using $\gamma = 7$ and $A_{div} = 2.8$ mm$^2$) with an independent measurement of the heat flux by an infra-red camera [21], this in principle fixes only the ratio $\gamma/A_{div}$ and not the value of $\gamma$ itself. The uncertainty in $A_{div}$ can be rather large, as discussed in the previous paragraph. In general, experimental measurements of are $\gamma$ are rare and give rather large uncertainties [38].

For the data analysis in this thesis, only average values of the measured quantities are needed. Thus every profile from HRCP and VRCP drawn and processed here is smoothed using a lowpass filter with the cut-off frequency 200 Hz. This specific frequency is a compromise between preserving the profile shape and filtering out the sawtooth oscillations, whose typical frequency is 500 Hz. As discussed in detail in section 3.1.2, this means that the spatial resolution of the processed profiles is 1-2 mm.

# Chapter 3

# Experimental data analysis

In this chapter, the data measured on tokamak COMPASS will be discussed within the frame of the two-point model, aiming to investigate the SOL transport regimes that this tokamak may enter. The primary tool will be to compare radial electron temperature profiles, which are drawn from five experimental diagnostics and from the 2PM, where experimental $q_{\parallel}$, $n_u$, and $L$ serve as input data. From collisionality and temperature drops along the field line, both in the experiment and in the model, the SOL transport regime of tokamak COMPASS will be inferred.

This chapter is divided into two parts. The first one is concerned with correcting the systematic errors in the magnetic equilibrium reconstruction and the second one contains the $T_e$ analysis described above. The issue of mapping, which the first part covers, is vital for any SOL profile analysis. The reason is that any profile comparison must be made on a common $x$ axis, which is commonly chosen as the $R$ coordinate at the OMP, meaning that any measurement carried out elsewhere must first be mapped onto this location. The only mean of mapping available is the magnetic equilibrium reconstruction programme, EFIT++ on COMPASS, which has been known to displace the OMP separatrix by 1-2 cm. Unfortunately, when dealing with regions of such steep gradients as near the OMP separatrix, 1 cm is a lot. Displacing a mapped profile by this amount can render any comparison of it worthless. To give an example, in figure 3.1 four $T_e$ profiles are plotted using only the uncorrected EFIT mapping.[1] The HRCP profile (red) was measured on the OMP, so it is considered spatially accurate. Considering the fast thermal transport along field lines, it is obvious that $T_e = 20$ eV measured on the OMP is inconsistent with $T_e = 1$ eV observed on the same magnetic surface on the top of the plasma. It is apparent that even though EFIT considers these two points to be magnetically connected, in reality this is not so and a correction is needed to the mapping before any profile comparison is perfomed. This is the reason why a section investigating the OMP separatrix position must precede the actual SOL transport analysis.

[1] Unfortunately there is no discharge available in the COMPASS database where all five $T_e$ diagnostics were measuring at once.

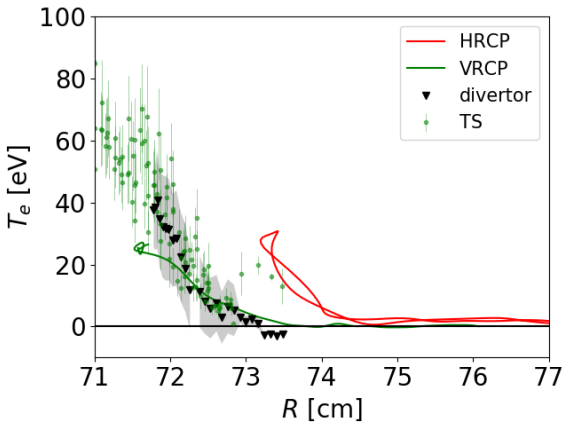


Figure 3.1: $T_e$ profiles from HRCP, VRCP, TS, and the new divertor array, mapped with EFIT++ onto the OMP without any correction. Discharge #15497, D-shaped plasma.

## 3.1 Separatrix position on the OMP

The magnetic equilibrium reconstruction programme EFIT++ has been known to display a systematic error in the exact location of the separatrix. This error seems to change with the poloidal angle, reaching a maximum at the OMP where the measuring magnetic coils are the furthest from the plasma, resulting in an uncertainty greater than at the divertor or at the plasma top. However, while this should cause only a random error in the equilibrium reconstruction, there is also a systematic shift which depends, most notably, on plasma shape. In my Bachelor's thesis [39] I showed that the position of the velocity shear layer (VSL) $E_r = 0$ as measured by the HRCP is shifted from the EFIT $R_{sep}$ on average by $-0.5$ cm for circular plasmas and 2.5 cm for D-shaped plasmas. Here I expand this analysis in several directions. Firstly, the statistical set is larger since tokamak COMPASS has performed approximately 6000 discharges over the last three years. Secondly, beside the VSL position on the OMP I also employ other means of estimating the EFIT systematic error, namely:

- manually shifting the VRCP $T_e$ profile mapped to midplane so that it lies on top of the HRCP $T_e$ profile, assuming zero temperature gradients along field lines in the near SOL
- shifting the profile so that HRCP and VRCP VSLs overlap
- shifting the profile to overlay the boundary between the near and far SOL (obtained by fitting the HRCP and VRCP $T_e$ profile with a double exponential)
- calculating $T_u$ from the 2PM (using $P_{SOL}$, $L$, and $T_t$ or $n_u(R)$ as input, refer to section 3.1.4) and finding its position on the HRCP profile to obtain the separatrix position

The issue of the exact separatrix position has already been covered on many tokamaks [13][14][40]. There is a number of proposed methods for finding the magnetic separatrix, or at least correcting the systematic error of the magnetic equilibrium reconstruction, such as:

- The separatrix lies just outside of the location where the $T_e$ gradient is the largest, with the exact distance related to the $T_e$ SOL width $\lambda_T$. [13]
- Assuming that the magnetic equilibrium reconstruction has no error on the divertor and the SOL is in the sheath-limited regime (no pressure losses), overlay the divertor and OMP electron pressure profiles. [13]
- Making the same assumption, overlay the electron temperature profiles. [13]
- Assume that the 2PM is a good model of the SOL and use it to predict $T_u$ from $P_{SOL}$ and $\lambda_T$ under the assumption of the conduction-limited regime, then find $T_u$ on the OMP electron temperature profile. [13]
- The results of the magnetic equilibrium reconstruction may be more accurate if currents running along the separatrix were allowed to be finite. [13]
- The separatrix lies at the location of the maximum shear $\left|\frac{\mathrm{d}^2\Phi}{\mathrm{d}R^2}\right|$, where $\Phi$ may be measured by:
  - a ball-pen probe,
  - a swept Langmuir probe,
  - a floating Langmuir probe and a swept Langmuir probe, subtracting $2.5T_e$ from $V_{fl}$, or
  - a floating Langmuir probe, neglecting the $T_e$ contribution to $V_{fl}$. [14]
- Performing a cross-corelation between two poloidally separated probes (any probe with a high sampling frequency is sufficient), find the position where the poloidal phase velocity changes sign. [14] Since plasma flow is dominated by the $\mathbf{E} \times \mathbf{B}$ drift, this effectively corresponds to finding radius with $E_r = 0$ or local maximum of $\Phi$.
- Overlay the $V_{fl}$ profiles obtained by a reciprocating probe and by wall probes in the limiter configuration. [14]

There are also a few other methods which may be possible to use on COMPASS:

- Find the "blob birth zone" on the profile of $I_{sat}$. This method is based on the picture of interchange turbulence in the edge plasma, where instabilities on the separatrix cause filaments of colder SOL plasma to exchange place with filaments of hotter confined plasma and then continue propagating in the same direction. The cold filaments are seen as negative fluctuations on a gaussian background, resulting in a negative skewness of the probability distribution function (PDF). On the other hand, in the SOL a positive $I_{sat}$ PDF skewness is typically observed, showing the occurence of hot plasma filaments, or "blobs" as they are seen in the poloidal cross-section. The radial location where the PDF skewness is zero is then called the blob birth zone, and numerical models of SOL turbulence show that it is located just inside the separatrix. [41]
- Use the Vacuum Toroidal Harmonics method, which reconstructs the $\Psi$ function outside the main plasma by decomposing it into toroidal harmonics. By extrapolating to the plasma edge, the separatrix may be found. [42]
- Use the position where a floating Langmuir probe abruptly becomes self-emissive, as this indicates an abrupt increase in the incident heat flux.

Evidently there is a multitude of methods based on various assumptions which allow to calculate the separatrix position or correct the mapping error. The ones implemented in this thesis have one of two things in common: they are based on data

from my previous work (BPP potential maximum detection [39] and the detection of the boundary between the near and far SOL [43]) or they are directly connected to the subject of this thesis (overlay of upstream $T_e$ profiles and 2PM calculation of $T_u$). The other methods may be implemented in the future.

In this section, each of the methods will be detailed as to the theoretical background and data processing. Then, all four methods and some of their combinations will be compared statistically and the best way to correct the EFIT mapping will be chosen. It is more difficult to choose the best candidate for the separatrix position, however, by reaching a self-consistent prediction of upstream and target temperature profiles on COMPASS using the 2PM, it will be found that simply the EFIT separatrix corrected to achieve agreement between HRCP and VRCP temperature profiles is a good estimate of the real separatrix position.

### 3.1.1 Manual overlay of HRCP and VRCP $T_e$ profiles

Assuming a separatrix temperature 30 eV, electron thermal conductivity on this magnetic surface is $k = \kappa_{0e} T_e^{7/2} = 3 \times 10^8$ Wm$^{-1}$K$^{-1}$, which is 6 orders of magnitude higher than copper at room temperature. This conductivity should be enough to ensure that within the confined plasma and on the separatrix, $T_e$ is constant along any magnetic surface. In the SOL, on the other hand, temperature drops along the field line may occur depending on the average temperature, the connection length, and the plasma density. Coming from the COMPASS operational space analysis (Fig. 1.2), however, the SOL of this tokamak may be expected feature significant temperature gradients only in high densities. Furthermore, most of the temperature drop will then occur within the divertor volume and not while the field line is still close to the confined plasma. It is therefore justifiable to assume that temperature profiles measured on the VRCP and the HRCP are, essentially, the same.

Figure 3.2 shows $T_e$ profiles in discharge #8870 as measured by the horizontal and vertical reciprocating probes, with the VRCP profile mapped onto the OMP (left) and then shifted so that it overlays the HRCP profile (right). It is apparent that the profiles are not the same in the far SOL, with the VRCP $T_e$ falling rapidly to zero when HRCP $T_e$ is still 5-10 eV. This is most likely caused by the combination of two factors: that most of the cross-field transport into the SOL occurs near the OMP, and that between the OMP and the top of the plasma there is only a small clearance, indicated in figure 3.3. In fact, from the uncorrected mapping it is obvious that EFIT places the separatrix approx 1 cm inward from its actual location, so the real clearance is probably even smaller. This means that much of the power transported along the flux tube from the OMP impinges on the limiter between the HRCP and the VRCP, meaning that the VRCP far SOL is shadowed from the heat source and thus much colder.

Bearing this in mind, the manual overlay was performed prioritising the high temperature part of the profile, left to the "knee" where $T_e$ begins growing rapidly. Discharges where both the probes measured $T_e$ but at least one of them did not reach this "knee" were excluded from the analysis. 149 discharges were processed

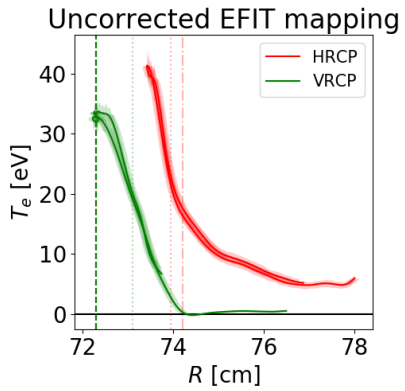


Figure 3.2: HRCP and VRCP $T_e$ profiles, as mapped by EFIT (left) and shifted so that they lie on top of each other (right). Discharge #8870. Dashed line $R_{EFIT}$, dotted $R_{BPP}$, dash-dot $R_{break}$.

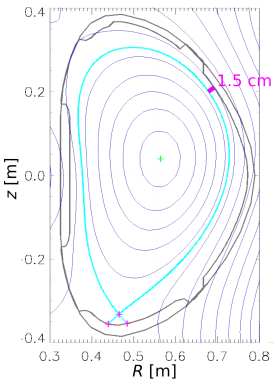


Figure 3.3: Magnetic equilibrium reconstruction of discharge #8870. The cyan line marks position of the LCFS.

in total, from #6878 to #15497.

### 3.1.2 BPP potential maxima

The ball-pen probe floating potential profile typically exhibits a maximum in the near SOL. Theory provides an explanation why plasma potential should reach a stationary point in the edge plasma and why this should be a maximum. Electric radial field $E_r = -\frac{\mathrm{d}\Phi}{\mathrm{d}r}$ combined with the predominantly toroidal magnetic field of a tokamak causes a poloidal $\mathbf{E} \times \mathbf{B}$ drift, whose magnitude is $v_p = E_r/B$. Since $E_r$ changes radially, so does $v_p$, causing shear flows which can tear turbulent structures escaping from the main plasma apart, reducing turbulent transport and acting as a transport barrier. Turbulent models such as [44] show that this shear is largely generated by momentum transfer from the turbulent structures themselves and is thus localized close to the separatrix in the region of large turbulent drive. This means that $E_r = 0$, or $\Phi$ being stationary, should signify the vicinity of the separatrix. The reason why this stationary point should be a maximum in particular requires a slightly longer explanation.

The key argument why the plasma potential should have a maximum at the separatrix is that in the region of closed magnetic surfaces, different physical processes dictate the potential profile than in the region of open magnetic field lines. Inside of the separatrix, the radial component of the force balance equation is

$$E_r = \frac{1}{nZe}\frac{\mathrm{d}p_i}{\mathrm{d}r} - (\mathbf{u} \times \mathbf{B})_r \,,$$

where $Z$ is the ion charge, $p_i$ is the ion pressure and $\mathbf{u}$ is the plasma velocity.

Assuming low velocities we may neglect the second term and write

$$E_r = -\frac{\mathrm{d}\Phi}{\mathrm{d}r} \sim \frac{\mathrm{d}p_i}{\mathrm{d}r}.$$

Since the ion pressure decreases with increasing $r$, $\frac{\mathrm{d}p_i}{\mathrm{d}r} < 0$ and $\frac{\mathrm{d}\Phi}{\mathrm{d}r} > 0$. Therefore, the plasma potential $\Phi$ increases with $r$ in the region of closed magnetic field lines.

The situation is entirely different in the region of open magnetic field lines. Here the plasma potential is dictated by the fast parallel transport to the wall. In the sheath-limited SOL, $\Phi$ does not change significantly along the magnetic field line, following the formula

$$\Phi = V_{divertor} + \alpha T_e,$$

where $V_{divertor}$ is the divertor potential (zero for a grounded divertor), $\alpha \approx$ 2-3 along the field line in deuterium plasma ($\alpha = 2.8$ at the divertor sheath), and $T_e$ is the local electron temperature. Since in the SOL $T_e$ falls with increasing $r$, $\Phi$ also decreases with $r$.

These are the physical reasons why the plasma potential, or the potential of the ball-pen probe, should form a maximum near or at the separatrix. Interestingly, the Langmuir probe floating potential also forms a maximum in the SOL. However, due to the large contribution of the electron temperature, $V_{fl,LP} = \Phi - 2.8T_e$, it is moved much further into the SOL and does not provide separatrix position as reliable as the BPP, where $V_{fl,BPP} = \Phi - (0.6 \pm 0.3)\, T_e$. Continuing this train of thought, it would actually be more proper not to detect the BPP potential maximum, but first subtract the $T_e$ contribution. Such a correction was not performed in the data presented here for two reasons. First, it introduces an error into the data because $T_e$ measurement is non-local. Second, it limits the database of BPP maxima because electron temperature measurement is not always available. This is why, for the separatrix detection, uncorrected BPP potential was used. This can be expected to result into a systematic error, which shifts the $V_{BPP}$ peak several milimeters outwards the $\Phi$ peak, figure 3.4.

Based on the method of maximum detection in the noisy BPP signal, the approximate error in $R_{BPP,max}$ can be inferred. Prior to the automatic maximum detection, a lowpass filter with the cut-off frequency 200 Hz was applied to the signal. This particular frequency was chosen as middle ground between the sawtooth oscillations (typically at 500 Hz) and preserving the profile shape. But one can also arrive at this number by considering the probe movement speed and the spatial resolution required of the profile. The maximum velocity of the reciprocating probes is approximately 1 mm/ms and the mean velocity is around 0.5 mm/ms. As plotted in figure 3.5, the raw record of the probe position contains some noise as well and its smoothing introduces an inherent random error in $R$ of approximately 1 mm. Therefore the spatial resolution of $V(R)$ cannot be lower than 1 mm. Capping this resolution by the factor of two, one may require the spatial resolution of 2 mm. Considering the maximum probe velocity 1 mm/ms, 2 mm translates to 1 sample per 2 ms, a sampling frequency of 500 Hz. The Nyquist frequency of such a time series is 250 Hz, which is close to the used 200 Hz cut-off, confirming the choice made in data processing. The conclusion is that the random error of the $V_{BPP}$ maximum detection is estimated to be 2 mm.

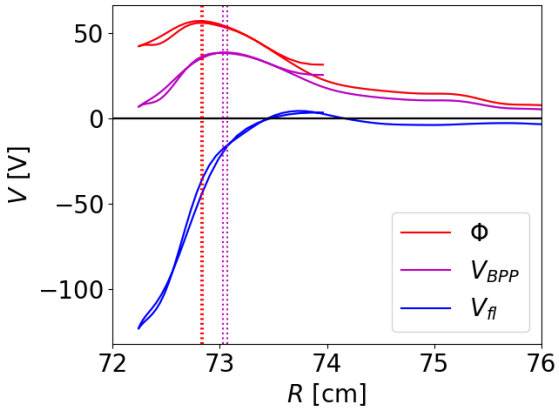


Figure 3.4: Shift of the detected maximum when the $T_e$ contribution to BPP potential is subtracted. HRCP, discharge #6878.

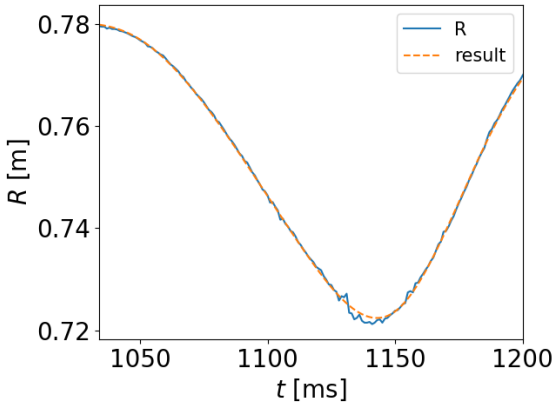


Figure 3.5: The raw and smoothed radial axis used in all radial plots. HRCP, discharge #6878.

On the HRCP, BPP potential maximum was detected in 409 discharges and on the VRCP in 202 discharges. These two sets have 116 discharges in common.

### 3.1.3 Boundary between the near and far SOL

In many tokamaks, a steepening of the parallel heat flux profile in the SOL near the separatrix has been observed. This so-called narrow feature has been called the near SOL, as opposed to the remaning far SOL [45]. In my research project [43], submitted in 2016, I investigated the SOL width of the near and far SOL on tokamak COMPASS using a broken exponential fit,

$$q_{\parallel}(R) = \begin{cases} q_{\parallel 0} \cdot \exp\left(-\dfrac{R - R_{break}}{\lambda_{near}}\right), & R < R_{break} \\ q_{\parallel 0} \cdot \exp\left(-\dfrac{R - R_{break}}{\lambda_{far}}\right), & R > R_{break} \end{cases} \tag{3.1}$$

where $\lambda_{near}$ and $\lambda_{far}$ are the respective SOL widths, $q_{\parallel 0}$ is the heat flux at the boundary between the two SOLs, and $R_{break}$ is the position of this boundary. An example of such a fit performed on electron temperature can be seen in figure 3.6. While the research project was largely concerned with $q_{\parallel}$ profiles, the routines can be used freely to any quantity which exhibits the double exponential shape, including the electron temperature. Two outputs of this fitting are used in this thesis: $\lambda_{near,q}$ is used for 2PM predictions in section 3.1.4, and $R_{break,T}$ is regarded as a location in the SOL detectable both on the HRCP and the VRCP.[2] Making the assumption that the near SOL ends at the same magnetic surface for all poloidal locations, overlaying

[2]If the clearance mentioned in the previous section is small, it shows on the VRCP $T_e$ profile as an abrupt end of a rather short far SOL. The profiles where the clearance is so small that the $R_{break}$ position is affected were excluded from the fitting.

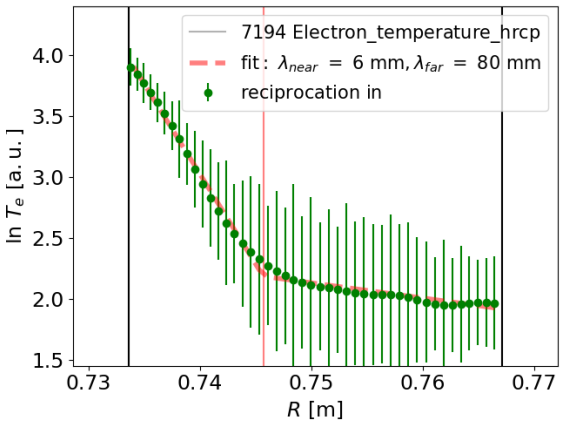


Figure 3.6: An example $T_e$ fit by a broken exponential. HRCP, discharge #7194. The errorbars show one standard deviation of the fluctuations.

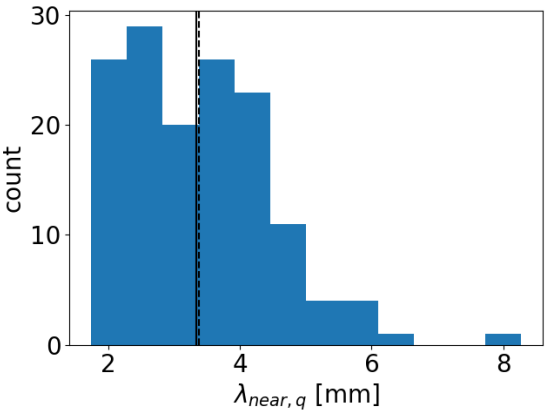


Figure 3.7: Histogram of SOL widths $\lambda_{q,near}$ measured on COMPASS in D-shapes plasma. The solid line signifies the median, 3.34 mm, the dashed line is the mean, 3.37 mm. The standard deviation of the distribution is 1.1 mm.

$R_{break}$ from HRCP and VRCP becomes a way to correct the EFIT mapping. It is not, however, a viable method for separatrix position detection, as illustrated in section 3.1.6.

Out of 476 COMPASS discharges where $T_e$ was measured well on the HRCP, 204 yielded converged fits of the near and far SOL. (The rest of the discharges either featured profiles unsuitable for fitting, due to shallow reciprocations or profile deformities, or their fits did not converge.) The VRCP, which is generally less used than the HRCP, produced 71 discharges good for fitting out of 193 candidates. $R_{break,T}$ was obtained simultaneously in 39 discharges.

### 3.1.4 Separatrix inferred from the 2PM $T_u$

The basic two-point model allows to calculate the upstream temperature of each individual flux tube as

$$T_u = \left( T_t^{7/2} + \frac{7}{2} \frac{q_\parallel L}{\kappa_{0e}} \right)^{2/7} \tag{3.2}$$

where $T_t$ is the target temperature of the flux tube in question, $q_\parallel$ is the heat flux travelling toward the target, and $L$ is the flux tube length. If one uses the target temperature at the strike point, $q_\parallel$ at the OMP separatrix, and the connection length just outside the OMP separatrix as input, the electron temperature at the separatrix $T_{sep}$ is obtained. This value can then be used to find the separatrix position via comparison with an experimental $T_u$ profile.

The problem with using this method is that it requires already knowing the separatrix position for evaluating all three input quantities. To circumvent this, the user

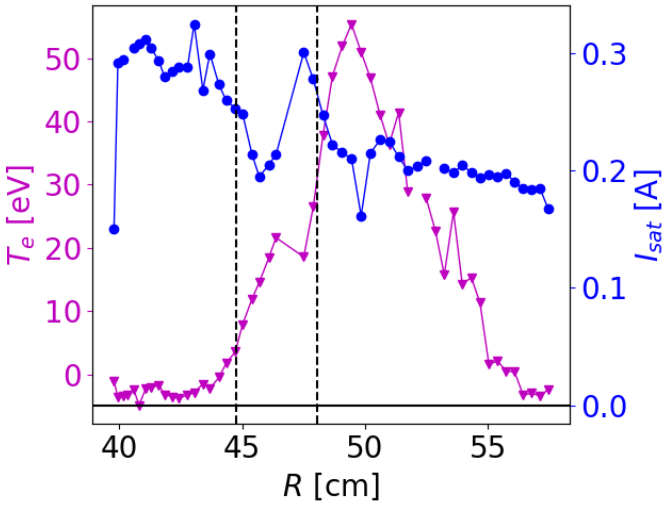


Figure 3.8: $I_{sat}$ (blue) and $T_e$ (magenta) profiles as measured by the new divertor array. The dashed lines are EFIT strike points. Discharge #15973.

must employ approximations, which all feature a various degree of inaccuracy. The resulting $T_u$ is luckily not very sensitive to inaccuracies within a factor of two due to the power 2/7. First, the approximations of $q_\parallel$ and $L$ will be presented, and then two ways to work with $T_t$ will be shown.

The parallel heat flux in the flux tube just outside the separatrix may be calculated using the power crossing the separatrix $P_{SOL}$ and the flux tube cross section $A_\parallel$,

$$q_\parallel = \frac{P_{SOL}}{A_\parallel}. \tag{3.3}$$

The radial extent of the flux tube is the near SOL width $\lambda_{near,q}$ and its poloidal extent is $4\pi R_{sep}^{OMP} B_{pol,sep}^{OMP} / B_{total,sep}^{OMP}$. In this analysis, $P_{SOL}$, $R_{sep}$ and the magnetic fields were taken from the EFIT code, and $\lambda_{near,q}$ was obtained by fitting the $q_\parallel$ profile or set to the representative value 3.4 mm if no fit was available. This value can be obtained as either the mean or median of all the near SOL widths measured in the divertor configuration, Fig. 3.7. The standard deviation of the data set is 1.1 mm, which is acceptable due to the final exponent 2/7 as argued above.

The second input of Eq. (3.2) is the connection length $L$. This was also taken from EFIT, under the assumption that even though the separatrix is systematically shifted in the magnetic equilibrium reconstruction, the connection length calculated just outside the EFIT separatrix is a good representative for the actual connection length just outside the real separatrix. This assumption will be used throughout this chapter, as magneetic field line tracing is the most accurate way to estimate $L$ but the connection length has a rather steep profile, so its radial placement must be as accurate as possible.

The final input of Eq. (3.2) is the target temperature $T_t$. Here the mentioned two methods diverge.

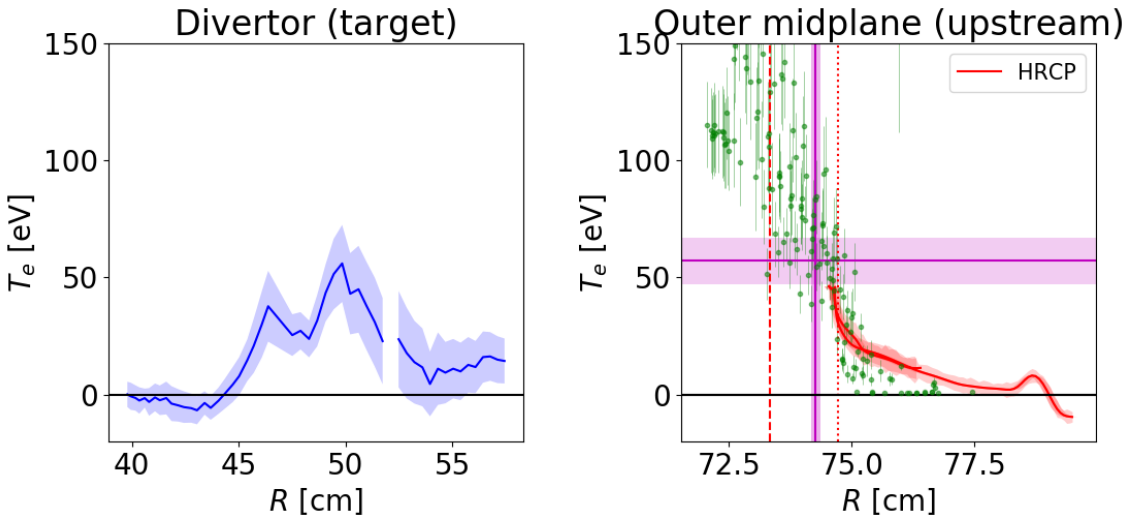


Figure 3.9: Separatrix position (vertical magenta line) inferred from the 2PM $T_u$ (horizontal magenta line) using the Thomson scattering $T_e$ profile. Horizontal magenta span shows the ±10 eV span used for datapoint choice, vertical magenta span signifies the errorbar of the resulting $R_{sep}$. EFIT separatrix dashed, BPP maximum position dotted. Discharge #13926.

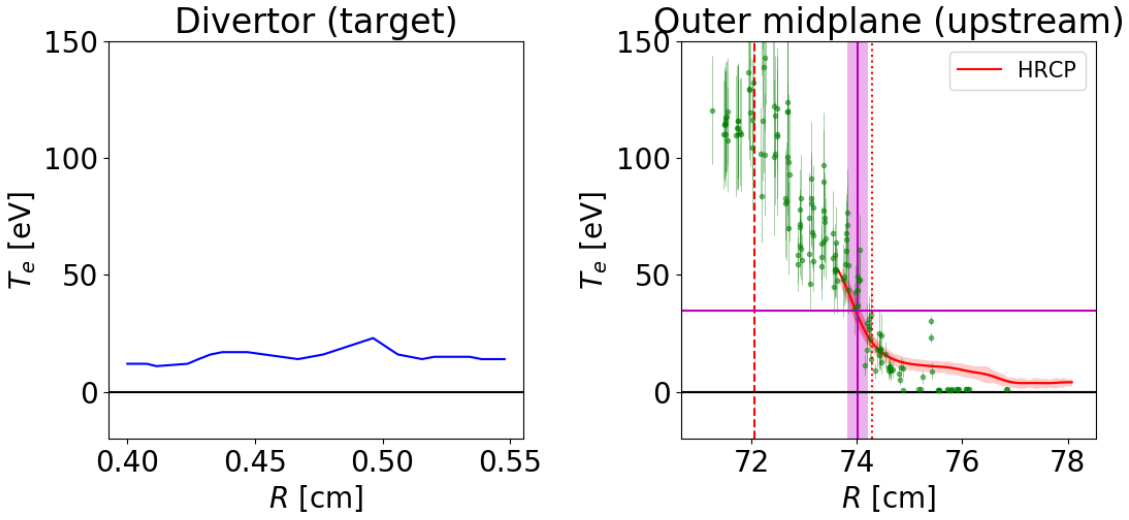


Figure 3.10: Separatrix position (vertical magenta line) inferred from the 2PM $T_u$ (horizontal magenta line) using the HRCP $T_e$ profile. The vertical magenta span signifies errorbar of the resulting $R_{sep}$. EFIT separatrix dashed, BPP maximum position dotted. Discharge #13812.

**Method: Using experimental $T_t$**

In this approach, $T_t$ is taken as the maximum $T_e$ measured on the LFS by one of the divertor probe arrays. As figure 3.8 shows, typically the $T_e$ maximum does not coincide with the EFIT strike point or the $I_{sat}$ maximum. The shift between the peak of $T_e$ and $I_{sat}$ may be explained by an increased temperature drop along field line as the plasma in the vicinity of the separatrix is closer to the high-recycling/conduction-limited regime. This is due to increased collisionality at this region caused by longer $L$ (vicinity of the X-point) and large density (maximum at the LCFS).

To obtain the final goal, the separatrix position, the calculated $T_u$ must be found on the upstream temperature profile. Two diagnostics are suitable for upstream profile measurement on the OMP: the HRCP and the TS, which must first be mapped onto the OMP. The latter case, of course, includes the need to correct the EFIT systematic error. Even if $T_u$ is sought on the original TS axis on the top of the plasma, the resulting $Z_{sep}$ must be mapped onto the OMP anyway in order to be compared with the other separatrix indicators. It does not matter whether the separatrix position is first sought from $T_u$ and then mapped onto the OMP, or vice versa. Thus the latter approach was taken, which implied the need to shift the mapped TS profile on the OMP. The shift was performed so that the TS data were an extension of the HRCP profile. The separatrix position was sought in the following way:

- HRCP measures deep enough to reach $T_u$:
  $T_e = T_u$ is sought on the profile and the mean of the resulting positions (for probe movement in and out) is taken to obtain $R_{sep}$.
- HRCP does not go deep enough but TS data is available:
  TS datapoints with $T_e$ in the span $(T_u - 10\text{ eV}, T_u + 10\text{ eV})$ are chosen from the stationary phase of the discharge, $R_{sep}$ is taken as the mean of their radial positions.

In the case of using the HRCP profile, $R_{sep}$ error was estimated as 2 mm, Sec. 3.1.2. If TS had to be used, the error was calculated as the arithmetic mean error,

$$\Delta R = \frac{1}{N}\sqrt{\sum_{i=1}^{N}\left(R(i) - \overline{R}\right)^2}$$

where $N$ is the number of datapoints contained in the temperature span.

When $T_t$ was taken from the new divertor array, 67 discharges yielded $R_{sep}$ by comparing $T_u$ with the TS profile. Only in one discharge (#13813) did the HRCP perform a reciprocation deep enough to measure $T_u$. An example is plotted in figure 3.9. With $T_t$ taken from the old divertor array, 12 discharges yielded $R_{sep}$ using TS and 11 using the HRCP. This goes to show that the old divertor array measures systematically lower temperatures than the new divertor array. An example of $R_{sep}$ inferred from the HRCP profile in plotted in figure 3.10.

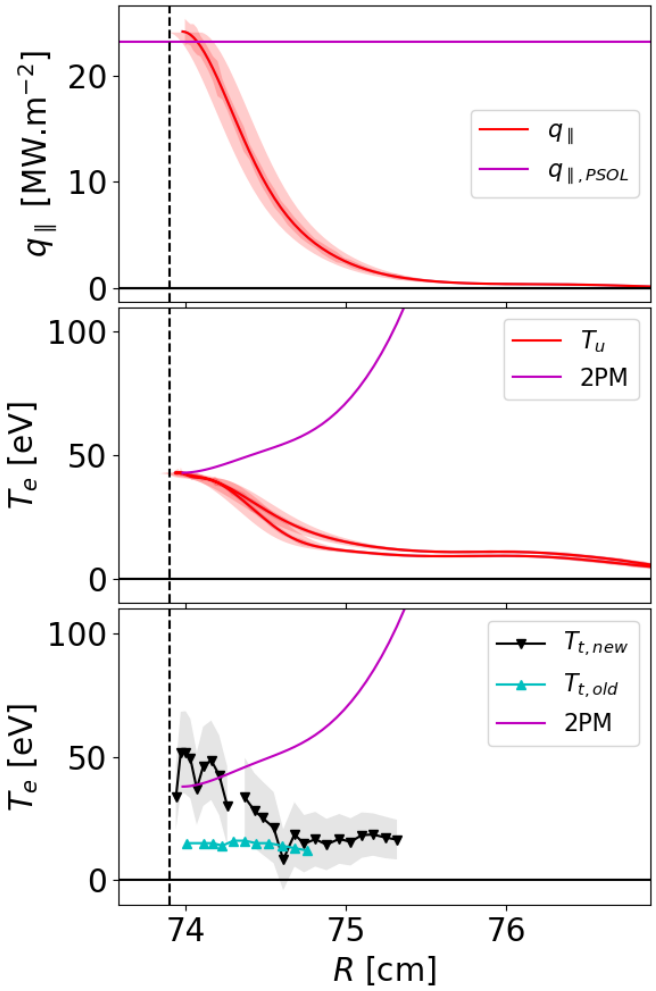


Figure 3.11: Example of applying Eq. (3.4). Upstream experimental data are plotted with a red line, target experimental data with triangles. The magenta line are inputs and outputs of the 2PM: in the uppermost figure it is the $q_\parallel$ inferred using Eq. (3.3) and in the middle and bottom figure it signifies the $T_u(R)$ and $T_t(R)$ curves, respectively. Discharge #13820.

**Method: Sampling the separatrix position with $n_u(R)$**

The alternative approach to finding $T_t$ uses the 2PM, which allows the calculation of $T_t$ from $n_u$, $q_\parallel$, and $L$ with Eq. (1.7). While $q_\parallel$ and $L$ can be approximated as explained above, finding $n_u$ requires knowing the separatrix position, which is what we are trying to calculate in the first place. This is why, instead of $T_{sep}$, the entire "profile"

$$T_u(R) = \left( T_t^{7/2} \left( n_u(R), q_\parallel, L \right) + \frac{7}{2} \frac{q_\parallel L}{\kappa_{0e}} \right)^{2/7} \tag{3.4}$$

is calculated from the experimental $n_u(R)$ profile. The resulting $T_u(R)$ is not an actual physical profile. To put it simply, $T_u(R)$ answers the question: "If $R$ was the separatrix, with the entire $P_{SOL}$ entering at this location, then what value would $T_u$ have here?" By comparing this curve to experimental temperature measurements, either of $T_u$ or $T_t$, the separatrix position may be found.

An example where this method was successful is shown in figure 3.11. In the upper plot, the approximated $q_{\parallel PSOL}$ intersects the experimentally measured profile of $q_\parallel$ at the same radial location as the $T_u(R)$ curve touches the $T_u$ profile. This result was actually typical. Those discharges where a reciprocation deep enough to reach $q_{\parallel PSOL}$ occured were also those where the $T_u(R)$ curve intersected the experimental temperature profile, with the two locations agreeing within 3 mm. It is interesting that this model is self-consistent. It shows that both the assumptions,

- the 2PM can be used to predict $T_u$ from $q_\parallel$ and $n_u$,
- using $P_{SOL}$ and characteristic flux tube dimensions gives an accurate estimate of the separatrix heat flux,

are valid at once. Within the uncertainties presented by smoothing the $T_u$ profile and calculating $q_{\parallel PSOL}$, this way of inferring the separatrix position yields an agreement with the corrected EFIT maximum, which is ultimately chosen as the best separatrix representative in section 3.1.6. However, there are too few datapoints to allow a worthwhile statistical analysis or to consider this method widely applicable.

Two extra examples of using the $T_u(R)$ method are plotted in the appendix, figures C.1 and C.2.

### 3.1.5 Correcting the EFIT OMP mapping error

In total, four ways of correcting the EFIT OMP separatrix position or detecting the separatrix itself were tested: manually overlaying the HRCP and VRCP $T_e$ profiles, detecting the maxima of BPP floating potential, fitting the near and far SOL with a broken exponential to obtain the boundary $R_{break}$ between them, and inferring $T_{sep}$ from $T_t$ using the 2PM. The methods have a varying degree of applicalibility depending on how many input variables are required, and they can be combined in various ways. In this section they will be statistically tested as to their mutual corellation and systematic errors.

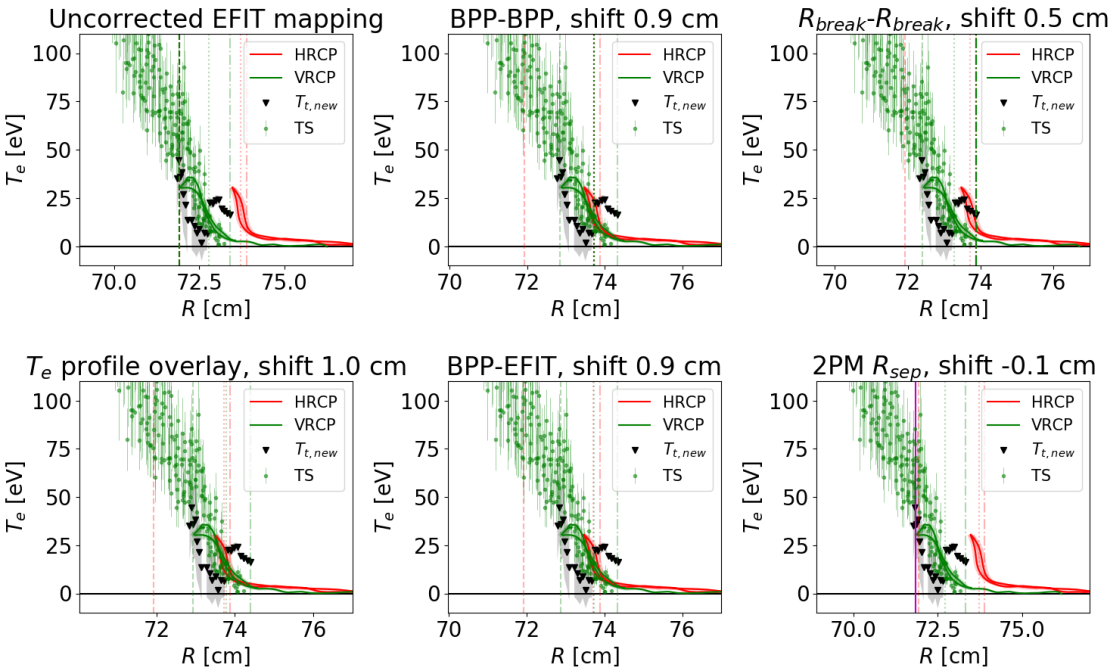


Figure 3.12: An example of corrections to EFIT mapping. The BPP-EFIT shift is already corrected using equation (3.6). Discharge #15491, D-shaped plasma.

There are two distinct applications that I seek by processing the obtained data. Firstly, I wish to be able to correct the mapping error of EFIT in any given discharge. The ideal output of this analysis are instructions on how to perform this correction based on the data available in the particular discharge. Secondly, I wish to know the exact position of the separatrix. This is convenient for a number of reasons, having accurate upstream inputs into the 2PM prominent among them. The data processing will therefore be carried out in a way that will preferentially produce these two outputs.

In the issue of correcting the EFIT OMP mapping, the following shifts $\Delta$ of the mapped axis were investigated, illustrated with figure 3.12:

1. $\Delta_{Te}$ - manual overlay of HRCP and VRCP $T_e$ profiles
2. $\Delta_{BPP,BPP}$ - overlay of BPP maxima detected on the HRCP and on the VRCP
3. $\Delta_{BPP,EFIT}$ - overlay of the HRCP BPP maximum and the EFIT separatrix
4. $\Delta_{2PMnew,EFIT}$ - overlay of the 2PM $R_{sep}$ and the EFIT separatrix, using the new divertor array data
5. $\Delta_{2PMold,EFIT}$ - overlay of the 2PM $R_{sep}$ and the EFIT separatrix, using the old divertor array data[3]
6. $\Delta_{Rbreak,Rbreak}$ - overlay of the $R_{break}$ detected on the HRCP and on the VRCP

Since $\Delta_{Te}$ corresponds to a well justified assumption that $T_e$ at LCFS is constant over flux surface, it is taken as the reference case, to which all the others are compared.

[3]This overlay is not plotted in the figure. There is unfortunately no discharge where the HRCP, the VRCP, and the old divertor array measure at once, so $\Delta_{2PMold,EFIT}$ can only be compared against $\Delta_{BPP,EFIT}$.

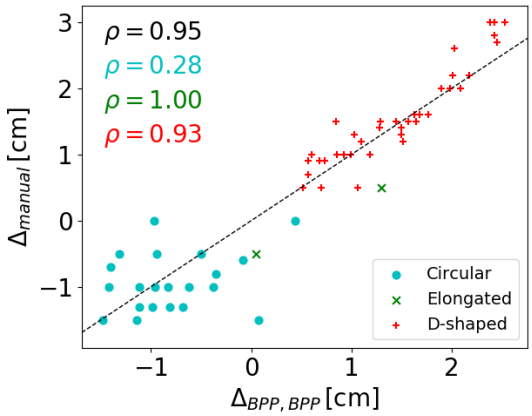


Figure 3.13: Scatterplot comparing the manual overlay of $T_e$ profiles to the overlay of BPP potential maxima. 60 datapoints.

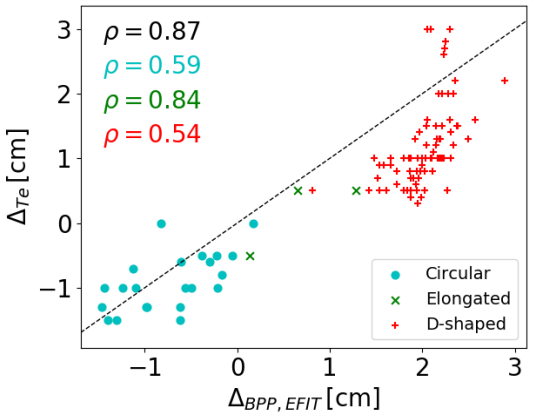


Figure 3.14: Scatterplot comparing the manual overlay of $T_e$ profiles to the overlay of the HRCP BPP potential maximum and the EFIT separatrix. 104 datapoints.

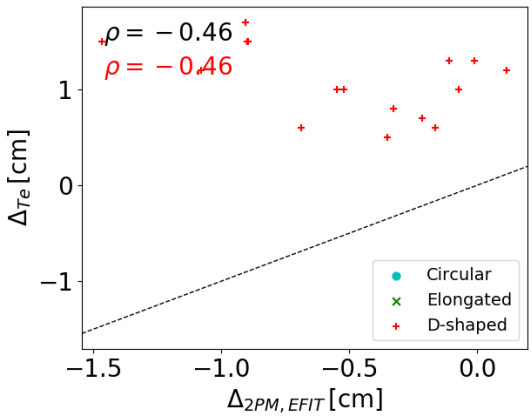


Figure 3.15: Scatterplot comparing the manual overlay of $T_e$ profiles to the overlay of the 2PM separatrix and the EFIT separatrix. 16 datapoints.

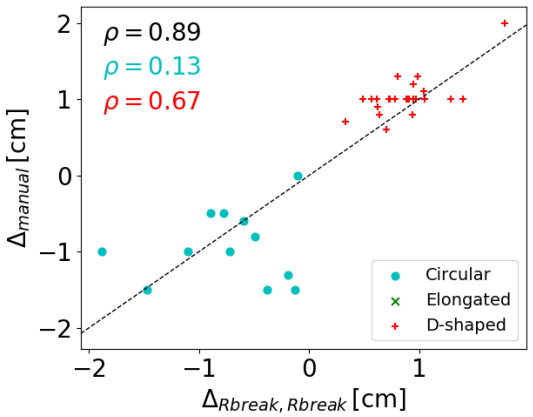


Figure 3.16: Scatterplot comparing the manual overlay of $T_e$ profiles to the overlay of the near-far SOL boundaries $R_{break}$. 37 datapoints.

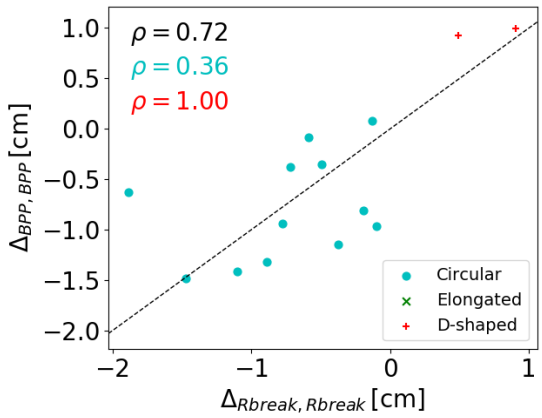


Figure 3.17: Scatterplot comparing the overlay of the near-far SOL boundaries $R_{break}$ to the overlay of BPP potential maxima. 14 datapoints.

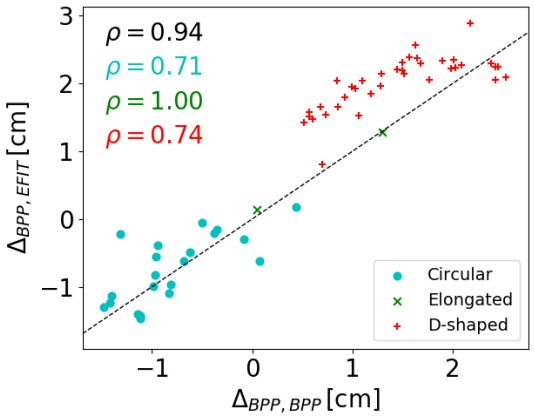


Figure 3.18: Scatterplot comparing the overlay of BPP potential maxima to the overlay of the HRCP BPP potential maximum and the EFIT separatrix. 62 datapoints.

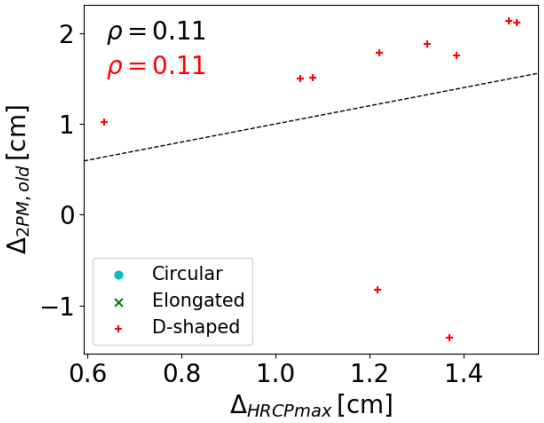


Figure 3.19: Scatterplot comparing the overlay of $R_{sep}$ calculated using the 2PM from the old divertor array data to the overlay of the HRCP BPP potential maximum and the EFIT separatrix, corrected using Eq. (3.6). 10 datapoints.

The results are plotted in figures 3.13-3.18. The dashed black line shows the 1:1 dependency and $\rho$ values in the upper left corner stand for the Pearson correlation coefficient between the shifts, calculated for all available datapoints (black) and for the respective plasma configurations (color). Several observation are immediately obvious.

- $\Delta_{Te}$, $\Delta_{BPP,BPP}$ and $\Delta_{Rbreak,Rbreak}$ are all strongly correlated in a 1:1 dependence, with $\rho \geq 0.72$ and growing with the amount of datapoints up to $\rho = 0.95$.
- The $\Delta_{BPP,EFIT}$ shift, which does not need any VRCP data, is also strongly correlated with $\Delta_{Te}$, but exhibits a systematic departure from the 1:1 dependency, which is especially prominent in D-shaped plasmas. This is most likely caused by the imprecision of the EFIT separatrix position on the top of the plasma, which is taken into account in $\Delta_{Te}$ but not in $\Delta_{BPP,EFIT}$. The way how to adapt $\Delta_{BPP,EFIT}$ to compensate for this missing information will be shown later in this section in Eq. (3.6).
- The 2PM-EFIT overlay using the new divertor array $T_t$ is completely unusable for EFIT mapping correction. While the manual shift is typically around +1 cm, the 2PM-EFIT shift has the mean value of -0.5 cm and is negatively correlated with the manual shift (the $p$-value of the correlation is 2 %).
- The 2PM-EFIT overlay using the old divertor array $T_t$ shows an intriguing correlation with the BPP-EFIT overlay, however, two outliers cause the overall correlation to be very small. These two data points were investigated and no error or significant difference from the other discharges was uncovered, therefore it should be assumed that this seeming correlation is caused by analysing a dataset of insufficient size.

The strong 1:1 correlation of three independent shifts suggests that the electron temperature profiles measured on the HRCP and the VRCP are, indeed, poloidally symmetric and the assumption of the poloidal symmetry holds also for the positions of the VSL and the boundary between near and far SOL. It is possible that if another characteristic place on the RCP profiles was found (such as the beginning of GAMs as observed in [46], the start of exponential decay of sawtooth oscillations amplitude due to fast energy losses along open field lines in the SOL, or the position of the poloidal phase velocity reversal), its position would also be poloidally symmetric. Such a measurement could be used in the same manner as the BPP potential maxima were used here, to correct the EFIT mapping error on the OMP.

The profile shift comparison has yielded intriguingly unanimous results, but there lies a problem within it. This problem is data availability. It is good to know that certain measurements allow an accurate EFIT mapping correction, but if these measurements are not performed routinely then their significance is limited. Not in all discharges does the HRCP move, or move deep enough into the plasma to measure the BPP potential maximum. In even less discharges does the VRCP move as well. If the ultimate goal is to suggest a correction that can be used universally to correct the EFIT OMP mapping, then the data set required for the calculation must be as small as possible.

For instance, the BPP-EFIT shift is available in more discharges than the BPP-BPP

shift, as it only requires that the HRCP measured $V_{BPP}$ deep enough to reach the maximum. The price paid is lesser accuracy - even if the deviation from the 1:1 dependency in figure 3.14 is fixed using a linear fit depending on $\Delta_{BPP,EFIT}$, the scatter is larger than in the BPP-BPP shift.

A whole new challenge then arises when one attempts to correct the EFIT OMP mapping error based on routinely measured plasma parameters. To provide an example: since shifts depend strongly on the plasma shape, the magnetic equilibrium geometry apparently plays an important role in the EFIT systematic error. Therefore, an easily obtained geometry parameter like plasma elongation $\epsilon$ may be a good control variable. In figure 3.20, the dependency of the manual shift on $\epsilon$ is drawn. Evidently elongation is not the best choice for the x axis, as most of the datapoints are concentrated near to $\epsilon = 1$ (circular plasmas) and $\epsilon = 1.8$ (D-shaped plasmas). Performing a linear fit of the dependency, one obtains

$$\Delta_{elongation} = 2.65\epsilon - 3.46.$$

Using this formula to predict the manual shift from elongation, one arrives at figure 3.21. The correlation is quite high, $\rho = 0.77$, but it is obvious that this prediction contains a large random error. An alternative approach which yields approximately the same results, figure 3.22, is to set the shift for circular and D-shaped plasmas firmly as use a fit only for the elongated plasmas,

$$\Delta_{shape} = \begin{cases} (-0.9 \pm 0.4) \text{ cm} & \text{for circular plasmas} \\ (8.34\epsilon - 9.96) \text{ cm} & \text{for elongated plasmas} \\ (1.2 \pm 0.7) \text{ cm} & \text{for D-shaped plasmas.} \end{cases} \tag{3.5}$$

At the moment I have not reached a more reliable formula for correcting the EFIT mapping error without any additional data. However, if the HRCP BPP potential maximum position is available, by improving the BPP-EFIT data with a linear fit one reaches the prediction of figure 3.23,

$$\Delta_{HRCPmax} = 0.77\Delta_{BPP,EFIT} - 0.37 \text{ cm}. \tag{3.6}$$

This correction of the EFIT OMP mapping is available whenever the HRCP performs a deep enough reciprocation, and yields results that show no systematic error unlike the uncorrected BPP-EFIT shift.

To summarise, in this section it was found that the HRCP and VRCP $T_e$ profiles are poloidally symmetrical inside the separatrix and in the near SOL. Overlaying the maxima of the BPP potential and the boundaries between the near and far SOL results in the profiles themselves overlaping. This confirms the assumption of poloidal $T_e$ symmetry based on the high electron thermal diffusivity and offers an accurate way of correcting the systematic error of mapping to the OMP using EFIT. In discharges where this data is not measured, it is possible to estimate the appropriate shift using only the HRCP BPP potential maximum or to infer the shift from the plasma elongation. On average, it was found that in circular plasmas the EFIT mapping is displaced by $(-0.9 \pm 0.4)$ cm and in D-shapes plasmas by $(1.2 \pm 0.7)$ cm.

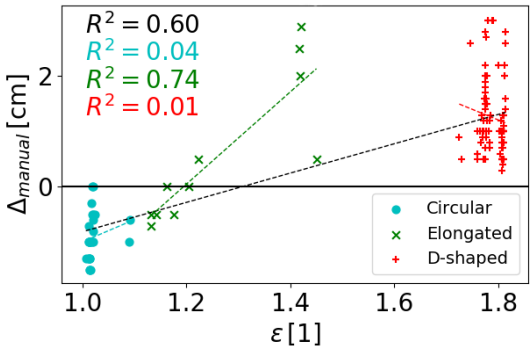


Figure 3.20: Scatterplot of the manual overlay of HRCP and VRCP $T_e$ profiles as dependent on plasma elongation. 135 datapoints.

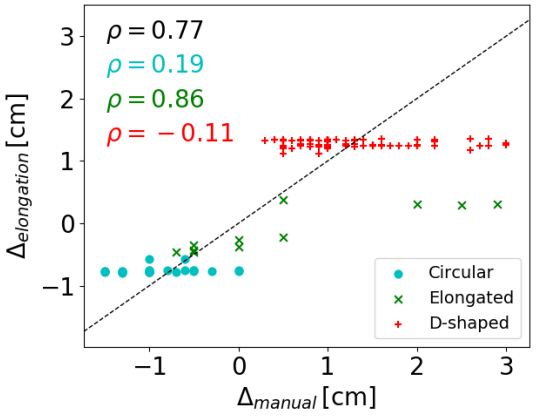


Figure 3.21: Scatterplot comparing the manual overlay to the shift computed from elongation using the formula $\Delta_{elongation} = 2.65\epsilon - 3.46$. 135 datapoints.

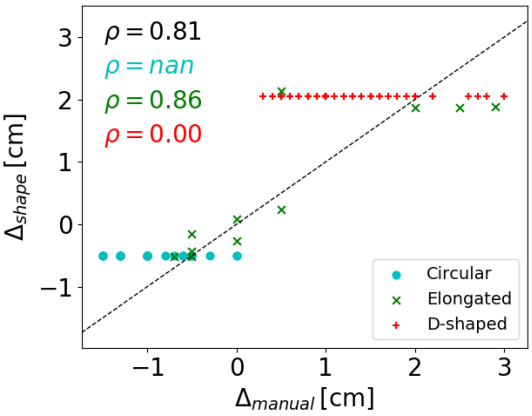


Figure 3.22: Scatterplot comparing the manual overlay to the shift computed from elongation using equation (3.5). 135 datapoints.

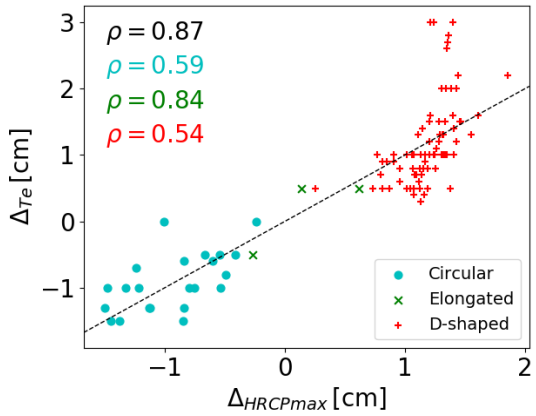


Figure 3.23: Scatterplot comparing the manual overlay to the shift computed from the BPP-EFIT shift using equation (3.6). 104 datapoints.

### 3.1.6 The exact separatrix position

Now that the issue of correcting the EFIT OMP mapping has been properly addressed, the data analysis moves on to investigating the actual separatrix position $R_{sep}$ on the OMP. Five sources are available for comparison:

- $R_{EFIT}$ - EFIT (uncorrected)
- $R_{EFIT,corr}$ - EFIT (corrected by the best available profile shift from the previous section)
- $R_{BPP}$ - BPP potential maximum
- $R_{sep,new}$ - 2PM separatrix calculated using the new divertor array $T_t$ (Sec. 3.1.4)
- $R_{sep,old}$ - 2PM separatrix calculated using the old divertor array $T_t$

Of these, $R_{BPP}$ is taken as the reference case against which all the others are compared, as it is an easily detectable separatrix position indicator which allowed for a precise analysis in the previous section. The boundary between the near and far SOL $R_{break}$ will enter the analysis briefly as well, though not as a candidate for the separatrix position but rather as a limit for it. The alternative "$T_u(R)$" approach to inferring $R_{sep}$ using the 2PM, described in section 3.1.4, yielded only qualitative results and it seems to be in accord with the corrected EFIT.

Figures 3.24-3.27 show the typical correlations between the candidates on separatrix position. Several observations can be made.

- There is a large systematic difference between $R_{BPP}$ and $R_{EFIT}$ depending on plasma shape. In part, this can be attributed to the systematic error of the EFIT separatrix on the OMP. However, after correcting $R_{EFIT}$ to obtain $R_{EFIT,corr}$, figure 3.25, the systematic difference persists for most of the diverted discharges (and for all of those corrected by the BPP-BPP shift). We see that in the limiter configuration the BPP maximum tends to form at the corrected EFIT separatrix, but in the divertor configuration it forms 1 cm radially outside of this position.
- Separatrix positions inferred using the 2PM are positively correlated with $R_{BPP}$, although not as strongly as with $R_{EFIT}$. A constant offset is visible in both cases: 2-3 cm for the new divertor array and 0.5 cm for the old divertor array. This is consistent with the new array measuring higher temperatures, which means that the calculated higher $T_u$ is placed deeper into the edge plasma. The two outliers, visible in figure 3.19, are present also in figure 3.27, distorting the otherwise clean dependency. It is uncertain why the values of these two points are so distant, however, no reason was found to call them erroneous.

After making these observations, I will argue why the EFIT separatrix corrected with the best available shift should be taken as the optimal indicator of the real last closed flux surface. (To repeat, the hierarchy of "best" is 1. BPP-BPP shift, 2. corrected BPP-EFIT shift, 3. shift based on plasma shape or elongation.) First, the correction of $R_{EFIT}$ on the OMP, discussed in the previous section, is quite firmly established with three independent methods, $T_e$ profile overlay, $R_{BPP}$ overlay, and

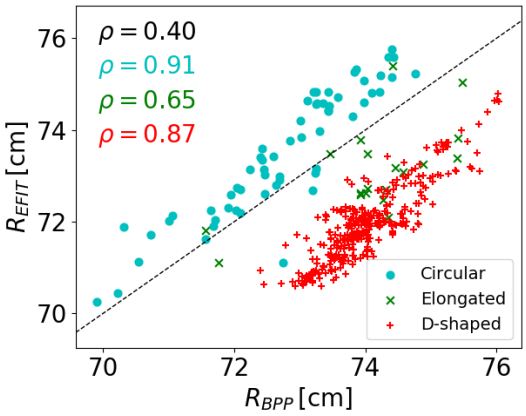


Figure 3.24: Scatterplot of the radial position of BPP potential maximum $R_{BPP}$ vs the uncorrected EFIT separatrix position $R_{EFIT}$. 406 datapoints.

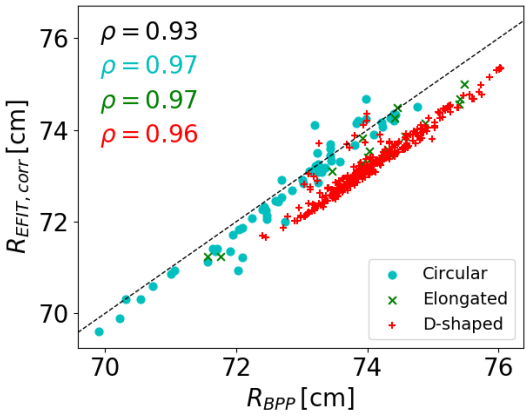


Figure 3.25: Scatterplot of the radial position of BPP potential maximum $R_{BPP}$ vs the corrected EFIT separatrix position $R_{EFIT,corr}$. 406 datapoints.

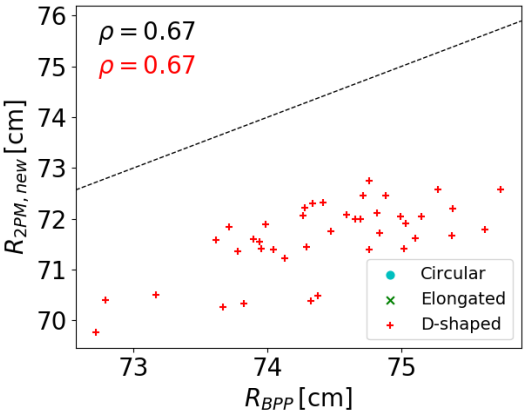


Figure 3.26: Scatterplot of the radial position of BPP potential maximum $R_{BPP}$ vs the $R_{sep}$ inferred using the 2PM from the new divertor array data. 41 datapoints.

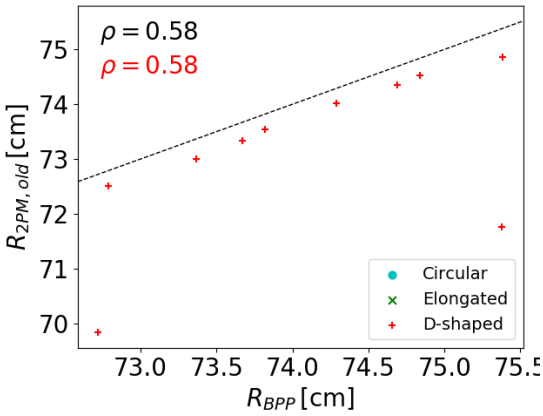


Figure 3.27: Scatterplot of the radial position of BPP potential maximum $R_{BPP}$ vs the $R_{sep}$ inferred using the 2PM from the old divertor array data. 10 datapoints.

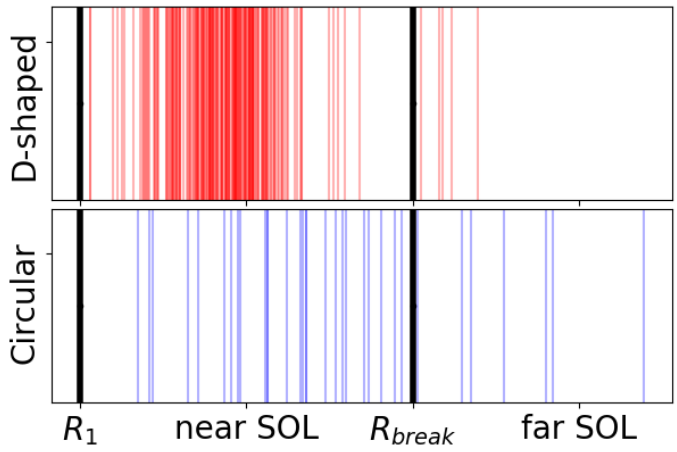


Figure 3.28: Occurence of BPP maximum in the near SOL for circular and D-shaped plasma. $R_1$ is the beginning on the near SOL, $R_{break}$ is its end. The distance between them is normed to 1 and the maximum position is shown relative to them.

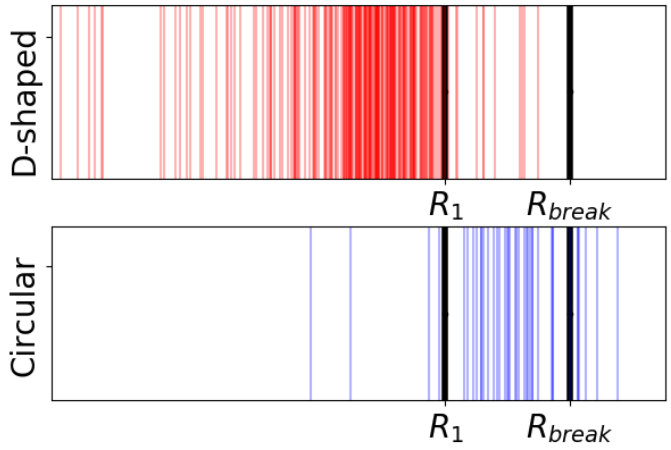


Figure 3.29: Occurence of the corrected EFIT separatrix $R_{EFIT,corr}$ in the near SOL for circular and D-shaped plasma. $R_1$ is the beginning on the near SOL, $R_{break}$ is its end. The distance between them is normed to 1 and the separatrix position is shown relative to them.

$R_{break}$ overlay, supporting it by their strong 1:1 correlation. Furthermore, in the next section, using $R_{EFIT,corr}$ as the real separatrix will lead to a self-consistent two-point model of the COMPASS SOL. Lastly, both of the 2PM separatrix candidates are alsp correlated with $R_{EFIT,corr}$, albeit not as strongly as $R_{BPP}$ ($\rho = 0.93$ for circular plasmas). As to their use as a separatrix position indicator, the scatter is too large to be more useful than the HRCP techniques, which are also more easily accessible throughout the COMPASS database.

An interesting insight is provided in figure 3.28, where the near SOL is normed to the extent (0,1) and plotted together with the BPP maxima. The inner edge of the near SOL, $R_1$, was taken as the inner boundary of the double exponential $T_e$ profile fits described in section 3.1.3, and its outer edge was set to $R_{break}$. In the majority of cases, the BPP potential maximum forms in the near SOL in both circular and D-shaped plasmas. In contrast, when the corrected EFIT separatrix position is plot-

ted relative to the near SOL, figure 3.29, the situation changes between the divertor and limiter configuration, in accord with figure 3.25. In the divertor configuration, $R_{EFIT,corr}$ typically lies just inside the near SOL. In the limiter configuration, on the other hand, the separatrix forms inside the near SOL atop the BPP maximum. I have no physical explanation why this should be so, but the experimental correlation is too strong not to consider it supported by some physical mechanism. For instance, the shearing flows at the plasma edge may have a different profile for the two configurations, or the magnetic shear near the X-point may play a role.

Concluding from the observations made above, in the following analysis the corrected EFIT separatrix $R_{EFIT,corr}$ will be used as "the real separatrix". The 2PM candidates are not as widely applicable and feature a greater scatter, while the BPP maximum does not coincide with the separatrix in the divertor configuration. $R_{BPP}$ can, however, be used as a precise separatrix position indicator in plasmas with a circular cross-section.

Unless stated otherwise, from now on $R_{EFIT,corr}$ will be denoted in radial profiles with a black dashed line.

Now that both the questions of OMP separatrix position and EFIT mapping correction have been addressed, we can move on to the core of this thesis: the SOL transport regime of tokamak COMPASS.

## 3.2 SOL transport regime of tokamak COMPASS

### 3.2.1 Collisionality achievable in the COMPASS parameter space

The basic and easiest step toward determining the SOL transport regime of tokamak COMPASS is to reproduce figure 1.2 using experimental data. Since the axes of this plot feature quantities taken at the separatrix, the newly established $R_{EFIT,corr}$ can be used right away, figure 3.30. Of the 369 discharges where $q_{\parallel}$ and $n_e$ were measured by the HRCP, only a third is plotted here because the probe does not typically reciprocate this deeply into the plasma. (For good reasons. Effects such as self-emission or arcing, whose onset is often associated with the steep heat flux gradient in the separatrix vicinity, not only devalue $q_{\parallel}$ and $n_e$ measurements, but can also negatively affect the probe, for instance by eroding the graphite pins of the Langmuir probes.) To obtain a wider data set, the same plot was drawn using the BPP potential maxima as separatrix, figure 3.31.

In the appendix C.7, thus obtained collisionalities are plotted against each other, showing a positive correlation but with a dauntingly large scatter. For instance, in discharge #6024 ($I_p$ = 160 kA, $\overline{n}_e = 5 \times 10^{19}$ m$^{-3}$, D-shaped) $\nu^*_{BPP} = 24$ while $\nu^*_{EFIT,corr} = 5$. In this particular discharge, $R_{BPP}$ and $R_{EFIT,corr}$ lie 1 cm apart, which is enough to raise the heat flux by a factor of 10, figure C.8. Consequently, the "outlier" is entirely legitimate and it shows the difference in collisionalities between two SOL flux tubes which lie far apart. In fact, most of the scatter in the $\nu^*_{BPP} -$

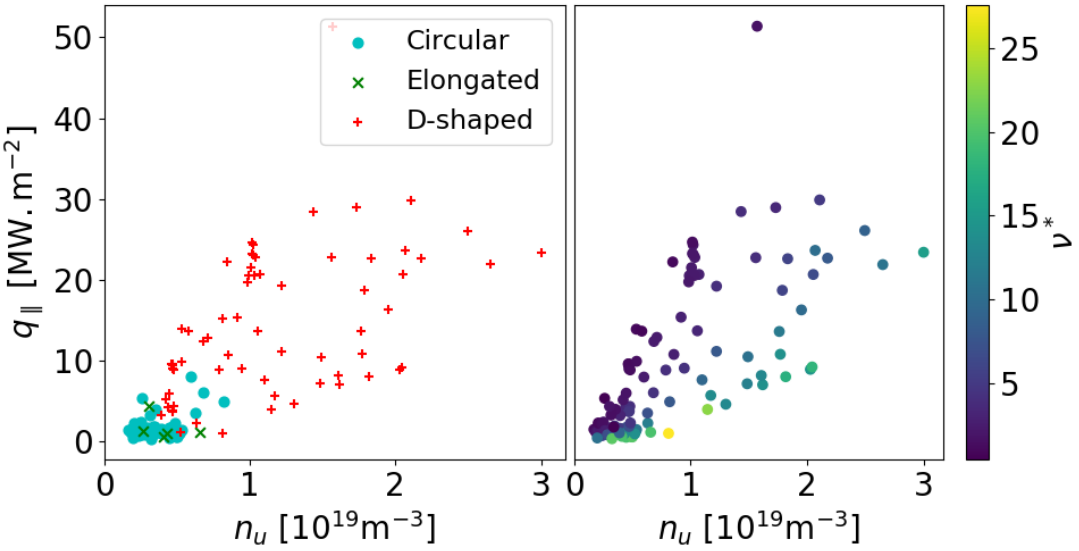


Figure 3.30: The COMPASS operational space, with $q_\parallel$ and $n_u$ taken at the corrected EFIT separatrix. Outer target. 109 datapoints.

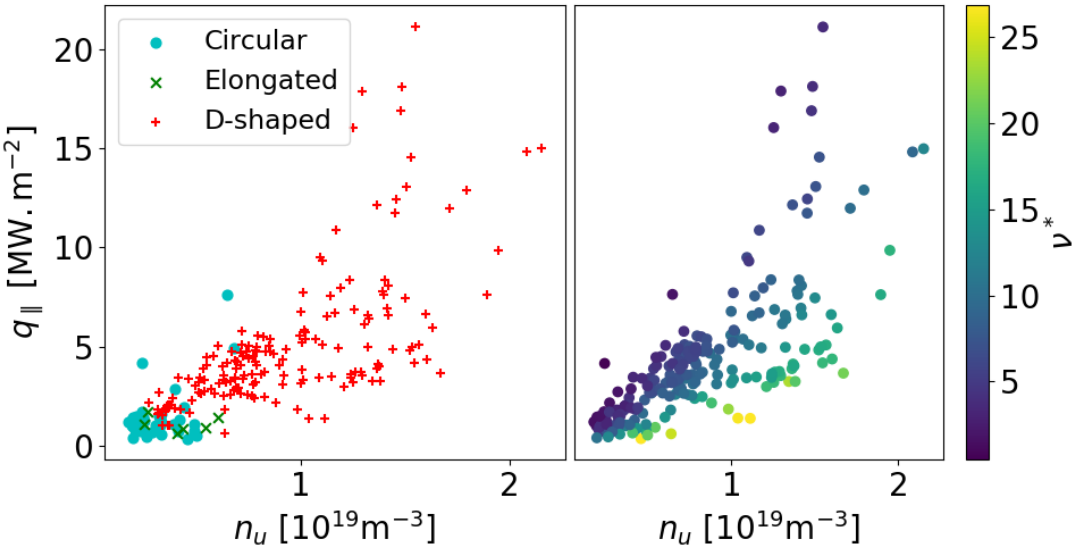


Figure 3.31: The COMPASS operational space, with $q_\parallel$ and $n_u$ taken at the BPP maximum. Outer target. 224 datapoints.

$\nu^*_{EFIT,corr}$ plot may be caused by the fact that the collisionalities are calculated in different flux tubes. The combination of figures 3.30 and 3.31 may then be taken to indicate that on tokamak COMPASS SOL collisionality does not exceed 30 in any given flux tube. This still provides plenty of space for collisionalities sufficiently high to establish the conduction-limited regime on the outer target.

At the inner target, figures C.3-C.6, collisionalities reach up to 40 due to the longer connection length $L$. Unfortunately, this prediction cannot be validated against experimental data as the new divertor array does not operate well in this part of the divertor. Perhaps in the future, when the large LFS-HFS asymmetry of its measurements has been resolved, the analysis presented in this thesis can be carried out for the inner target as well.

Finally, by calculating the flat-top plasma current $I_p$ and line-averaged density $\overline{n}_e$, it is possible to translate the axes of figures 3.30 and 3.31 into the input parameters of tokamak operation. As figures 3.32 and 3.33 show, however, the result is far from conclusive. Discharges with high collisionality seem to be scattered throughout the parameter space, especially in the case of taking separatrix parameters at the BPP maximum. This may be a sign that the assumption made when choosing 2PM control variables is not completely valid. The heating power and the line-averaged density are, of course, tied to the SOL heat flux and the upstream density, but the relationship between these variables is complex and other factors come into play as well. To provide an example, the scatterplot of $\overline{n}_e$ and $n_{BPP,max}$ was drawn in figure C.9. While the quantities are positively correlated across the bulk of discharges, the dependence is not clean, with many (verified) outliers and datapoint accumulations which show no trend of their own.

### 3.2.2 $T_e$ profiles in discharges with low and high collisionality

As already alluded, it is possible to take the experimental profile of $n_u$, $q_\parallel$, and $L$ and apply the 2PM individually for each flux tube, obtaining predictions for $T_u$, $T_t$, and $n_t$. In this section the upstream and target temperature profiles will be compared, model to experiment.

In figure 3.34, the 2PM predictions of upstream and target temperature are plotted together with the measured profiles and control variables for discharge #13812, which was chosen as a representative of the sheath-limited regime with separatrix collisionality $\nu^* = 4$. The mapping of the divertor profiles was adjusted using the corrected BPP-EFIT shift, Eq. (3.6), similarly to the profile of connection length. The resulting temperature profiles show an extraordinary agreement with the experiment. Though the difference grows in the far SOL, the 2PM predicts the $T_u$ profile within an accuracy of 10 %. The target profile, as measured by the new divertor array, is also perfectly reproduced. The old divertor array, on the other hand, measures temperatures significantly lower. This difference will be addressed below, after the introduction of the conduction-limited regime representative.

Comparing the upstream and target profiles against each other, figure 3.35, one comes to appreciate the importance of accurate mapping. When the small clearance

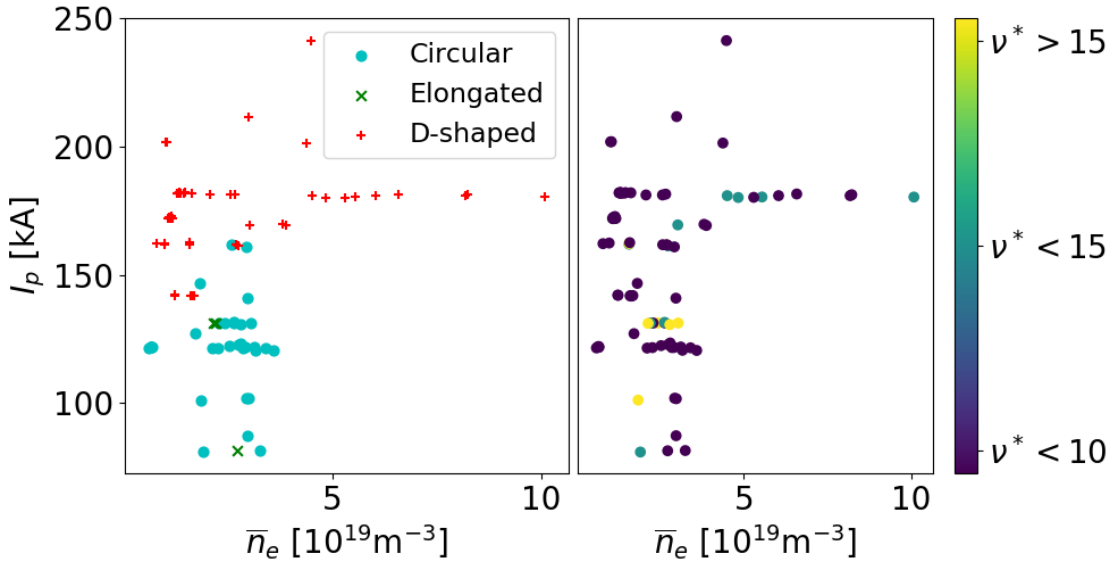


Figure 3.32: The COMPASS operational space, with $I_p$ and $\overline{n}_e$ averaged over the flat top, and collisionality computed at the corrected EFIT separatrix. Outer target. 90 datapoints.

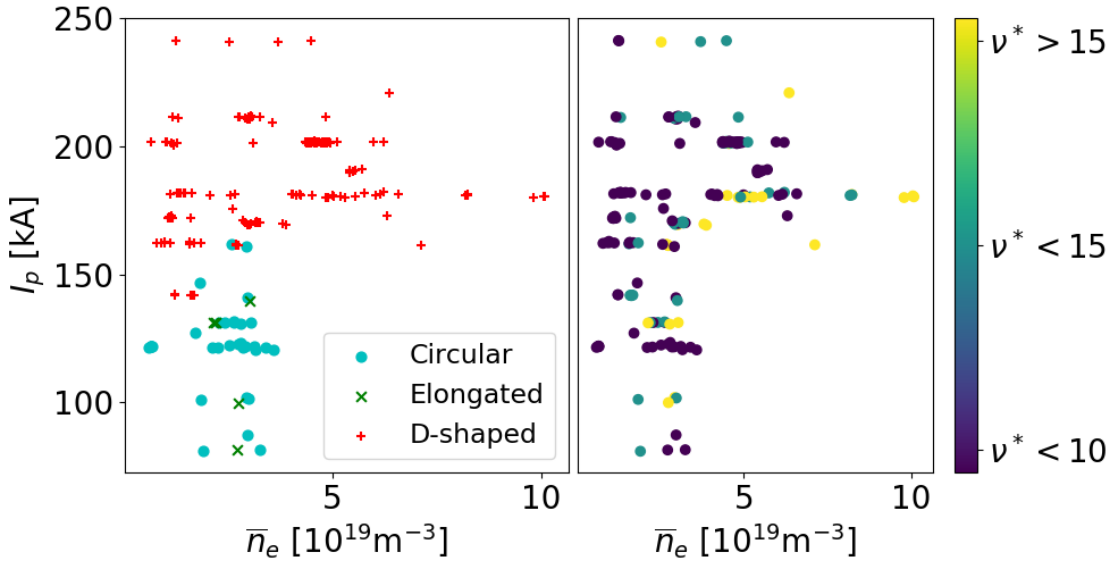


Figure 3.33: The COMPASS operational space, with $I_p$ and $\overline{n}_e$ averaged over the flat top, and collisionality computed at the BPP potential maximum. Outer target. 197 datapoints.

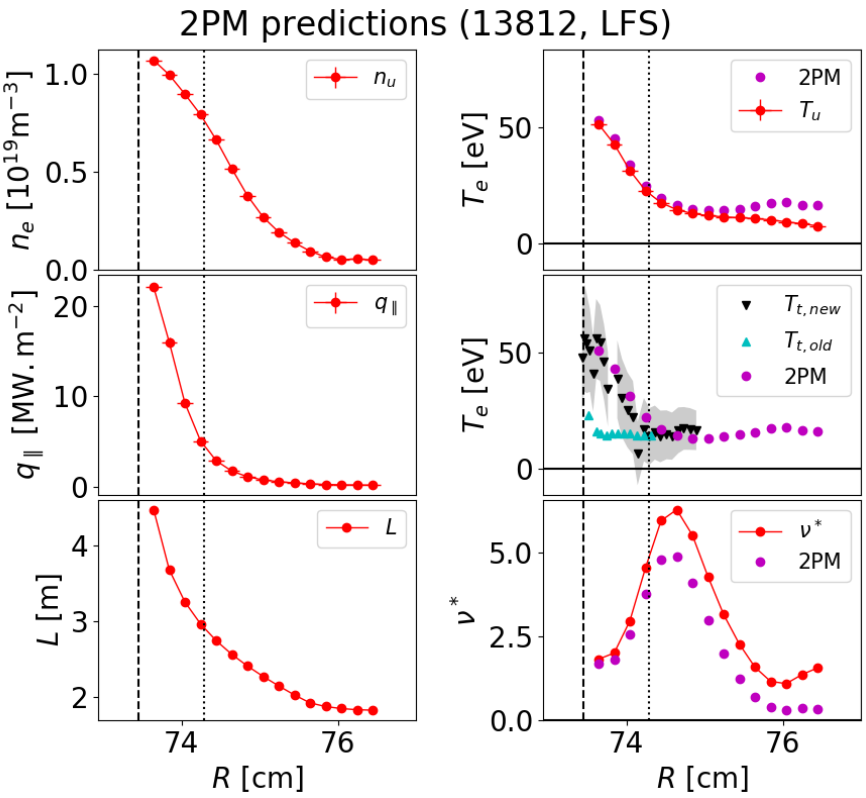


Figure 3.34: Experimental profiles of $n_u$, $q_\parallel$, $L$, $T_u$, $T_t$, and $\nu^*$ (red), compared with the 2PM prediction of $T_u$, $T_t$, and $\nu^*$ (magenta). Discharge #13812. $I_p = 180$ kA, $\overline{n}_e = 3 \times 10^{19}$ m $^{-3}$, $B_T = 1.15$ T.

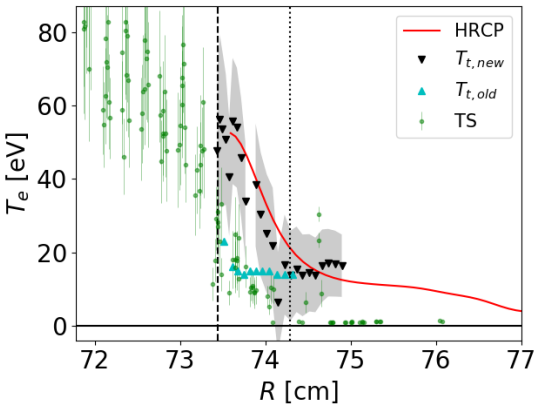


Figure 3.35: $T_e$ profiles measured by the HRCP, the Thomson scattering diagnostic, and the old and the new divertor array. Discharge #13812. Dashed line $R_{EFIT,corr}$, dotted $R_{BPP}$.

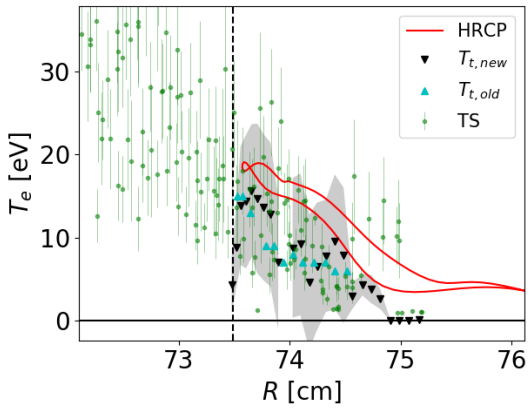


Figure 3.36: $T_e$ profiles measured by the HRCP, the Thomson scattering diagnostic, and the old and the new divertor array. Discharge #15941. Dashed line $R_{EFIT,corr}$.

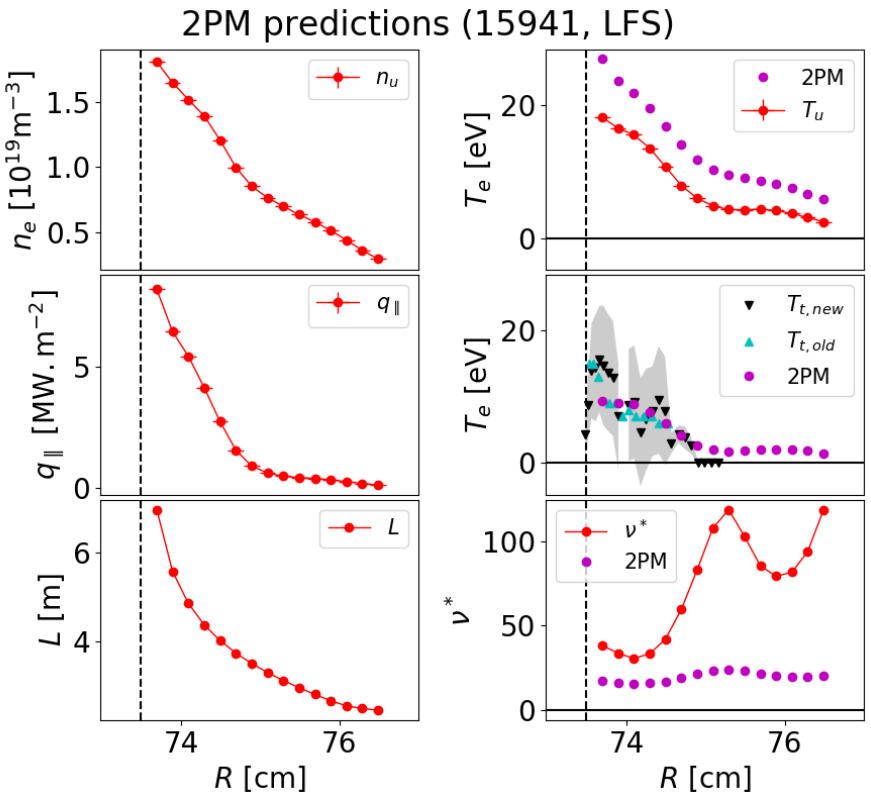


Figure 3.37: Experimental profiles of $n_u$, $q_\parallel$, $L$, $T_u$, $T_t$, and $\nu^*$ (red), compared with the 2PM prediction of $T_u$, $T_t$, and $\nu^*$ (magenta). Discharge #15941. $I_p = 160$ kA, $\overline{n}_e = 8 \times 10^{19}$ m $^{-3}$, $B_T = 1.38$ T.

discussed in section 3.1.1 is considered responsible for the fall of TS temperature to zero where OMP and divertor profiles are still 10-20 eV, then the radial shift of approximately 7 mm between the profiles becomes apparent. Even though the best available mapping correction was employed, the TS, HRCP, and new divertor array profiles, which otherwise have a similar shape, do not overlap. This extra shift in the TS profile is common even when compared to the VRCP, which this diagnostic shares measuring space with. An example of such a shift is given in the appendix, figure C.10. As a result it is not possible to say whether the SOL is truly isothermal on all poloidal angles. The agreement is within the expected bounds and there is no clear indicator of temperature drop toward the divertor.

Because of the large gradients in the vicinity of separatrix, a shift of several milimeters can induce temperature drops by a factor of two just as easily as $T_t > T_u$. Such a precision could conceivably be reached when a precise mapping correction, such as the BPP-BPP or $R_{break}$-$R_{break}$ shift is available. However, when inferring mapping correction from the plasma shape only, the expected scatter is almost 0.7 cm for the divertor configuration. This is enough to render any profile comparison completely worthless and highlights the importance of knowing the exact separatrix position on the OMP, where the systematic errors of magnetic equilibrium reconstruction codes tend to be the largest.

Having discussed a discharge in the sheath-limited regime, let us consider discharge

#15941, where $\nu^*_{EFIT,corr} = 18$. This discharge features lower $I_p$, much higher $\overline{n}_e$, and higher $B_T$. Examining the 2PM $T_e$ profile predictions, figure 3.37, one sees that both upstream and target temperature are much lower than in the previously discussed discharge, about by a factor of two. This time the 2PM predictions are not as spot on: $T_u$ is overstimated, while strike point temperature is lower than what the new divertor array measures. On the other hand, the agreement with the old divertor array is considerably. It is interesting to note that in the sheath-limited discharge, the first derivate probe technique yielded a bimaxwellian electron energy distribution across the entire SOL, while in the conduction-limited discharge the distribution was bimaxwellian only in the vicinity of the strike point. This is in accord with the increased collisionality, which tends to maxwellise the energy distribution of both ions and electrons.

However, the telltale sign of the increased collisionality, a large temperature drop, is not as great as this collisionality would predict. In figure 3.36, all the available temperature profiles are plotted against each other, showing that, like in the previous discharge, the shape of the profiles is quite similar and by shifting some of them radially, complete agreement could be induced. The temperature at the separatrix is approximately 15 eV according to both the divertor arrays, while the HRCP measures a temperature only slightly larger, approximately 20 eV.

Supposing that the mapping correction is at least moderately accurate then, an explanation should be sought for the missing temperature gradient. In the next section upstream and target pressures and heat fluxes will be compared in order to quantify the pressure and power balance between upstream and target. Before that, however, I would like to address the difference between the new and the old divertor array.

In the previous section, dealing with the OMP separatrix position, it was found that the outer strike point temperature of both arrays may be used to predict the separatrix position. The accuracy of this prediction is, however, not great, showing both a systematic shift from other separatrix indicators and a scatter which is not acceptable when accuracy to 1-3 mm is desired. The fact that the new divertor array measures higher temperatures than the new divertor array was confirmed when the $R_{sep,new}$ results were systematically deeper in the plasma than the $R_{sep,old}$ results. This discrepancy may, after all, be seen in figure 3.34. Even though in the sheath-limited regime the higher temperature from the bimaxwellian was taken from the old divertor array, this value is still more than a factor of two smaller than the strike point temperature measured by the new divertor array or predicted by the 2PM. It is not certain how to interpret this difference. The first-derivative probe technique is not widely used like, for instance, the three- or four-parameter fits of the Langmuir probe $I$-$V$ characteristic, so it lacks a strong experimental base. On the other hand, the qualitative results of bimaxwellian/maxwellian electron energy distribution are unique to this method and in accord with theory in this analysis. All in all, it would be unwise to carry out judgements such as "the new divertor array is correct because it is in agreement with the 2PM". A more appropriate course of action would be to carry out experiments where plasma collisionality is as large as possible, and compare the measurements of the two arrays, seeking to reproduce

the agreement of discharge #15941. If this is reached, it may then be discussed why increased collisionality would have this effect on the probe measurements. For instance, collisionality may influence the currents described in Sec. 2.1.1.

### 3.2.3 Power and pressure balance

The 2PM was found in the previous section to be able to predict COMPASS upstream and target temperature profiles quite well in the sheath-limited regime, but in the conduction-limited discharge the predicted temperature drop did not appear in the experimental data. This can indicate that some of the 2PM assumptions of the 2PM do not hold in the COMPASS experiment. Using the HRCP and divertor array data it is possible to verify this hypothesis. The same two discharges representing the sheath-limited and the nearly-conduction-limited regime as in the previous section will be used to demonstrate this.

In figures 3.38 and 3.39 the comparison of upstream and target pressure and heat flux is plotted. Generally the agreement of upstream and target profiles is good, hinting that power and pressure balance both hold in the COMPASS SOL. Strangely, in both the high and the low collisionality discharges, $p_t > p_u$. There is a number of interpretations that can be brought forth here.

- The new divertor array may be overestimating target temperatures. Since $p \sim I_{sat}\sqrt{T_e}$ and $q_\parallel \sim I_{sat}T_e$, such an overestimation would raise both $p_t$ and $q_\parallel t$.
- The effective collecting probe area is different from the used $A_{HRCP} = 4.9$ mm$^2$ and $A_{div} = 2.8$ mm$^2$. Since both $p$ and $q_\parallel$ are inversely proportional to the probe area, such an inaccuracy is capable of scaling the profiles up and down multiplicatively.
- The mapping, while seeming accurate enough, can still be flawed and radial shifts in the profiles may be obstructing their comparison.
- Moving on from the probe dimension of the problem, it is possible that the pressure is, in fact, higher at the target than at the OMP. This could be explained by the power crossing the separatrix from the OMP until the X-point, which can cause a further pressure increase along the flux tube until the maximum is reached near the X-point. This additional energy then propagates radially into the far SOL, causing pressure to grow there as well.

All in all, there are quite a few possible explanations why $p_t > p_u$ could be measured on tokamak COMPASS. Looking past the exact quantitative agreement, however, it is evident that there are no significant power or momentum losses in the COMPASS tokamak. Even in the discharge with a high collisionality the power and pressure balance holds, verifying these two assumptions of the 2PM and raising the question: What has gone wrong? Where is the promised temperature gradient?

There is one more assumption in the 2PM, expressed in its second equation: the heat flux is purely conductive. In discharge #15941 the 2PM predicts high upstream temperatures because with the average temperature this low ($T_{sep} = 20$ eV), heat conduction is not strong enough to carry the measured heat flux in an isothermal

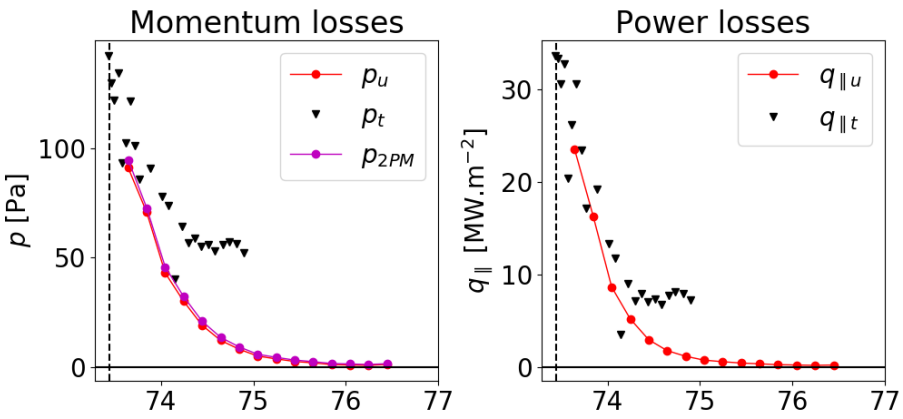


Figure 3.38: Profile of $p_u$, $p_t$, $q_{\parallel u}$, and $q_{\parallel t}$ as measured by the HRCP and the new divertor array. Discharge #13812, collisionality $\nu^*$ =1-5 throughout the SOL.

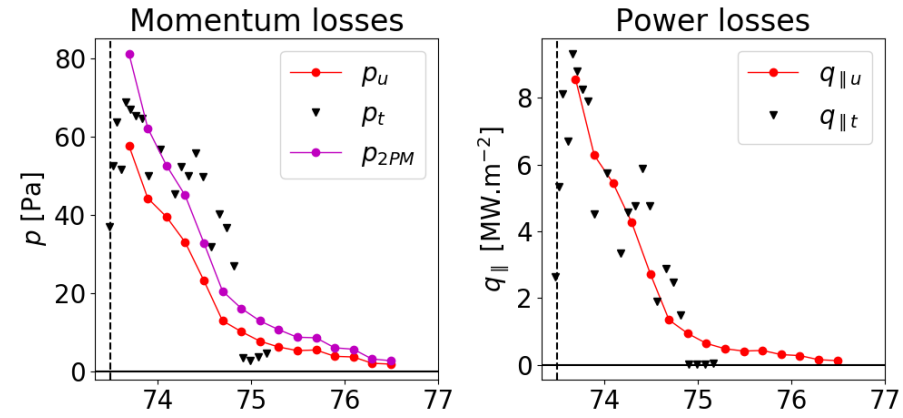


Figure 3.39: Profile of $p_u$, $p_t$, $q_{\parallel u}$, and $q_{\parallel t}$ as measured by the HRCP and the new divertor array. Discharge #15941, collisionality $\nu^*$=10.30 throughout the SOL.

SOL. However, if the experimental heat flux also has a significant convective component, then there needs to be no temperature gradient to drive the power transport.

Across the 61 discharges processed in the 2PM profile analysis described in the previous section, there was none which featured very significant difference between target and upstream temperature, even though according to the 2PM the collisionalities should be sufficient for a temperature drop to appear. This SOL isothermality may be, in part, caused by inaccuracy in the EFIT mapping, which can obscure temperature gradients when they are present. But there is also the possibility that the SOL of tokamak COMPASS has difficulties with supporting large temperature gradients due its short parallel length. Previous experiments studying detachment have yielded similar results, as attempts to induce detachment with nitrogen seeding either had little effect or cooled the SOL as a whole [47]. It seems that this thesis has confirmed this result, minus the nitrogen. The COMPASS SOL is isothermal across a range of discharges with various collisionalities, of course, within the bounds of experimental error where especially radial shifts in mapped profiles play a key role.

# Conclusion

This thesis addressed the question of tokamak COMPASS SOL parallel transport regime by comparing electron temperature profiles within the frame of the two-point model.

In the first chapter, the theory of the two-point model was derived from the basic assumption, that is, the flux tube is a closed system in steady state, with power entering only at the upstream end and leaving only at the target. From this basic principle, power balance, pressure balance, and purely conductive transport follow. The basic 2PM equations were written down and solved in regard to the dependent variables, $T_t$, $T_u$, and $n_t$.

Using the basic 2PM equations,

$$n_u T_u = 2 n_t T_t$$

$$T_u^{7/2} = T_t^{7/2} + \frac{7}{2} \frac{q_\parallel L}{\kappa_{0e}}$$

$$q_\parallel = \gamma e n_t T_t c_{s,t},$$

it is possible to define the regime with a small temperature drop $T_u/T_t < 1.5$ and the regime with a significant temperature drop $T_u/T_t > 3$ as the sheath-limited and the conduction-limited regime, respectively. These temperature drops can be translated into an easily calculate parameter, SOL collisionality

$$\nu^* = \frac{n_u L}{T_u^2} \times 10^{-16},$$

which has the meaning of the amount of collisions a particle undergoes on average before reaching target from upstream. In the sheath-limited regime, $\nu^* < 10$, and for the conduction-limited regime $\nu^* > 15$, the area between them being a transition.

Subsequently the 2PM was applied to the COMPASS parameter space, and it was found that the sheath-limited regime, defined by small temperature gradients from upstream to target, was more native to the outer target of the machine. That does not mean, however, that this tokamak is predicted to be able to operate only in the sheath-limited regime. For the outer target, where connection length is typically $L \approx 5$ m, a sufficiently high upstream density $n_u > 1 \times 20^{19}$ m$^{-3}$ together with low heat flux $q_\parallel < 10$ MW.m$^{-2}$ will induce the conduction-limited regime according to the 2PM. For the inner target, $L \approx 15$ m, the window is larger: the conduction-limited regime and its substantial temperature drop is achieved for $n_u > 1 \times 10^{19}$ m$^{-3}$ and $q_\parallel < 15$ MW.m$^{-2}$.

In the second chapter of this thesis, the five $T_e$ diagnostics of tokamak COMPASS were introduced: the horizontal and vertical reciprocating probe, the old and new divertor array, and the Thomson scattering diagnostic. Probe measurements were discussed in particular, as there is a systematic difference between the old and new divertor array $T_e$ and this was addressed later in the thesis. Toroidally asymmetrix, non-ambipolar currents were suggested as a possible reason for the commonly observed "teeth" on the $T_e$ and $V_{fl}$ profile of the new divertor array, and results similar to those published at the old COMPASS installation site were found.

The third chapter, experimental results, was split into two parts. The first one dealt with the issue of separatrix position on the OMP while the latter discussed SOL transport regimes of tokamak COMPASS.

In the first half of the experimental results, it was shown that the magnetic equilibrium reconstruction code EFIT++ has a systematic error in the separatrix position estimation which depends strongly on plasma shape. Several possible corrections were introduced, including shifting the mapped axis so that the HRCP and VRCP $T_e$ profiles overlapped, overlaying the maxima of ball-pen probe potential which in theory form on the separatrix, overlaying the HRCP and VRCP boundaries between the near and far SOL obtained by fitting the $T_e$ profile with a broken exponential, and overlaying the OMP EFIT separatrix with the BPP potential maximum on the HRCP. Additionally, the 2PM was used to calculate the separatrix temperature from the strike point temperature and the power entering the SOL. When this $T_{sep}$ was found on the OMP temperature profile, this was taken as the separatrix position. Because the new divertor array temperatures were quite high, the HRCP profile had to be extended using the Thomson scattering data.

Comparing the various shifts against each other using the Pearson correlation coefficient and scatterplots, it was found that the $T_e$ profile overlay, the BPP-BPP shift, and the $R_{break}$-$R_{break}$ shift all yield the same results, displaying a strong 1:1 correlation against each other. Thus it was concluded that temperature profiles in the edge plasma of tokamak COMPASS are, indeed poloidally symmetric, and the BPP-BPP shift, which has the widest applicability of the three interconnected mapping corrections, was proclaimed to be the best available EFIT correction on the OMP. As a close second came the BPP-EFIT shift, which involved taking the difference between the HRCP BPP potential maximum position and the EFIT separatrix position $\Delta_{BPP,EFIT}$, and scaling it linearly

$$\Delta = 0.77\Delta_{BPP,EFIT} + 0.33 \text{ cm}$$

to obtain an EFIT mapping correction which also featured a 1:1 correlation with the three mentioned shifts. Finally, for the case where the HRCP did not move deep enough into the plasma to reach the BPP potential maxima, and for the discharges where the HRCP did not move at all, a correction of EFIT OMP mappping was suggested,

$$\Delta_{shape} = \begin{cases} (-0.9 \pm 0.4) \text{ cm} & \text{for circular plasmas} \\ (8.34\epsilon - 9.96) \text{ cm} & \text{for elongated plasmas} \\ (1.2 \pm 0.7) \text{ cm} & \text{for D-shaped plasmas.} \end{cases}$$

based only on the plasma shape or elongation. This correction contains a rather large random error, but it available in any given discharge and its error is not as large as to render it useless.

With the fresh knowledge how to correct the systematic error EFIT exhibits on the OMP, the question of the exact OMP separatrix position was addressed. After comparing the BPP maximum, the corrected and uncorrected EFIT OMP separatrix position, and the $R_{sep}$ inferred from the old and new divertor array, it was concluded that the best measure of the real separatrix is simply the EFIT separatrix corrected for the code's systematic error. It was also found that the BPP potential maximum forms in the near SOL in both the divertor and limiter configuration, and that in D-shaped plasmas the real separatrix lies approximately 1 cm deeper in the edge plasma, while in circulars plasmas the separatrix and the BPP potential maximum coincide.

With the issue of separatrix position solved, the analysis could finally move on to the comparison of $T_e$ profiles measured at various locations and inferring the tokamak COMPASS SOL transport regime. Using the newly derived separatrix position as input for calculating the SOL collisionality, it was found that in some discharges $\nu^*$ can be as high as 25.

Two representative discharges were then picked, #13812 for the sheath-limited regime and #15941 for the conduction-limited regime. In the former discharge, the 2PM provided perfectly accurate predictions of upstream and target temperature profiles, based on the input of OMP $q_{\parallel}$, $n_u$, and $L$ profiles. As one would expect from the sheath-limited regime, there was no temperature drop between upstream and target. In constrast to this harmony, in the high-density discharge #15941 the upstream temperature was measured lower than the 2PM predicted. As a result, the parallel temperature gradient, while finite, was not as large as the collisionality would indicate.

Investigating further pressure and power balance, no significant pressure losses were found in the conduction-limited discharge. On the contrary, target pressure was slightly higher than upstream pressure in both the discharges, which was speculated upon but no decisive explanation was reached. There are many uncertainties present in the analysis, from the effective probe collecting area affecting the values of $n_e$ and $q_{\parallel}$ to the still present if mitigated mapping error.

To explain the situation where are discharge with collisionality $\nu^* = 16$, and many like it, featured almost no temperature drop, the possibility of strong convective energy transport was suggested. While heat conduction, assumed by the 2PM to be the only channel of heat transport, needs a sufficient temperature gradient to drive a given amount of heat flux through a relatively cold SOL flux tube, convection has no such limits. The COMPASS SOL has been observed to be isothermal across all the processed discharges with collisionalities $\nu^* = 3$-$25$, within the uncertainties. This is in accord with last year's experiments with nitrogen seeding, where injecting nitrogen had either little to no effect or caused the entire SOL to cool.

The hypothesis that the COMPASS SOL is not able to support large temperature gradients must, of course, be addressed in theory, modelling, and experiment.

For instance the code SOLF1D can resolve the parallel profiles of SOL transport quantities, acting as a two-point model extended to one dimension. Dedicated discharges similar to those found in this analysis which feature a high collisionality can be performed and their scenarios optimised, looking for conditions under which the COMPASS SOL can truly be conduction-limited, with the target cool and upstream hot.

Achieving the conduction-limited regime on COMPASS would be beneficial not only for research on this tokamak alone, but it could also contribute to the global effort of designing and operating a fusion power plant. As a small tokamak, COMPASS has a unique place in scaling studies, occupying one end of the major radius axis. Being able to research detachment, which is the next step after the conduction limited regime, would also contribute toward the COMPASS-Upgrade project, as it can build on the experiment basis build by its predecessor.

# Bibliography


[1] J. Jacquinot. "Fifty years in fusion and the way forward". In: *Nuclear Fusion* 50.1 (2010). URL: http://stacks.iop.org/0029-5515/50/i=1/a=014001.

[2] P. Vandenplas and G. H. Wolf. "50 years of controlled nuclear fusion in the European Union". In: *Europhysics News* 39.2 (2008), pp. 21–28. ISSN: 0531-7479. DOI: 10.1051/epn:2008006. URL: http://www.europhysicsnews.org/10.1051/epn:2008006.

[3] T. Hirai et al. "Use of tungsten material for the ITER divertor". In: *Nuclear Materials and Energy* 9 (2016), pp. 616–622. ISSN: 23521791. DOI: 10.1016/j.nme.2016.07.003. URL: http://linkinghub.elsevier.com/retrieve/pii/S2352179115301046.

[4] The ITER organisation. *The ITER divertor*. May 2018. URL: https://www.iter.org/mach/divertor.

[5] G. Giruzzi et al. "Modelling of pulsed and steady-state DEMO scenarios". In: *Nuclear Fusion* 55.7 (2015), p. 073002. URL: http://stacks.iop.org/0029-5515/55/i=7/a=073002.

[6] R. Pánek et al. "Status of the COMPASS tokamak and characterization of the first H-mode". In: *Plasma Physics and Controlled Fusion* vol. 58.issue 1 (2016-01-01), pp. 014015–. ISSN: 07413335. DOI: 10.1088/0741-3335/58/1/014015. URL: http://stacks.iop.org/0741-3335/58/i=1/a=014015?key=crossref.cbd9509a544f4d9eb76fe62b71a66a58.

[7] P. Stangeby. *The plasma boundary of magnetic fusion devices*. Philadelphia: Institute of Physics Pub., 2000. ISBN: 07-503-0559-2.

[8] P. Stangeby. *Strong correlation between D 2 density and electron temperature at the target of divertors found in SOLPS-EIRENE and EDGE2D-EIRENE analysis*. Presented at the 24th ITPA Meeting on SOL/Divertor Physics, University of York, UK. 2017.

[9] C. Wersal, P Ricci, and J Loizu. "A comparison between a refined two-point model for the limited tokamak SOL and self-consistent plasma turbulence simulations". In: *Plasma Physics and Controlled Fusion* 59.4 (2017), p. 044011. URL: http://stacks.iop.org/0741-3335/59/i=4/a=044011.

[10] Automatica. *Tokamak equilbrium*. University of Padova. May 2018. URL: http://automatica.dei.unipd.it/tl_files/utenti/angelocenedese/IMAGES/Tokamak_Equilibrium.jpg.

[11] J. P. Gunn et al. "Evidence for a poloidally localized enhancement of radial transport in the scrape-off layer of the Tore Supra tokamak". In: *Journal of Nuclear Materials* 363-365 (2007). Plasma-Surface Interactions-17, pp. 484–490. ISSN: 0022-3115. DOI: https://doi.org/10.1016/j.jnucmat.2007.01.195. URL: http://www.sciencedirect.com/science/article/pii/S0022311507000943.

[12] J. Boedo et al. "A review of direct experimental measurements of detachment". In: *Plasma Physics and Controlled Fusion* 60.4 (2018), p. 044008. URL: http://stacks.iop.org/0741-3335/60/i=4/a=044008.

[13] G. D. Porter et al. "Characterization of the separatrix plasma parameters in DIII-D". In: *Physics of Plasmas* 5.5 (1998), pp. 1410–1422. ISSN: 1070-664X. DOI: 10.1063/1.872830. URL: http://aip.scitation.org/doi/10.1063/1.872830.

[14] C. K. Tsui et al. "Poloidal asymmetry in the narrow heat flux feature in the TCV scrape-off layer". In: *Physics of Plasmas* 24.6 (2017), pp. 062508–. ISSN: 1070-664X. DOI: 10.1063/1.4985075. URL: http://aip.scitation.org/doi/10.1063/1.4985075.

[15] J. Wesson and D. Campbell. *Tokamaks*. 4th ed. New York: Oxford University Press, 2011. ISBN: 0199592233.

[16] H. J. Sun et al. "Study of near SOL decay lengths in ASDEX Upgrade under attached and detached divertor conditions". In: *Plasma Physics and Controlled Fusion* 59.10 (2017), p. 105010. URL: http://stacks.iop.org/0741-3335/59/i=10/a=105010.

[17] S. I. Krasheninnikov, D. A. D'Ippolito, and J. R. Myra. "Recent theoretical progress in understanding coherent structures in edge and SOL turbulence". In: *Journal of Plasma Physics* 74.05 (2008). ISSN: 0022-3778. DOI: 10.1017/S0022377807006940. URL: http://www.journals.cambridge.org/abstract_S0022377807006940.

[18] J. Adámek et al. "Profile measurements of the electron temperature on the ASDEX Upgrade, COMPASS, and ISTTOK tokamak using Thomson scattering, triple, and ball-pen probes". In: *Review of Scientific Instruments* 87.4 (2016), pp. 043510–. ISSN: 0034-6748. DOI: 10.1063/1.4945797. URL: http://aip.scitation.org/doi/10.1063/1.4945797.

[19] V. Weinzettl et al. "Overview of the COMPASS diagnostics". In: *Fusion Engineering and Design* 86.6-8 (2011), pp. 1227–1231. ISSN: 09203796. DOI: 10.1016/j.fusengdes.2010.12.024. URL: http://linkinghub.elsevier.com/retrieve/pii/S0920379610005594.

[20] P. Bílková et al. "High resolution Thomson scattering on the COMPASS tokamak - extending edge plasma view and increasing repetition rate". In: *Journal of Instrumentation* 13.01 (2018), p. C01024. URL: http://stacks.iop.org/1748-0221/13/i=01/a=C01024.

[21] J. Adámek et al. "Electron temperature and heat load measurements in the COMPASS divertor using the new system of probes". In: *Nuclear Fusion* 57.11 (2017), p. 116017. URL: http://stacks.iop.org/0029-5515/57/i=11/a=116017.

[22] V. Weinzettl et al. "Progress in diagnostics of the COMPASS tokamak". In: *Journal of Instrumentation* 12.12 (2017), p. C12015. URL: http://stacks.iop.org/1748-0221/12/i=12/a=C12015.

[23] J. Adámek. *Schematic picture of a single ball-pen probe*. 2014. URL: https://en.wikipedia.org/wiki/Ball-pen_probe#/media/File:Ball-pen_probe_schematic.png.

[24] J. Adámek et al. "Direct Measurements of the Electron Temperature by a Ball-pen/Langmuir probe". In: *32nd EPS Conference on Plasma Physics*. 2005.

[25] T. S. V. K. Popov et al. "Electron energy distribution function, plasma potential and electron density measured by Langmuir probe in tokamak edge plasma". In: *Plasma Physics and Controlled Fusion* 51.6 (2009), p. 065014. URL: http://stacks.iop.org/0741-3335/51/i=6/a=065014.

[26] P. M. Kozlowski et al. "Theory of Thomson scattering in inhomogeneous media". In: *Scientific Reports* 6.1 (2016). ISSN: 2045-2322. DOI: 10.1038/srep24283. URL: http://www.nature.com/articles/srep24283.

[27] T. S. V. K. Popov et al. "Bi-Maxwellian electron energy distribution function in the vicinity of the last closed flux surface in fusion plasma". In: *Plasma Physics and Controlled Fusion* 57.11 (2015), p. 115011. URL: http://stacks.iop.org/0741-3335/57/i=11/a=115011.

[28] M. Aftanas. "Thomson Scattering Diagnostic on COMPASS Tokamak". PhD thesis. Charles University in Prague, Faculty of Mathematics and Physics, 2015.

[29] R. J. Merlino. "Understanding Langmuir probe current-voltage characteristics". In: *American Journal of Physics* 75.12 (2007), pp. 1078–1085.

[30] F. F. Chen. *Lecture Notes on Langmuir Probe Diagnostics*. Ed. by F. F. Chen. Electrical Engineering Department University of California, Los Angeles, 2003.

[31] J. Adámek et al. "A novel approach to direct measurement of the plasma potential". In: *Czechoslovak Journal of Physics* 54.3 (2004), pp. 95–99. ISSN: 00114626. DOI: 10.1007/BF03166386. URL: http://link.springer.com/10.1007/BF03166386.

[32] J. Adámek et al. "Direct Plasma Potential Measurements by Ball-Pen Probe and Self-Emitting Langmuir Probe on COMPASS and ASDEX Upgrade". In: *Contributions to Plasma Physics* 54.3 (2014), pp. 279–284. ISSN: 08631042. DOI: 10.1002/ctpp.201410072. URL: http://doi.wiley.com/10.1002/ctpp.201410072.

[33] S. Murphy-Sugrue et al. "Improved understanding of the ball-pen probe through particle-in-cell simulations". In: *Plasma Physics and Controlled Fusion* 59.5 (2017), p. 055007. URL: http://stacks.iop.org/0741-3335/59/i=5/a=055007.

[34] J. Adámek et al. “Ball-Pen Probe Measurements in L-Mode and H-Mode on ASDEX Upgrade”. In: *Contributions to Plasma Physics* 50.9 (2010), pp. 854–859. ISSN: 08631042. DOI: 10.1002/ctpp.201010145. URL: http://doi.wiley.com/10.1002/ctpp.201010145.

[35] M. Dimitrova et al. “Plasma potential and electron temperature evaluated by ball-pen and Langmuir probes in the COMPASS tokamak”. In: *Plasma Physics and Controlled Fusion* 59.12 (2017), p. 125001. URL: http://stacks.iop.org/0741-3335/59/i=12/a=125001.

[36] C. G. Silva et al. “SOL currents and divertor asymmetries on COMPASS-D”. In: *Journal of Nuclear Materials* 266-269 (1999), pp. 679–684. ISSN: 00223115. DOI: 10.1016/S0022-3115(98)00600-X. URL: http://linkinghub.elsevier.com/retrieve/pii/S002231159800600X.

[37] G. M. Staebler and F.L. Hinton. “Currents in the scrape-off layer of diverted tokamaks”. In: *Nuclear Fusion* 29.10 (1989), p. 1820. URL: http://stacks.iop.org/0029-5515/29/i=10/a=017.

[38] J. Marki et al. “Sheath heat transmission factors on TCV”. In: *Journal of Nuclear Materials* 363-365 (2007), pp. 382–388. ISSN: 00223115. DOI: 10.1016/j.jnucmat.2007.01.197. URL: http://linkinghub.elsevier.com/retrieve/pii/S0022311507000761.

[39] K. Jiráková. “Characterization of edge plasma fluctuations in tokamak COMPASS”. Bachelor’s thesis. FNSPE CTU in Prague, 2015.

[40] A. J. Webster. “Techniques for studying the separatrix of tokamak plasmas”. In: *Physics of Plasmas* 16.1 (2009), pp. 012501–. ISSN: 1070-664X. DOI: 10.1063/1.3046070. URL: http://aip.scitation.org/doi/10.1063/1.3046070.

[41] J. Horáček. “Measurement of edge electrostatic turbulence in the TCV tokamak plasma boundary”. Disertační práce. Lausanne: École polytechnique fédérale de Lausanne, 2006. DOI: 10.5075/epfl-thesis-3524. URL: http://infoscience.epfl.ch/record/83511/files/EPFL_TH3524.pdf.

[42] B. Faugeras et al. “2D interpolation and extrapolation of discrete magnetic measurements with toroidal harmonics for equilibrium reconstruction in a tokamak”. In: *Plasma Physics and Controlled Fusion* 56.11 (2014), p. 114010. URL: http://stacks.iop.org/0741-3335/56/i=11/a=114010.

[43] K. Jiráková. “Radial profiles of the scrape-off layer of the COMPASS tokamak”. Research project. FNSPE CTU in Prague, 2016.

[44] O. E. Garcia et al. “Turbulence and intermittent transport at the boundary of magnetized plasmas”. In: *Physics of Plasmas* 12.6 (2005), pp. 062309–. ISSN: 1070664x. DOI: 10.1063/1.1925617. URL: http://scitation.aip.org/content/aip/journal/pop/12/6/10.1063/1.1925617.

[45] O. E. Garcia et al. “Fluctuations and transport in the TCV scrape-off layer”. In: *Nuclear Fusion* 47.7 (2007), pp. 667–676. ISSN: 00295515. DOI: 10.1088/0029-5515/47/7/017. URL: http://stacks.iop.org/0029-5515/47/i=7/a=017?key=crossref.52b05fe76865fa0326117e3fe0b71112.

[46] J. Seidl et al. “Electromagnetic characteristics of geodesic acoustic mode in the COMPASS tokamak”. In: *Nuclear Fusion* 57.12 (2017-12-01), pp. 126048–. ISSN: 0029-5515. DOI: 10.1088/1741-4326/aa897e. URL: http://stacks.iop.org/0029-5515/57/i=12/a=126048?key=crossref.8e41de493084efddc3884bd2b69

[47] M. Komm et al. “First detachment studies on COMPASS tokamak using nitrogen seeding”. In: *44th EPS Conference on Plasma Physics*. 2017.

[48] Encyclopedia of Mathematics. *Cardano formula*. May 2018. URL: https://www.encyclopediaofmath.org/index.php/Cardano_formula.

# Appendix A

# List of used symbols

The following symbols were used in this work:

| **Quantity name** | **Symbol** | **Unit** | **Value** |
|---|---|---|---|
| Elementary charge | $e$ | C | $e = 1.602 \times 10^{-19}$ C |
| Electron temperature | $T_e$ | eV | |
| Flux tube length/Connection length | $L$ | m | |
| Parallel heat flux | $q_{\parallel}$ | $\mathrm{Wm}^{-2}$ | |
| Parallel flux tube coordinate | $s$ | m | |
| Ion mass (deuteron) | $m_i$ | kg | $m_i = 3.34 \times 10^{-27}$ kg |
| Radial coordinate (measured from the tokamak centre) | $R$ | m | |
| Radial coordinate (measured from the magnetic axis) | $r$ | m | |
| Ion saturated current | $I_{sat,i}$ or $I_{sat}$ | A | |
| Electron saturated current | $I_{sat,e}$ | A | |
| Current density | $j$ | $\mathrm{Am}^{-2}$ | |

# Appendix B

# Exact 2PM formulas for the dependent variables

Here the entire process of extracting $T_t$ from the basic 2PM equations will be shown. Let us first write the three equations down.

$$n_u T_u = 2 n_t T_t \tag{B.1}$$

$$T_u{}^{7/2} = T_t{}^{7/2} + \frac{7}{2}\frac{q_\parallel L}{\kappa_{0e}} \tag{B.2}$$

$$q_\parallel = \gamma e n_t T_t c_{s,t} \tag{B.3}$$

Our first goal is to obtain an equation only for $T_t$ (blue) and the control variables (black), eliminating the other two dependent variables (red). From equation (B.3) we extract the target density,

$$n_t = \frac{q_\parallel}{\gamma e T_t c_{s,t}}, \tag{B.4}$$

and from equation (B.1) an expression for the upstream temperature,

$$T_u = \frac{2T_t}{n_u} n_t = \frac{2T_t}{n_u}\frac{q_\parallel}{\gamma e T_t c_{s,t}},$$

where we promptly insert (B.4). We insert this into equation (B.2), eliminating all red variables and obtaining:

$$\left(\frac{2q_\parallel}{n_u \gamma e c_{s,t}}\right)^{7/2} = T_t{}^{7/2} + \frac{7}{2}\frac{q_\parallel L}{\kappa_{0e}} \tag{B.5}$$

Finally we insert

$$c_{s,t} = \left(\frac{2eT_t}{m_i}\right)^{1/2}$$

to obtain an equation only for $T_t$:

$$\left(\frac{q_\parallel (2m_i)^{1/2}}{n_u \gamma e^{3/2}}\right)^{7/2} T_t{}^{-7/4} = T_t{}^{7/2} + \frac{7}{2}\frac{q_\parallel L}{\kappa_{0e}} \tag{B.6}$$

Substituting now $x = T_t^{7/4}$, $A = \left(\frac{q_\parallel (2m_i)^{1/2}}{n_u \gamma e^{3/2}}\right)^{7/2}$ and $B = \frac{7}{2}\frac{q_\parallel L}{\kappa_{0e}}$, the equation transforms into a simpler one,

$$Ax^{-1} = x^2 + B.$$

We multiply this with $x$ and move all terms to the left-hand side to obtain the equation given in section 1.2:

$$x^3 + Bx - A = 0 \tag{B.7}$$

The solution of this equation can be found analytically using Cardano's formula [48]. In its general form, the formula states that the equation

$$x^3 + ax^2 + bx + c = 0$$

has the three solutions

$$x = -\frac{p}{3u} + u - \frac{a}{3}$$

where

$$p = b - \frac{a^2}{3}$$
$$q = c + \frac{2a^3 - 9ab}{27}$$
$$u = \sqrt[3]{-\frac{q}{2} \pm \sqrt{\frac{q^2}{4} + \frac{p^3}{27}}}.$$

The solution multiplicity stems from the parameter $u$, which can yield up to 3 values depending on the sign inside it and on the result of the complex third root. Applying Cardano's formula to equation (B.7), the parameters $p$, $q$, and $u$ are

$$p = \frac{7}{2}\frac{q_\parallel L}{\kappa_{0e}}$$
$$q = -\left(\frac{q_\parallel (2m_i)^{1/2}}{n_u \gamma e^{3/2}}\right)^{7/2}$$
$$u = \sqrt[3]{\frac{1}{2}\left(\frac{q_\parallel (2m_i)^{1/2}}{n_u \gamma e^{3/2}}\right)^{7/2} + \sqrt{\frac{1}{4}\left(\frac{q_\parallel (2m_i)^{1/2}}{n_u \gamma e^{3/2}}\right)^{7} + \frac{1}{27}\left(\frac{7}{2}\frac{q_\parallel L}{\kappa_{0e}}\right)^{3}}}.$$

The sign in $u$ has been changed to $+$ so that the resulting $x$ is is positive and real. Transforming the solution $x$ back into $T_t$, the solution of equation (B.6) is

$$T_t = \left( -\frac{7}{6}\frac{q_\parallel L}{\kappa_{0e}} \left( \frac{1}{2}\left(\frac{q_\parallel (2m_i)^{1/2}}{n_u \gamma e^{3/2}}\right)^{7/2} + \sqrt{\frac{1}{4}\left(\frac{q_\parallel (2m_i)^{1/2}}{n_u \gamma e^{3/2}}\right)^{7} + \frac{1}{27}\left(\frac{7}{2}\frac{q_\parallel L}{\kappa_{0e}}\right)^{3}} \right)^{-1/3} \right.$$
$$\left. + \sqrt[3]{\frac{1}{2}\left(\frac{q_\parallel (2m_i)^{1/2}}{n_u \gamma e^{3/2}}\right)^{7/2} + \sqrt{\frac{1}{4}\left(\frac{q_\parallel (2m_i)^{1/2}}{n_u \gamma e^{3/2}}\right)^{7} + \frac{1}{27}\left(\frac{7}{2}\frac{q_\parallel L}{\kappa_{0e}}\right)^{3}}} \right)^{4/7}. \tag{B.8}$$

# Appendix C

# Additional plots

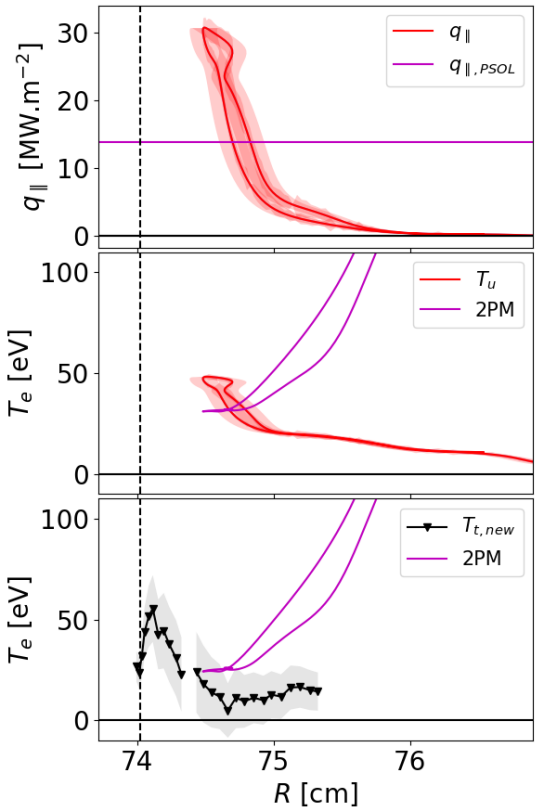


Figure C.1: Semi-successful application of Eq. (3.4) to infer the upstream separatrix position. While the conclusion from the upstream profile is that $R_{sep} \approx 74.6$ cm, the target profile mapping correction (the BPP-EFIT correction, (3.6)) is not accurate and denies validation. Discharge #13925.

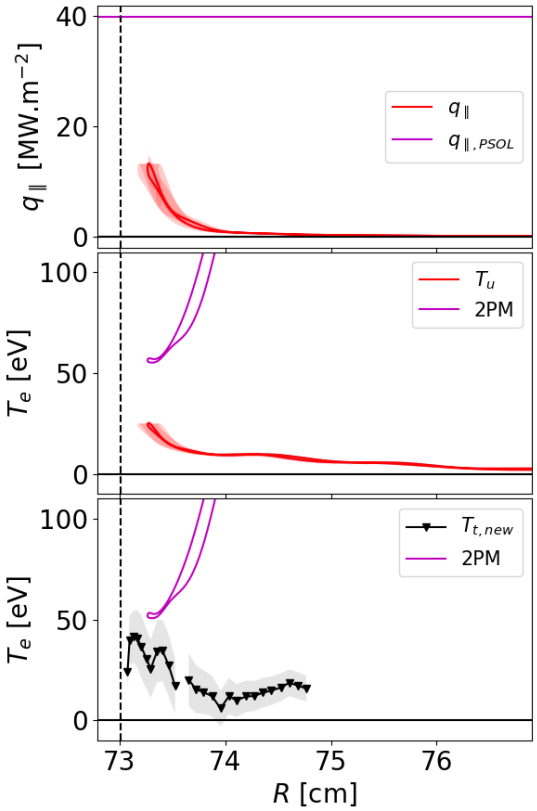


Figure C.2: Unsuccessful application of Eq. (3.4) to infer the upstream separatrix position. The probe does not perform a deep enough reciprocation and it does not approach the vicinity of the separatrix. Approximately half of the processed 61 discharges met this outcome. Discharge #13797.

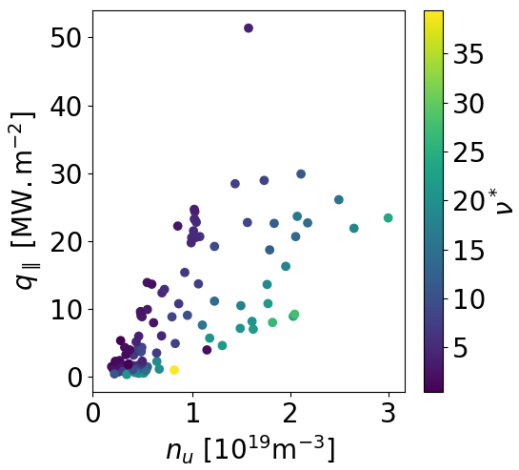


Figure C.3: The COMPASS operational space, with $q_\parallel$ and $n_u$ taken at the corrected EFIT separatrix. Inner target. 109 datapoints.

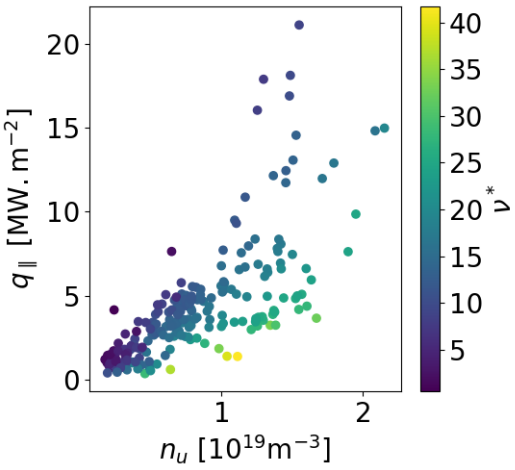


Figure C.4: The COMPASS operational space, with $q_\parallel$ and $n_u$ taken at the BPP maximum. Inner target. 224 datapoints.

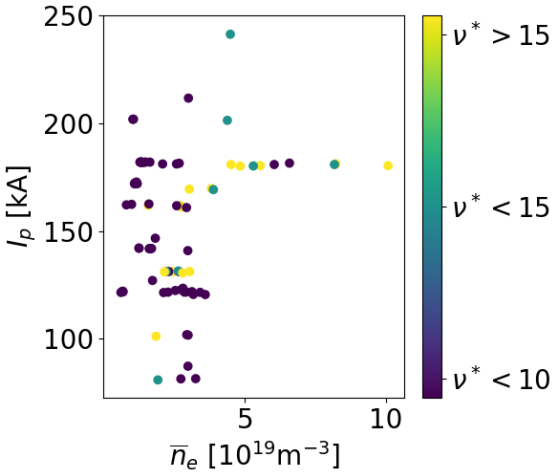


Figure C.5: The COMPASS operational space, with $I_p$ and $\overline{n}_e$ averaged over the flat top, collisionality computed at the corrected EFIT separatrix. Inner target. 90 datapoints.

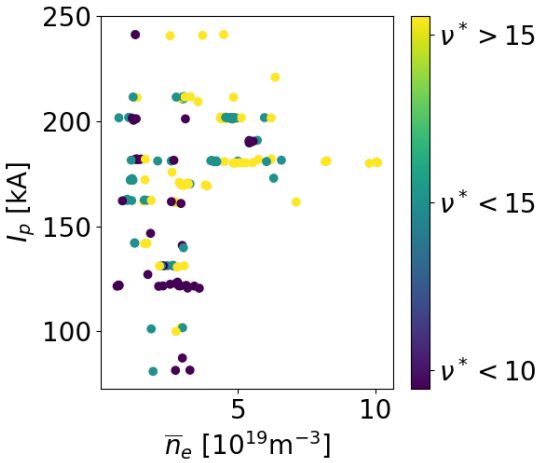


Figure C.6: The COMPASS operational space, with $I_p$ and $\overline{n}_e$ averaged over the flat top, collisionality computed at the BPP potential maximum. Inner target. 197 datapoints.

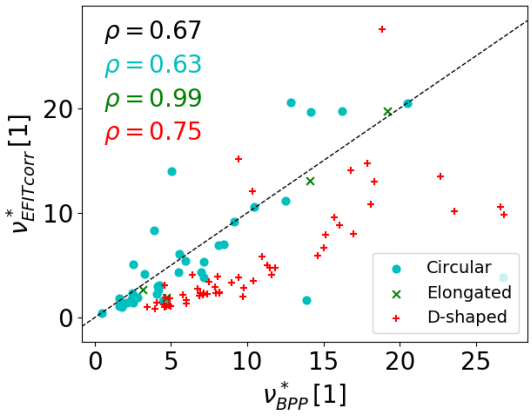


Figure C.7: Scatteplot comparing the collisionality computed from the 2PM using the BPP maxima as separatrix and using the corrected EFIT separatrix.

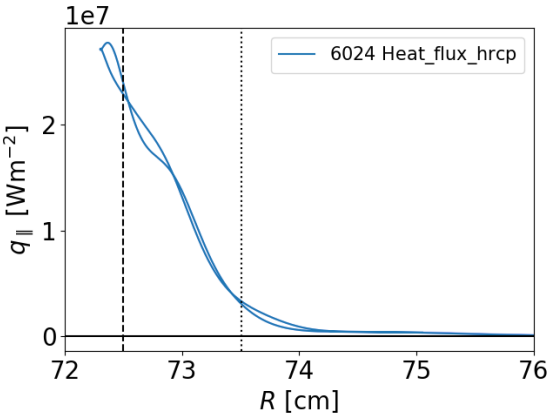


Figure C.8: Heat flux profile in discharge #6024, which has $\nu^*_{BPP} = 16$ and $\nu^*_{EFIT,corr} = 5$ on the plot to the left. Dashed line is $R_{EFIT,corr}$, dotted line is $R_{BPP}$.

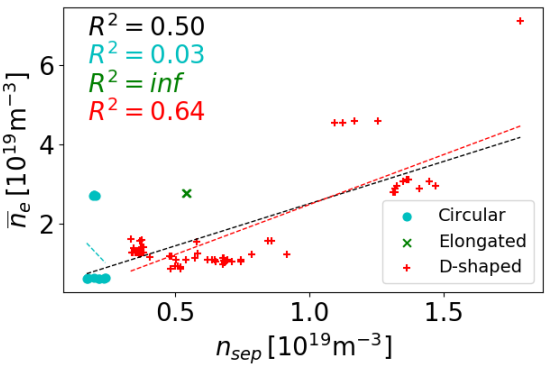


Figure C.9: Comparison of the line-averaged density $\overline{n}_e$ to the density taken at the BPP maximum $n_{sep}$. The linear fit across all discharges (black line) is $\overline{n}_e = 2.13 n_{sep} + 0.38 \times 10^{19}$.

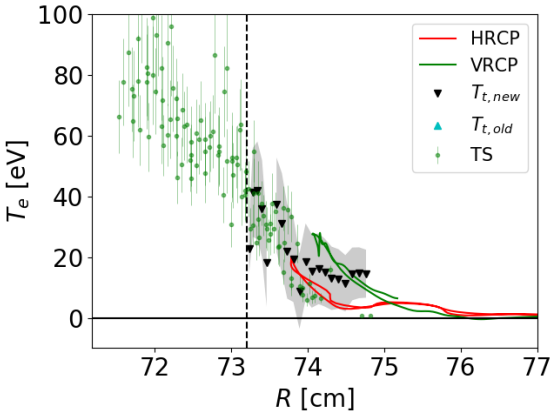


Figure C.10: Example of profile comparison where the VRCP profile does not directly tie into the TS profile. Discharge #15184.